In-liquid bulk acoustic wave resonators for biosensing applications

Girish Rughoobur

University of Cambridge

Department of Engineering

St Edmund's College

January 2017

This dissertation is submitted for the degree of:
Doctor of Philosophy in Engineering

Declaration

I hereby declare that this dissertation submitted herein:

- is the result of my own work and includes nothing which is the outcome of work done in collaboration except as declared in the acknowledgements and specified in the text;
- is not substantially the same as any that I have submitted, or, is being concurrently submitted for a degree or diploma or other qualification at the University of Cambridge or any other University or similar institution except as declared in the acknowledgements and specified in the text. I further state that no substantial part of my dissertation has already been submitted, or, is being concurrently submitted for any such degree, diploma or other qualification at the University of Cambridge or any other University or similar institution except as declared in the acknowledgements and specified in the text; and
- does not exceed the prescribed limit for the Department of Engineering of 65,000 words and 150 figures.

Girish Rughoobur

January 2017

Acknowledgement

I wish to thank my supervisor Prof. Andrew J. Flewitt who has been a constant motivator and who has been providing me with resources and advice since the start of the project. I am also very thankful to my advisor Prof. William I. Milne, who has also provided advice on the research plans and guidance for a future career. I am most grateful to Dr. Luis García-Gancedo (former Research Associate in the Electrical Engineering Division, Department of Engineering, University of Cambridge) for training me in device fabrication: sputtering, evaporation, etching and photolithography. Likewise I am extremely thankful to Dr. Mario DeMiguel-Ramos for the enriching discussion, his help on device modelling and fabrication, and ideas that enabled me to understand the principles underlying the devices that we fabricated over the last three years. In addition Dr. Mario DeMiguel-Ramos has provided acoustic reflectors and AlN seed layers used in Chapter 2. I am very grateful to Prof. Enrique Iborra and the members (Dr. Marta Clement, Dr. Jimena Olivares, Teona Mirea, Dr. José-Miguel Escolano and Prof. Jesus Sangrador) of his research group for having me as a visitor in his group during my PhD, and for all their kindness during my time in Madrid. Prof. Iborra has provided help with software design, device fabrication and analysis, Dr. José-Miguel Escolano has helped with the biosensing of Rabbit IgG and Teona has helped with the design and fabrication of acoustic reflectors for higher temperatures.

I am most grateful to Dr. Kham Man Niang for help in fabrication, great ideas and for being a good friend throughout the PhD. Furthermore I would like to thank Dr. Ewelina Wajs for her invaluable help with device functionalisation for PSA detection. I am very grateful to Dr. Ian Farrer and Dr. Harvey Beere from Cavendish lab for helping with XRR/XRD measurements, from CAPE: Ivonne Medina-Salazar (now at Nokia), Adrian Ginn, Neil Laurence, Kasia, Mark Barrett, Trevor Foster, Dr. David Hasko, and scientists from PlasmaQuest: Dr. Sarah Thornley, Dr. Peter Hockley, Dr. Stuart Rand, Neil Fryer, Dr. Hayley Brown and Dr. Steve Wakeham, for helping me in designing processes in the HiTUS. I also thank Graham Gale, from Wordentec for his help in fixing the HiTUS. Finally I would like to acknowledge all my friends: Xingyi, Xinya, Calum, Edward, Shan, Hisashi, Mario, Marie Ammar, Akmal, Zongyin, Lorenzo, Oscar, Sabina, Paul, Andrea, Indrat, Phillip, Ruizhi, Richard, Junhee, Jack, Hannah, Sarwat, Tim Butler, Sanggil, Mehdi, Dilek, Farah Al-Naimi, Juan, Melanie Stamp and Yang Li. I also acknowledge collaboration with Eric Hou, Prof. Chris Ford and William Hsiao from the Cavendish labs and Dr. Pawan Shrestha, Prof. Tim Wilkinson and Dr. Luigi Occhipinti in CAPE. I would also like to thank Dr. Susan Haines and Dr. Ravi Sundaram from St Edmund's College and Penny Davison for support during the last 3 years. I also very grateful to my parents and my family in Mauritius for all their love and support, which has helped me reach this far.

I also wish to acknowledge the generosity of the Cambridge Trust for the Cambridge International Scholarship and the IET for the postgraduate scholarship award, which have supported me financially during this research.

Abstract

Gravimetric sensors based on thin-film bulk acoustic wave (BAW) resonators operating between 1-5 GHz have tremendous potential as biosensors because they are inexpensive, label-free, fast and highly sensitive. The two main challenges in this objective are: the conventional longitudinal mode resonance in *c*-axis oriented piezoelectric films suffers from more than 90% damping in liquid; the alternative is the shear mode resonance, with lower damping in liquid but which requires an inclined *c*-axis piezoelectric film, a process that is still not fully scalable. In this thesis, seed layers such as AlN with mainly (103) orientations are used to promote the growth of homogeneously inclined *c*-axis ZnO (inclination of up to ∼45°) films without significant equipment modifications. Sputtered Al electrodes with controlled roughness are then substituted for the parasitic AlN seed layers to improve the electromechanical performance. At a substrate temperature, $T_{\mathrm{S}} = 100$ °C, an optimum surface roughness of 9.2 nm yields homogeneously inclined *c*-axis ZnO films with angles ∼25°. Solidly mounted resonators (SMRs) operating in a shear mode at ∼1.1 GHz with the Al electrodes have resonant quality factors (Q_r) higher than 150 and effective electromechanical coupling coefficients, k^2_{eff}, of 2.9-3.4%, which are improved from only 2.2% with the AlN seed layers. This shear mode of the ZnO SMRs has mass sensitivities, S_m of (4.9 ± 0.1) kHz·cm^2/ng and temperature coefficients of frequency (TCF) of $-(66 \pm 2)$ ppm/K. Viscosity sensing is carried out with different ethanol-water compositions; the SMRs are functionalised and successfully used in the detection of Rabbit Immunoglobin G. To mitigate the longitudinal mode damping in water, multi-wall carbon nanotube (CNT) forests are grown by chemical vapour deposition (CVD) at 600 °C using Fe/Al layers on the active area of inclined *c*-axis AlN SMRs designed for improved thermal and chemical stability. The dense CNT forest (with 0.5/8 nm Fe/Al) of ∼15 µm height provides an acoustic isolation to DI water with only 50-70% drop in the longitudinal mode Q_r compared to 99% in SMRs without the CNTs. Mass loading is still detected and demonstrated by detecting bovine serum albumin (BSA) in water whereas with forest heights of ∼30 µm and no significant frequency shifts due to mass attachment are observed. With the CNTs the longitudinal mode is shown for the first time to be more sensitive to mass (∼7×) than the shear mode in liquid, highlighting the potential of CNTs for the large scale use of the longitudinal mode for in-liquid sensing.

Publications

Journal publications

In progress

1. **Rughoobur, G** and Sugime, H and DeMiguel-Ramos, M and Mirea, T and Zheng, S and Robertson, J and Iborra, E and Flewitt AJ (2016) *Carbon nanotubes enabling the longitudinal acoustic resonant mode for in-liquid sensing*, To be submitted to Nature Communications pending Patent filing.

2. **Rughoobur, G** and DeMiguel-Ramos, M and Escolano, JM and Iborra, E and Flewitt AJ (2016) *Gravimetric sensors operating at 1.1 GHz based on inclined c-axis ZnO grown on textured Al electrodes*, Scientific Reports (under review).

3. Williams, C and **Rughoobur, G** and Flewitt, AJ and Wilkinson, TD (2016) *Nanostructured plasmonic metapixels.* Scientific Reports (under review).

Published

1. Kamarudin, MA and Khan, AK and Williams, C and **Rughoobur, G** and Said, SM and Nosheen, S and Flewitt, AJ and Qasim, M and Wilkinson TD (2016) *Self-assembled liquid crystalline nanotemplate for dye-sensitized solar cells*, Electrochimica Acta, 222, pp. 657-667.

2. Han, S and Niang, KM and **Rughoobur, G** and Flewitt, AJ (2016) *Effects of post-deposition vacuum annealing on film characteristics of p-type* Cu_2O *and its impact on thin film transistor characteristics*, App. Phys. Lett., 109,

173502.

3. Williams, C and **Rughoobur, G** and Flewitt, AJ and Wilkinson, TD (2016) *Single-step fabrication of thin-film linear variable bandpass filters based on metal–insulator–metal geometry*, Applied Optics, 55(32), pp. 9237-9241.

4. Williams, C and Bartholomew, R and **Rughoobur, G** and Gordon, GS and Flewitt, AJ and Wilkinson, TD (2016) *Fabrication of nanostructured transmissive optical devices on ITO-glass with UV1116 photoresist using high-energy electron beam lithography*, Nanotechnology, 27 (2016) 485301 (11pp).

5. Khan, AA and **Rughoobur, G** and Kamarudin, MA and Sepe, A and Dolan, JA and Flewitt, AJ and Qasim, MM and Wilkinson, TD (2016) *Homologous binary mixtures and improved hole conduction of self-assembled discotic liquid crystals*, Organic Electronics: physics, materials, applications, 36, pp. 35-44.

6. **Rughoobur, G**, DeMiguel-Ramos, M and Mirea T and Clement ,M and Olivares, J and Díaz-Durán, B and Sangrador, J and Milne, WI and Iborra, E and Flewitt, AJ (2016) *Room temperature sputtering of inclined c-axis ZnO for shear mode solidly mounted resonators*, Applied Physics Letters, 108, 034103.

7. Villa-López, FH and **Rughoobur, G** and Thomas, S and Flewitt, AJ and Cole, M and Gardner, JW (2015) *Design and modelling of solidly mounted resonators for low-cost particle sensing*, Measurement Science and Technology, 27 (2016) 025101 (13pp).

Conference proceedings

1. M. DeMiguel-Ramos, **G. Rughoobur**, A. J. Flewitt, T. Mirea ; B. Díaz-Durán, J. Olivares, M. Clement and E. Iborra,“Transparent thin film bulk acoustic wave resonators,” 2016 European Frequency and Time Forum (EFTF), York, 2016, pp. 1-4.

2. M. DeMiguel-Ramos, M. Clement, J. Goicuría, J. Olivares, T. Mirea, E. Iborra, **G. Rughoobur**, A. J. Flewitt, W. I. Milne, “ZnO/AlN stacked BAW resonators with double resonance,” 2014 IEEE International Ultrasonics Symposium, Chicago, IL, 2014, pp. 1484-1487.

3. M. DeMiguel-Ramos, J. Olivares, T. Mirea, M. Clement, E. Iborra, **G. Rughoobur**, L. Garcia-Gancedo, A. J. Flewitt and W. I. Milne, "The influence of acoustic reflectors on the temperature coefficient of frequency of solidly mounted resonators," 2014 IEEE International Ultrasonics Symposium, Chicago, IL, 2014, pp. 1472-1475.
4. T. Kim, S. Lim, S. Lee, D. Kim, F. Al-Naimi, P. Helfenstein, M. Spain, S. H. Lee, **G. Rughoobur**, L. Garcia-Gancedo, A. J. Flewitt and S. H. Lee, "A wide-range frequency tunable SMR-CMOS oscillator for gas sensing," IEEE Sensors 2014 Proceedings, Valencia, 2014, pp. 74-77.
5. **G. Rughoobur**, L. García-Gancedo, A. J. Flewitt, W. I. Milne, M. DeMiguel-Ramos, M. Clement, T. Mirea, J. Olivares and E. Iborra, "Seed layer controlled deposition of ZnO films with a tilted c-axis for shear mode resonators," European Frequency and Time Forum (EFTF), 2014, Neuchatel, 2014, pp. 297-300.
6. F. Al-Naimi, M. Spain, P. Helfenstein, T. Kim, Y. Lee, S. H. Lee, **G. Rughoobur**, L. Garcia-Gancedo and A. J. Flewitt, "Investigation of polymer deposition techniques on a Solidly Mounted Resonator arrays for vapour sensing," IEEE Sensors 2014 Proceedings, Valencia, 2014, pp. 202-205.

Patents

1. Formation of electrodes on a polymeric body
   Inventors: Tan, E, ***Rughoobur, G*** *and Occhipinti, L*
   Applied, Application number: 1619959.8
2. In-liquid longitudinal mode bulk acoustic wave resonator
   Inventors: ***Rughoobur, G****, Flewitt, AJ, DeMiguel-Ramos, M, Iborra, E and Mirea, T*
   In process

Contents

List of Figures

List of Tables

Nomenclature

Acronyms

AFM	Atomic force microscope
APTES	(3-Aminopropyl) triethoxysilane
BAW	Bulk acoustic wave
BSA	Bovine serum albumin
CMOS	Complementary metal oxide semiconductor
CNT	Carbon-nanotube
DI	De-ionised
DNA	Deoxyribonucleic acid
EtOH	Ethanol
FBAR	Film bulk acoustic resonator
GA	Glutaraldehyde
HiTUS	High target utlisation sputtering
IARC	International Agency for Research on Cancer
IDT	Inter digitated transducer
IPA	Isopropyl alcohol
LOD	Limit of detection
mBVD	modified Butterworth Van-Dyke
MWCNTs	Multi-wall CNTs
POC	Point of care
PSA	Prostrate specific antigen
QCM	Quartz crystal microbalance

RF	Radio frequency
RIE	Reactive ion etching
RT	Room temperature
SAW	Surface acoustic wave
SEM	Scanning electron microscope
SMR	Solidly mounted resonator
SPR	Surface plasmon resonance
SWCNTs	Single wall CNTs
TCF	Temperature coefficient of frequency
TLM	Thickness longitudinal mode
TSM	Thickness shear mode
VACNTs	Vertically aligned CNTs
WHO	World Health Organisation
XRD	X-ray diffraction

Variables

α	Polarisation angle
A	Active area
$\boldsymbol{c^E}$	Elastic stiffness matrix under constant electic field
χ	Inclination angle in the piezoelectric material
C	Capacitance
$\mathbf{D}$	Electic field displacement
δ	Decay length
$\mathbf{E}$	Electric field intensity
$\boldsymbol{e}$	Piezoelectric stress constant
E	Young's modulus
F	Force applied
f_a	Anti-resonant frequency
f_r	Resonant frequency

I	Electrical current
k_{eff}	Effective acoustic coupling coefficient
k	Propagation wave vector
k_t	Electromechanical coupling constant
λ	Wavelength
L	Inductance
m_r	Mass resolution
μ	Film stiffness (shear modulus)
ω	Angular frequency
$\boldsymbol{\epsilon}^{\boldsymbol{S}}$	Clamped dielectric constant
ν	Poisson's ratio
Ψ	Inclination angle with respect to *c*-axis in XRD
Q	Quality factor
ρ	Material density
R	Resistance
S_{11}	Input reflection coefficient
S_{21}	Forward transfer coefficient
S_m	Mass sensitivity
$\mathbf{S}$	Mechanical strain
S_v	Viscosity sensitivity
t	Thickness of layer
θ	Angle in degrees
$\mathbf{T}$	Mechanical stress
v	Acoustic velocity
η	Viscosity of a liquid
T	Temperature
V	Electrical voltage
Y	Electrical admittance
Z_a	Acoustic impedance
Z_{in}	Input electrical impedance

Chapter 1

Introduction

Early detection of diseases can save millions of lives. In 2012, the International Agency for Research on Cancer (IARC) reported that approximately 8.2 million deaths were caused by cancer worldwide, and it is estimated that this number will rise to 13 million by 2030.[1] According to the World Health Organisation (WHO), over 30% of cancer deaths can be prevented by early detection of cancer biomarkers, treatment and healthy life-style.[2] Biochemical substances such as cancer biomarkers can be identified and measured by biosensors, which are important for early diagnosis and eventually successful disease treatment. A biosensor consists of two fundamental components —a biological recognition element (receptor) and a transducer —that are in close contact to each other.[3–5] The selectivity of the biosensor depends on the binding affinity of the biological receptors. Successful biorecognition events are transduced to either an optical or an electrical signal, which in general directly relates to the concentration of target molecules.[4, 6] The most common ways to classify biosensors are based on either the biological element in the receptor (enzymes, antibodies, nucleic acids, DNA and organelles) or on the transduction principle (electrochemical, optical, mechanical, piezoelectric, magnetic and thermometric).[4, 7, 8] Most biosensing technologies aim to analyse multiple samples in real-time for early disease diagnosis. In order to achieve this, biosensors need to be highly sensitive to ideally track single molecules, highly selective to detect specific molecules only, have low noise for low detection limit, fast with no sample treatment, small for array assembly, low-cost for industrial fabrication, bio-compatible to eliminate sample destruction, easy to operate for point of care (POC) applications and reliable to avoid false-positive results.[9–13] Electrochemical sensors are low cost, small and disposable but lengthy sample treatments are required.[14, 15] Non-specific binding from electrolyte ions renders them unsuitable for real-time sensing.[16] Optical biosensing techniques such as fluorescence spectroscopy have high sensitivities, a range of fluorophores and labelling techniques.[14, 17] Nevertheless fluorophores are costly and have short shelf lives.[18] Fluorescent tagging can also inhibit binding of small molecules.[16] Surface plasmon resonance (SPR) biosensors are highly sensitive, real-time, label free, and use minimal amounts of reagents.[17, 19, 20] Although commercial SPR sensors have the best limit of detection of the order of $0.01\,\mathrm{ng/cm^2}$, they need expensive and bulky optical systems.[16, 21–23] Mechanical biosensors such as micro-cantilevers are fast, small, label-free and can theoretically have detection limits of $0.01\,\mathrm{ng/cm^2}$.[24, 25] Yet in fluids, the viscosity causes severe impairment to the sensitivity, which often entails the removal of the liquid after target-receptor interactions.[21, 25] Microcantilevers with low damping in liquid have been fabricated by Lee *et al.* [26], but mechanical biosensors remain fragile and flexible.[27]

1.1 Electro-acoustic devices and sensors

Electro-acoustic sensors have the potential for application in low-cost and real-time biosensors. These sensors consist of a piezoelectric material in which electrical energy is converted into mechanical energy and vice-versa, when a small radio-frequency (RF) signal is applied across it. Most of electro-acoustic devices use frequency shifts due to mass accretion after successful target-receptor interactions to track specific biomolecules —gravimetric sensing.[28] Such devices are broadly categorised into Surface Acoustic Wave (SAW) and Bulk Acoustic Wave (BAW) resonators. Acoustic waves (10 MHz to 1 GHz) propagate on the surface of a piezoelectric substrate in SAWs whereas in BAW resonators, the waves (1 GHz to 10 GHz) propagating through the thickness of the piezoelectric material.[29, 30] SAW devices can either be used as resonators or delay lines. In the latter configuration successful recognition events cause time delays in the signal at the output.[31] Achieving high operation frequencies for high sensitivities is, however, limited by the high resolution lithographic processes needed in fabricating inter-digitated transducers (IDTs) with short finger spacings.[32, 33] Static discharge can be another issue with the proximity of the IDTs; scaling down the device also undermines its power handling capabilities.[34, 35] The quartz crystal microbalance (QCM) is a well-established BAW technology, where a thickness shear mode (TSM) is generated within a single crystalline AT–cut quartz wafer "sandwiched" between two electrodes.[36] QCMs have relatively large diameters of the order of 1 cm.[33, 37] Typical thicknesses of the quartz layer vary between 100 and 300 µm, which limit the resonant frequency from 5 MHz to 20 MHz.[33] The mass sensitivities of QCMs, S_m, which is proportional to the square of the resonant frequency according to Sauerbrey [38], is therefore limited.[37, 39] Scaling down the dimensions of quartz layers for high resonant frequencies is complicated because the layers become fragile.[39, 40] Moreover multiplexed sensing with arrays of QCMs is costly and incompatible with CMOS technologies.[41] Nonetheless QCMs have unparalleled Q-factors (20,000 - 50,000 in air) that ensure mass resolutions of less than 1 ng/cm^2.[13, 42] For example, Nirschl *et al.* [23, 43] reported a detection limit of 0.38 ng/cm^2 for QCM in protein detection.

The advent of microfabrication technologies has spawned a new generation of high frequency (from 1 GHz to 5 GHz) thin film BAW resonators with inherently higher sensitivities, which have the potential to outperform QCM biosensors.[44] Their small size (µm scale), low-cost and CMOS-compatibility make them ideal for array fabrication.[45, 46] Yet mass resolutions with high-frequency BAWs are not significantly better than QCMs mainly because of the effects of boundary conditions, small size and increased noise at higher frequencies.[41] Also a major limitation in the application of BAW resonators as biosensors is the substantial acoustic damping in liquid environments of the conventional resonant mode —the thickness longitudinal mode (TLM).[47] A thickness shear mode (TSM) is instead necessary for biosensing as shear waves do not compress and thus have lower damping in liquids, which is caused by the viscous loading.[48, 49] With the growing need for BAW resonators for real-time biosensing applications, different methods have been adopted to achieve the shear resonance in thin piezoelectric films. The shear resonance is most efficiently excited when the piezoelectric film has a crystallographic orientation that is inclined at an angle to the exciting electric field.[50, 51] Nonetheless significant modification to the deposition systems are necessary to achieve wafer-level uniformity of thin piezoelectric films of ZnO and AlN to resonate with a TSM.[52, 53] There have also been attempts to laterally excite the shear mode in highly oriented films (mainly used for longitudinal modes) demonstrating poor shear mode electromechanical performance thus far.[40, 54] However such piezoelectric films excite the longitudinal mode efficiently, and such films are already in use for large scale fabrication for filters.[55–57] For example Avago Technologies Ltd produces more than 1 billion longitudinal mode filters annually.[58] For this reason, the possibility of using the longitudinal mode for real-time biosensing is still desired.

Carbon nanotubes (CNTs) are among the most attractive carbon based structures due to their extraordinary mechanical and electrical properties.[59] They demonstrate high electrical and thermal conductivities, high in-axis elastic constant and low mass density.[59] These characteristics make them suitable for a large variety of applications ranging from interconnects to biological sensors. In addition their high surface to volume ratio and the possibility of being easily functionalised ensure that CNT forests perform as both an electrode and a sensing layer simultaneously. In most of these cases CNTs are either used in a tangled-like form or composing a dispersion or composite or alternatively they can be used as vertically aligned forests for electro-acoustic sensors.[60, 61]. Several works have combined CNTs on thin-film BAW resonators although very few works have fully exploited the benefits of CNTs in gravimetric resonators for real-time biosensing.

1.2 Thesis aims and outline

The objectives of this thesis are to improve the film quality and uniformity for TSM BAW resonators and to investigate the potential of minimising TLM damping in liquids. The thesis is divided in six chapters, and in Chapter 2, the background information for BAW resonators and the origin of the shear mode to use in liquid are described. Chapter 3 is a description of the deposition of inclined *c*-axis ZnO for shear mode resonances using different textured surfaces to achieve homogeneous inclination angles. Chapter 4 explores the use of carbon nanotubes (CNTs) to provide an acoustic mismatch that reduces TLM damping in liquid. This chapter also describes the optimisation of CNTs with different morphologies on the active area of the BAW resonators, and assesses the TLM and TSM performances in deionised (DI) water. Chapter 5 aims to demonstrate the performance of the sensors fabricated, and biosensing experiments to detect antibodies and cancer biomarkers. A summary of the key results achieved in this work and potential future works are provided in Chapter 6.

Chapter 2

Bulk acoustic wave resonators

This chapter begins with an introduction to the different categories of thin film BAW resonators. The piezoelectric effect in hexagonal crystals is then introduced to describe the transduction between electrical and mechanical energy, which forms the basis of the resonant behaviour and its use in high frequency acoustic wave devices. Wave propagation in thickness excited BAW resonators is then described and the polarised waves in inclined *c*-axis piezoelectric materials are detailed. Models based on acoustic transmission line and equivalent circuits are explained. The gravimetric sensing principles of BAW resonators are outlined. Common materials used for piezoelectric layer, electrodes and acoustic reflectors are then compared. Finally the implications of operating in liquid and the associated damping factors are discussed. The current technology achieved with carbon nanotube (CNT) integration in BAW resonators is given as a prelude to their effect in BAW resonators operating in liquids.

2.1 Electrical performance of BAW resonators

Thin-film BAW resonators are based on the conversion of electrical energy to acoustic energy in a thin piezoelectric material. The most basic resonator is a piezoelectric layer "sandwiched" between two electrodes.[29, 57] A standing wave is generated in the layer at resonance, which occurs at a frequency dependent on the material properties and device geometry.[62] Different environmental conditions such as the mass load, temperature and viscosity of the medium affect this frequency of resonance.[33, 63] The changes in those parameters can be sensed by tracking the shifts as discussed in section 2.7. The input electrical impedance, Z_{in} of a simple BAW resonator shown in Figure 2.1 has two resonances. At the resonant frequency, f_r, the magnitude of Z_{in} tends to its minimum value, which is ideally zero.[62, 64] Conversely at the anti-resonant frequency, f_a, the magnitude of Z_{in} tends to infinity. In addition the phase between resonant frequencies is $90°$, which indicate that the resonator behaves as an inductor within the resonance region, whereas at other frequencies, the phase is $-90°$, where the resonator behaves as a capacitor.[64] Measurement data often involve the scattering parameters, either the reflection coefficient, S_{11} for 1-port devices or the forward voltage gain S_{21} for 2-ports devices (with RF signal at input and measured at output). Z_{in} is related to S_{11} and S_{21} by the relations given by equation (2.1)

$$S_{11} = \frac{Z_{in} - Z_0}{Z_{in} + Z_0}, \qquad S_{21} = \frac{Z_0}{Z_{in} + Z_0} \tag{2.1}$$

where Z_0 is characteristic impedance, which is usually $50\,\Omega$. Assuming negligible effect from the electrode thickness, the first harmonic, f_r of a resonator with thick-

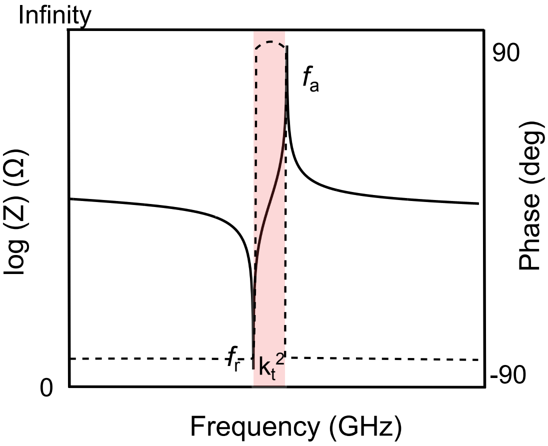

Figure 2.1: Electrical impedance curve of a typical BAW resonator showing the resonant, f_r and anti-resonant f_a frequencies, the red shaded region represent the frequency spacing indicating the piezoelectric coupling coefficient, k_t^2 of the resonator.

ness, t_p and acoustic velocity v can be approximated using equation (2.2) [13]:

$$f_{r,0} \approx \frac{v}{2t_p} \tag{2.2}$$

Additional harmonics are present at frequencies that are odd multiple of the $f_{r,0}$ [64]:

$$f_{r,n} = (2n+1)f_{r,0} \tag{2.3}$$

where n is the harmonic number. Several important electromechanical parameters are considered when characterising the performance of BAW resonators. Among them is the quality-factor, Q, which is the relative measure of the amount of energy stored in the resonator to the energy dissipated through losses from the acoustic wave to the surrounding medium.[13, 65]

$$Q = \frac{\omega \times \text{Stored energy}}{\text{Dissipated energy per cycle}} \tag{2.4}$$

where ω is the angular frequency, $2\pi f$. A well-known definition of the Q value at f_r and f_a is given by [62, 64]:

$$Q_{r,a} = \frac{f_{r,a}}{2} \left| \frac{\mathrm{d}\angle Z_{in}}{\mathrm{d}f} \right|_{f=f_{r,a}} \tag{2.5}$$

where $\mathrm{d}\angle Z_{in}/\mathrm{d}f$ is the derivative of the phase of Z_{in} with respect to frequency. A high Q causes sharp resonances in the frequency response of Z_{in}. Therefore smaller resonant frequency shifts, Δf_r, owing to smaller surface perturbations can be monitored, thus enhancing the sensitivity and mass resolution of the device.[66, 67] In a practical resonator, there are losses associated with the device and hence the achievable Q value is limited.[68] The Q value at the resonance frequency, Q_r is lower than at the anti-resonance frequency Q_a, since there is a strong influence of electrical (ohmic) losses at resonance. Acoustic losses and hence the power dissipated in the material are proportional to f^2 leading to lower Q value at higher frequencies.[62] Mechanical losses are investigated with Q_a and therefore acoustic leakage through other attached layers and spurious modes can be characterised. Electrical losses on the other hand are analysed using Q_r, and is dependent on the electromechanical conversion efficiency.

The electromechanical coupling constant, k_t^2, is conversion efficiency of electrical energy to mechanical energy and vice-versa in the piezoelectric material.[64, 69] This parameter is based on the definition of the internal energy for a piezoelectric body given by [70]:

$$k_t^2 = \frac{U_m^2}{U_e U_d} \tag{2.6}$$

where U_m is the mutual energy (energy transduction from electric to elastic energy in the piezoelectric material), U_e is the elastic energy and U_d is the electric energy. The value of k_t^2 is maximised when U_m is maximum. In practice, the k_t^2 of a BAW resonator can be estimated using the effective coupling coefficient, k_{eff}^2, of the resonator using [64, 71]:

$$k_{\mathit{eff}}^2 = \frac{\pi f_r}{2 f_a} \frac{1}{\tan\left(\frac{\pi f_r}{2 f_a}\right)} \tag{2.7}$$

An approximation based on the Taylor's series for equation (2.7) when f_a and f_r are not significantly different can also be used:

$$k_{\mathit{eff}}^2 = \frac{\pi^2 f_r}{4 f_a} \left(\frac{f_a - f_r}{f_a}\right) \tag{2.8}$$

k_{eff}^2 is a measure of the strength of coupling between the acoustic and electric fields in the resonator structure as a whole.[62] For a BAW resonator with ideal (infinitesimally thin, perfectly conducting) electrodes, $k_{\mathit{eff}}^2 = k_t^2$. For practical resonators, k_{eff}^2 depends on the electrode (geometry and thickness) and the reflector stack layer configurations.[62, 71] Therefore, in practice k_{eff}^2 differs from k_t^2. In some circumstances, k_{eff}^2 could be even larger than k_t^2 of the piezoelectric material used, depending on the thickness of electrodes and materials.[64]

2.2 Types of BAW resonators

Film bulk acoustic resonators (FBARs) and solidly mounted resonators (SMRs) are the two main types of BAW devices.[72] FBARs are membrane structures with air (low acoustic impedance) for isolation whereas SMRs have multi-layer acoustic reflectors for acoustic energy confinement.[73] Simple models of FBARs and SMRs are shown in Figure 2.2.

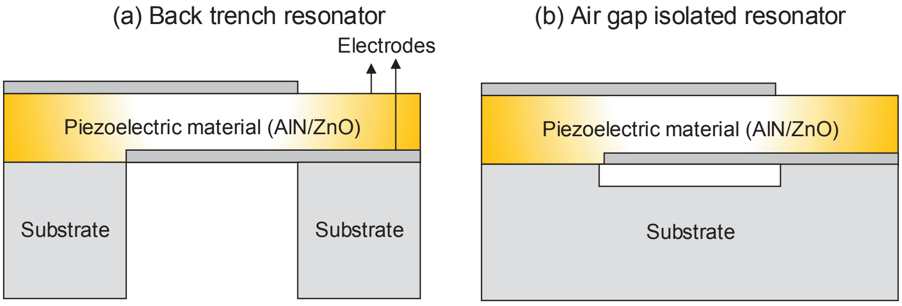

(a) Back trench resonator

(b) Air gap isolated resonator

(c) Solidly mounted resonator

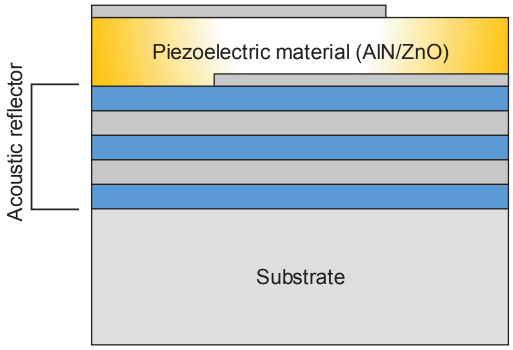

Figure 2.2: Topologies of thin-film bulk acoustic wave resonators (FBARs) showing the back trench FBAR with the substrate etched completely in (a), air-gap isolated FBAR using surface micromachining to etch a sacrificial layer or etching the substrate partially in (b) and more robust solidly mounted resonator (SMR) comprising of an acoustic reflector with alternating layers of high and low acoustic impedances in (c).

Free-standing FBARs shown in Figure 2.2 (a) and (b) have a piezoelectric layer between two electrodes suspended in air. The back trench FBAR is fabricated by etching the substrate completely whereas in the air-gap isolated FBAR, a sacrificial layer is deposited prior to the electrodes, and this sacrificial layer is etched isotropically to form a very thin air-gap underneath the piezoelectric film. Alternatively the substrate is partly etched through via-holes.[64, 71] Although the back trench and air-gap resonators are the simplest configuration, these structures are mechanically weak as the released membranes break easily due to residual stress.[55, 74] Comparatively the reflector stack of SMRs is fabricated by alternating between materials of high acoustic impedance and low acoustic impedance.[29, 75] Each layer has a thickness of a quarter of the acoustic wavelength, λ.[72] At each layer interface of the Bragg reflector, a part of the acoustic wave energy is reflected. The latter causes the wave amplitude to diminish with depth into the reflector. The number of layers in the Bragg reflector needed for complete wave reflection is determined by their acoustic impedance ratio and the quality of the interfaces. Although SMRs require additional manufacturing processes and design optimisation compared to FBARs, their purely additive fabrication is an attractive option for integrated sensor designs.[76] However biosensors based on the membrane types FBARs enable manufacturing of a microfluidic channel within the substrate underneath the FBAR for convenient transportation of samples to the bottom electrode, which acts as the sensor surface.[77, 78] The latter configuration is advantageous, in that it minimises parasitic fringe capacitances and dielectric losses, and the contacts can be made at the top electrode, which decouple the electrical signal from the liquid.[48]

The mechanical losses in SMRs mainly include acoustic leakage to the substrate, laterally escaping waves, viscous losses and wave scattering at the piezoelectric-electrode interface.[79, 80] Except for acoustic leakage to the substrate, all other loss mechanisms are associated with both FBARs and SMRs. In most cases the additional layers will reduce the relative spacing between f_r and f_a. A proper choice of electrodes, and the quality of the piezoelectric layer are necessary to have high k^2_{eff} as will be explained in section 2.8.[55] Moreover a rough bottom electrode significantly degrades coupling due to scattering of the acoustic wave. Thus, the smoothening of the bottom electrode is also important, which is commonly achieved by mechanical polishing of the final reflector layer. For SMRs with metal layers in the Bragg reflector, an additional parasitic capacitive coupling with the contact pads will reduce the coupling coefficient further.[81] This parasitic coupling can be eliminated by patterning of the Bragg reflector as proposed in [82] or by using a dielectric reflector.[57, 83, 84]

2.3 Piezoelectricity in hexagonal crystals

The operation of FBARs and SMRs is dependent on the ability of the piezoelectric materials to generate a mechanical deformation in response to an applied electrical field —the reverse piezoelectric effect.[85] In this section, the piezoelectric effect leading to the generation of acoustic waves in BAW resonators is outlined. The nature of the piezoelectric effect is closely related to the occurrence of electric dipole moments in solids. The latter may either be induced for ions on crystal lattice sites with asymmetric charge surroundings or may directly be carried by molecular groups.[85] The piezoelectric effect occurs when the charge balance within the crystal lattice is disturbed. When there is no applied stress on the material, the positive and negative charges are evenly distributed so there is no potential difference. When the lattice is changed slightly the charge imbalance creates a potential difference, often as high as several thousand volts.[86] However, the current is extremely small and only causes a small electric shock. The reverse piezoelectric effect occurs when the electrostatic field created by electrical current causes the atoms in the material to move slightly. In piezoelectric materials, the Maxwell's equations and Christoffel's equation are coupled with each other by the piezoelectric strain equations:

$$\begin{aligned}\mathbf{D} &= \boldsymbol{\epsilon}^{\boldsymbol{T}} : \mathbf{E} + \boldsymbol{d} : \mathbf{T} \\ \mathbf{S} &= \boldsymbol{d} : \mathbf{E} + \boldsymbol{s}^{\boldsymbol{E}} : \mathbf{T}\end{aligned} \tag{2.9}$$

where $\mathbf{D}$ is the electric field displacement, $\mathbf{E}$ is the electric field, $\mathbf{S}$ is the strain and $\mathbf{T}$ is the stress. The piezoelectric-stress equations are given by:

$$\begin{aligned}\mathbf{T} &= \boldsymbol{c}^{\boldsymbol{E}} : \mathbf{S} - \boldsymbol{e} : \mathbf{E} \\ \mathbf{D} &= \boldsymbol{e} : \mathbf{S} + \boldsymbol{\epsilon}^{\boldsymbol{S}} : \mathbf{E}\end{aligned} \tag{2.10}$$

where $\boldsymbol{\epsilon}^{\boldsymbol{T}}$ is the clamped dielectric constant, $\boldsymbol{d}$ is the piezoelectric strain constant, $\boldsymbol{s}^{\boldsymbol{E}}$ is the elastic compliance coefficient, $\boldsymbol{c}^{\boldsymbol{E}}$ is the elastic stiffness constant in constant strain, $\boldsymbol{e}$ is the piezoelectric stress constant. The parameters in bold indicate the anisotropy, ":" implies matrix multiplication and superscripts indicate the parameter that is kept constant. Using piezoelectric hexagonal crystals such as aluminium nitride (AlN) and zinc oxide (ZnO) as examples, the elastic stiffness in constant strain (constant electric field) is given by:

$$\boldsymbol{c^E} = \begin{bmatrix} c_{11}^E & c_{12}^E & c_{13}^E & 0 & 0 & 0 \\ c_{12}^E & c_{11}^E & c_{13}^E & 0 & 0 & 0 \\ c_{13}^E & c_{13}^E & c_{33}^E & 0 & 0 & 0 \\ 0 & 0 & 0 & c_{44}^E & 0 & 0 \\ 0 & 0 & 0 & 0 & c_{55}^E & 0 \\ 0 & 0 & 0 & 0 & 0 & c_{66}^E \end{bmatrix} \tag{2.11}$$

the piezoelectric stress constant is given by:

$$\boldsymbol{e} = \begin{bmatrix} 0 & 0 & 0 & 0 & e_{15} & 0 \\ 0 & 0 & 0 & e_{25} & 0 & 0 \\ e_{e31} & e_{32} & e_{33} & 0 & 0 & 0 \end{bmatrix} \tag{2.12}$$

and the clamped dielectric constant is given by:

$$\boldsymbol{\epsilon^S} = \begin{bmatrix} \epsilon_{11}^S & 0 & 0 \\ 0 & \epsilon_{22}^S & 0 \\ 0 & 0 & \epsilon_{33}^S \end{bmatrix} \tag{2.13}$$

A full derivation of the plane wave solutions of the Christoffel matrix for thickness excited BAW resonator is provided by Zhang and Chen [69] and it is given by equation (2.14):

$$\left[\frac{k}{\omega}^2 \left(c_{33}^E + \frac{e_{33}^2}{\epsilon_{33}^S}\right) - \rho\right] \left[\left(\frac{k}{\omega}\right)^2 c_{44}^E - \rho\right]^2 = 0 \tag{2.14}$$

where ρ is the density of the material and k is the propagation wavevector given by $2\pi/\lambda$, with λ being the wavelength of the acoustic wave. Since $\omega = vk$, the acoustic velocities, v, can be solved from equation (2.14). The first solution is the pure longitudinal wave with a phase velocity, v_L, which propagates along the c-axis of the hexagonal crystal. This longitudinal velocity is given by

$$v_L = \sqrt{\frac{c_{33}^E + e_{33}^2/\epsilon_{33}^S}{\rho}} \tag{2.15}$$

The second and third solutions are the waves that have orthogonal polarisations and propagate normal to the *c*-axis. These are the pure shear modes, with phase velocities, v_S and they are independent from the piezoelectric constants; they depend only on the stiffness and density.[69]

$$v_S = \sqrt{\frac{c_{44}^E}{\rho}} \tag{2.16}$$

2.4 Shear and longitudinal waves

The two general types of wave propagation in BAW resonators —the longitudinal and the shear wave —are different in the particle displacement and wave propagation direction. Particle displacement is parallel to the propagating wave vector in the case of the longitudinal mode, whereas for a shear mode, this particle displacement is in a direction normal to the wave propagation axis as shown in Figure 2.3.

In-liquid BAW sensing applications typically employ thickness shear (TS) mode acoustic waves. For such a structure, the top sensing surface moves side to side, parallel to the sensor-liquid boundary. Energy is not effciently coupled across this boundary, as fluids do not support shear wave propagation modes.[87] The mechanical action is therefore minimally degraded by energy loss. Bjurström *et al.* [88] have demonstrated a 1.6 GHz membrane FBAR operated with one face in air and one face in water, which caused a 60% degradation in the transduction efficiency.[88] TS modes can be excited in an FBAR structure using two common methods. The first is to grow a ZnO or AlN film whose columnar, piezoelectric *c*-axis is inclined with respect to substrate normal.[48, 50] When a normal electric field is applied, both the shear and the longitudinal modes can be excited. The alternate method is to use lateral field excitation, in which electrodes are applied on either side of the resonator surface, instead of through its bulk. This produces a lateral electric field within the piezoelectric layer, which can excite TSM waves within the bulk

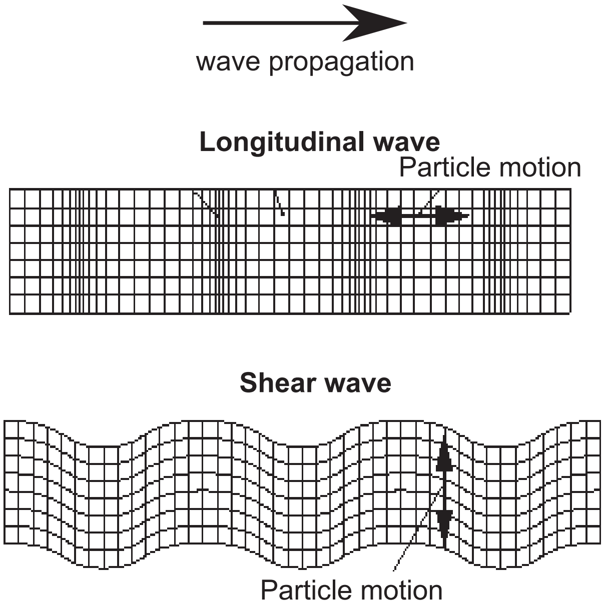

Figure 2.3: Longitudinal and shear wave propagation, with particle displacement being parallel to the propagation wave vector in the longitudinal wave whereas the particle displacement is perpendicular to the propagation vector for a shear wave.

material. This method has been employed by Dickherber *et al.* [54] and Corso *et al.* [40] to demonstrate aqueous biosensing. In practice, the electric fields between the coplanar electrodes are weak, and excited shear modes have low electromechanical coupling coefficients (<0.01%) in SMRs.[89, 90]

For a thickness longitudinal (TL) mode acoustic wave, particle displacement within the bulk is parallel to the wave propagation axis. Wave propagation comprises alternating peaks and troughs of higher and lower density material planes, forming a compression in the material. For BAW resonators, the TLM has been employed commonly in both RF applications and gas-based sensing applications.[91–93] This is due in part to the straightforward deposition of ZnO and AlN with a piezoelectric *c*-axis normal to the substrate. Additionally, the longitudinal mode for a given crystal has a higher phase velocity than does the shear mode, yielding higher frequency devices for a given thickness [62]; this is advantageous for both RF and sensing applications. While longitudinal mode resonators are rarely used in a liquid environment, aqueous TLM operation using the second harmonic has been demonstrated by Zhang and Kim [78] using a ZnO resonator on a thin silicon nitride support membrane achieving 88% energy loss compared to 94% using the fundamental mode. Xu *et al.* [77] have demonstrated a method to confine a very thin fluid layer at the resonator surface. This microfluidic layer is thick enough to be useful as a sensing layer, with a thickness of 4-5 µm, but it is thin enough that energy cannot be effectively coupled into the fluid layer.[94] This mitigates the commonly observed Q value degradation and suggests that TLM operation can be potentially used for in-liquid sensing

2.5 Quasi-shear and quasi-longitudinal waves

Pure TLM is excited when the *c*-axis is parallel to the E-field, whereas a pure TSM is excited when the *c*-axis is perpendicular. However a piezoelectric film can generally excite both longitudinal and shear waves simultaneously, when the *c*-axis is inclined from the E-field at an angle, χ as shown in Figure 2.4. The derivation of inclined *c*-axis ZnO and CdS was carried out by Foster *et al.* [95]. Depending on the inclination of the *c*-axis with respect to the resonator normal, which is generally parallel to the applied E-field, and depending at which frequency the resonator is excited, longitudinal or shear wave modes are predominately excited. In inclined c-axis films, the modes are polarised at an angle, α. This polarisation is also neither exactly aligned with nor exactly perpendicular to the propagation direction and therefore not exactly equal to χ as shown in Figure 2.4 (b).[33, 95] At different values of χ (from 0 to 90°) for inclined c-axis ZnO, α ranges from 2° to $-5°$, implying that the difference between particle displacement direction and the wave vector is not substantial.[96] Accordingly the displacement of the particles is a neither pure shear mode nor a pure longitudinal wave mode. For this reason they are called quasi-longitudinal and quasi-shear mode respectively.

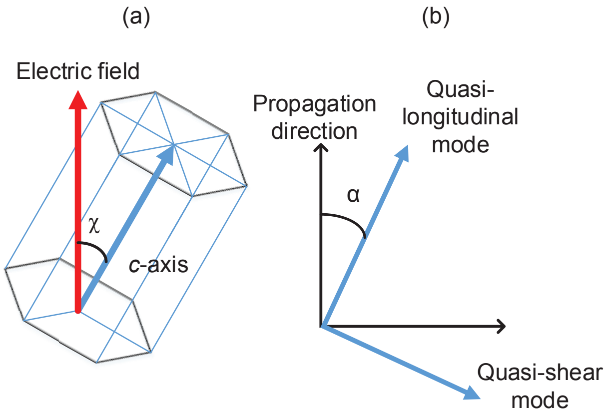

Figure 2.4: (a) The inclination of the c-axis relative to electric field of hexagonal crystal. (b) the polarisation angle α with respect to the propagation direction and the actual propagation direction of the quasi-longitudinal and quasi-shear modes. The modes are neither parallel nor perpendicular to the propagation vector.

The coefficients of the elastic stiffness of inclined c-axis piezoelectric materials are modified to [95]:

$$\begin{aligned}
c'_{33} &= c^E_{33}\cos^4\chi + 2(c^E_{13} + 2c^E_{55})\sin^2\chi\cos^2\chi + c^E_{11}\sin^4\chi \\
c'_{55} &= c^E_{55}(\cos^4\chi + \sin^4\chi) + (c^E_{11} + c^E_{33} - 2(c^E_{13} - 2c^E_{55})\sin^2\chi\cos^2\chi \\
c'_{35} &= \sin\chi\cos\chi\left[(c^E_{11} - 2c^E_{55} - c^E_{13})\sin^2\chi + (c^E_{13} + 2c^E_{55} - c^E_{33})\cos^2\chi\right]
\end{aligned} \tag{2.17}$$

and the piezoelectric stress coefficients are changed to [95]:

$$\begin{aligned} e'_{33} &= \cos\chi\left[(e_{31}+e_{15})\sin^2\chi + e_{33}\cos^2\chi\right] \\ e'_{55} &= -\sin\chi\left[e_{15}\sin^2\chi + (e_{33}-e_{31}-e_{15})\cos^2\chi\right] \end{aligned} \tag{2.18}$$

The clamped dielectric constant, which is the modification due to the inclined c-axis is given by:

$$\epsilon'_{33} = \epsilon^S_{11}\sin^2\chi + \epsilon^S_{33}\cos^2\chi \tag{2.19}$$

The piezoelectrically stiffened elastic constants of the inclined c-axis materials is then given by [95, 96]:

$$\begin{aligned} c^*_{55} &= c'_{55} + \frac{e'_{35}}{\epsilon'_{33}} \\ c^*_{35} &= c'_{35} + \frac{e'_{35}e'_{33}}{\epsilon'_{33}} \\ c^*_{33} &= c'_{33} + \frac{e'_{33}}{\epsilon'_{33}} \end{aligned} \tag{2.20}$$

For non-piezoelectric and anisotropic materials, these modified elastic constants are only equation (2.17) as the piezoelectric stress constants of the matrix, $\boldsymbol{e}$, are zero. The quasi-longitudinal and quasi-shear velocities of the inclined c-axis crystal are given by:

$$v_L = \left[\frac{c^*_{33}+c^*_{55}}{2\rho} + \sqrt{\left(\frac{c^*_{33}-c^*_{55}}{2\rho}\right)^2 + \left(\frac{c^*_{35}}{\rho}\right)^2}\right]^{\frac{1}{2}} \tag{2.21}$$

$$v_S = \left[\frac{c^*_{33}+c^*_{55}}{2\rho} - \sqrt{\left(\frac{c^*_{33}-c^*_{55}}{2\rho}\right)^2 + \left(\frac{c^*_{35}}{\rho}\right)^2}\right]^{\frac{1}{2}} \tag{2.22}$$

which leads to a Z_{in} of a simple transducer with thickness t and with infinitesimal electrode thickness given by:

$$Z_{in} = \frac{1}{j\omega C}\left[1 - k_L^2\frac{\tan(\omega t/v_L)}{\omega t/v_L} - k_S^2\frac{\tan(\omega t/v_S)}{\omega t/v_S}\right] \tag{2.23}$$

where the electromechanical coupling coefficients of the quasi-longitudinal , k_L^2 and quasi-shear k_S^2 modes are given by:

$$k_L^2 = \frac{(e'_{33}\cos\alpha + e'_{35}\sin\alpha)^2}{\epsilon'_{33}\rho v_L^2} \tag{2.24}$$

$$k_S^2 = \frac{(e'_{35}\cos\alpha - e'_{33}\sin\alpha)^2}{\epsilon'_{33}\rho v_S^2} \tag{2.25}$$

α is given by:

$$\alpha = \arctan\left(\frac{2c^*_{35}}{c^*_{33} - c^*_{55}}\right) \tag{2.26}$$

This angle shows that the displacement is inclined with respect to the propagation direction. The quasi-shear and quasi-longitudinal velocities of a typical ZnO material at different χ are plotted in Figure 2.5 (a) showing that the ratio of the TL to TS modes is different at different χ. In inclined c-axis films, the TS mode is most effectively excited at $\chi = 32°$ whereas the TL mode has the highest electromechanical coupling at $\chi = 0°$. In contrast, AlN has higher acoustic velocities but smaller electromechanical coupling coefficients as shown in Figure 2.6.

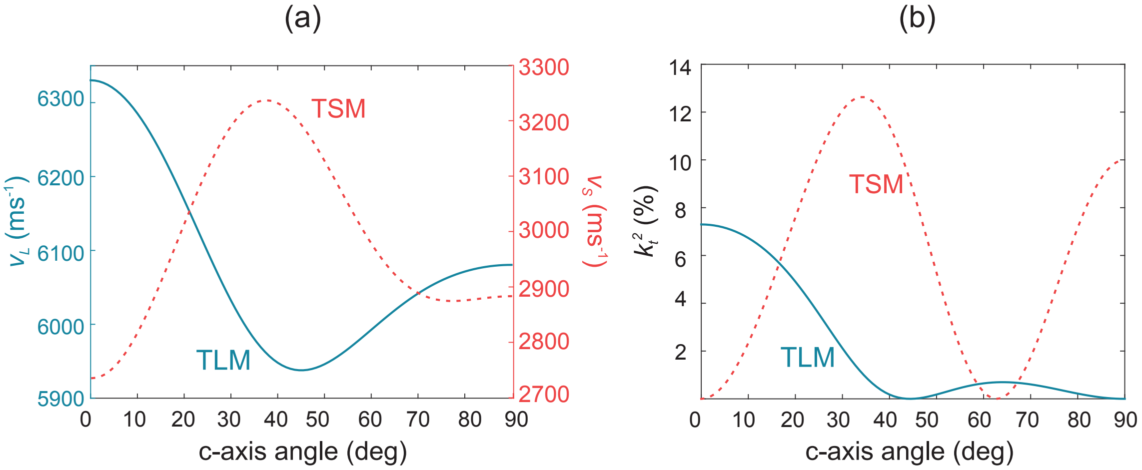

Figure 2.5: (a) The quasi-shear wave velocity and quasi-longitudinal wave velocity of inclined c-axis ZnO at different c-axis angles. (b) shows the electromechanical coupling of the quasi-shear and quasi-longitudinal modes with different c-axis angles for ZnO. The graphs demonstrate that the highest TSM velocities and k_t^2 are obtained at angles ranging from $\chi = 30 - 45°$.

For isotropic materials and non-piezoelectric materials, the acoustic velocities of

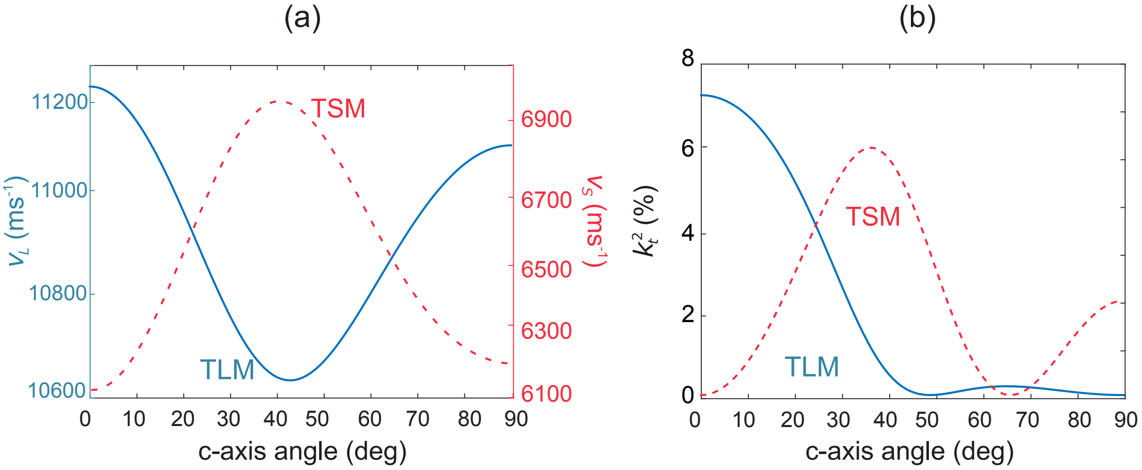

Figure 2.6: (a) The quasi-shear wave velocity and quasi-longitudinal wave velocity of inclined *c*-axis AlN at different *c*-axis angles. (b) shows the electromechanical coupling of the quasi-shear and quasi-longitudinal modes with different *c*-axis angles for AlN. The graphs demonstrate that the highest TSM velocities and k_t^2 are obtained at angles ranging from $\chi = 30 - 45°$.

the pure modes are calculated using [85]:

$$v_{L,p} = \sqrt{\frac{E(1-\nu)}{\rho(1+\nu)(1-2\nu)}}, \qquad v_{S,p} = \sqrt{\frac{E}{2\rho(1+\nu)}} \tag{2.27}$$

where E is the Young modulus and ν is the Poisson ratio. The quasi-shear and quasi-longitudinal velocities in such materials are then determined using:

$$v_L = v_{L,p}\cos\chi + v_{S,p}\sin\chi \tag{2.28}$$

$$v_S = v_{L,p}\sin\chi + v_{S,p}\cos\chi \tag{2.29}$$

The acoustic impedance, Z in Rayl (kg/(s m^2)), of a material can be calculated from:

$$Z = \rho v \tag{2.30}$$

For a resonator with active area, A, the acoustic impedance caused by this material in the BAW resonator, Z_a in (kg/s) is given by the product of the corresonding acoustic velocity and the density:

$$Z_a = A\rho v \tag{2.31}$$

2.6 One dimensional model of acoustic resonators

One-dimensional models using equivalent circuits are necessary to correctly design BAW resonators and to understand the impact of the different layers on the frequency response of the devices. With the well-known electrical transmission line model, the acoustic properties of the materials can be modelled using acoustic impedance and propagation constants. In the first case the transmission line model of a non-piezoelectric block is considered before the Mason model is used for the piezoelectric slab. Such one dimensional models assume that the piezoelectric layer is infinite in its lateral dimensions, thereby only thickness excited waves are present.

2.6.1 Transmission line model

The mechanical displacement in the z direction, $u(z)$ of a non-piezoelectric material can be expressed as:

$$\frac{\partial^2 u}{\partial z^2} = \frac{\rho}{C}\frac{\partial^2 u}{\partial t^2} \tag{2.32}$$

where C is the modulus of elasticity. For a lossless, isotropic, charge-free material, there are two different mechanical waves that propagate —an incident and a reflected —which can be expressed as:

$$u(z) = [A^+ \exp(-jkz) + A^- \exp(+jkz)] \tag{2.33}$$

where A^+ is the amplitude of the incident wave and the A^- is the amplitude of the reflected wave, with the term k being the wave number, defined as $k = \omega/v$. The first case considers a non-piezoelectric material as shown in Figure 2.7 (a), which has a thickness, t, with an applied force F_1 causing a particle velocity v_1 and force F_2 causing a particle velocity v_2.

By solving equation (2.33) between the boundaries z_1 and z_2, F_1 and F_2 can be

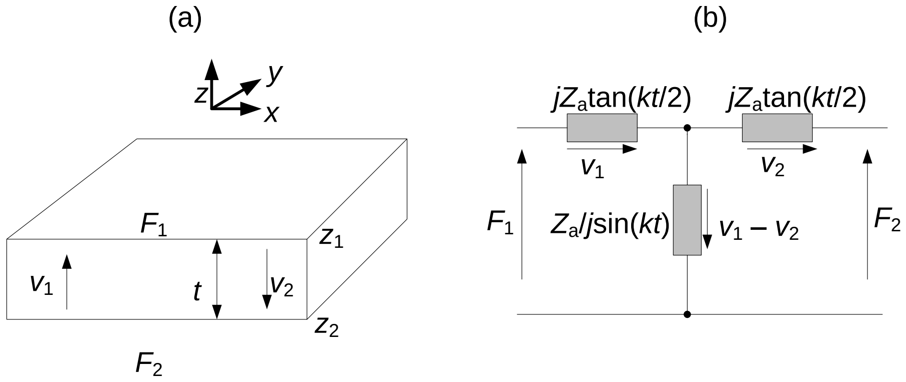

Figure 2.7: (a) A non piezoelectric slab with thickness t, showing the force and displacement directions at each interface, (b) Transmission line model for a non-piezoelectric layer, representing the acoustic impedances and relation between the input and output port.

expressed as [97]:

$$
\begin{aligned}
F_1 &= \frac{Z_a}{j\sin(kt)}(v_1 - v_2) + jZ_a \tan\left(\frac{kt}{2}\right) v_1 \\
F_2 &= \frac{Z_a}{j\sin(kt)}(v_1 - v_2) - jZ_a \tan\left(\frac{kt}{2}\right) v_2
\end{aligned}
\tag{2.34}
$$

with Z_a being the acoustic impedance of the material. Furthermore this can be represented as a circuit model as shown in Figure 2.7 (b), which is a classic distributed T-impedance equivalent network for a transmission line.[98] If the applied force, F, is related to the electrical voltage V, and the particle velocity to the current, I, the non-piezoelectric material can be considered as an acoustic transmission line. An easier way to represent equation (2.34) is by using $ABCD$ matrices, which is given by [69, 99]:

$$
\begin{bmatrix} F_1 \\ v_1 \end{bmatrix} = \begin{bmatrix} \frac{a+b}{b} & 2a + \frac{a^2}{b} \\ \frac{1}{b} & \frac{a+b}{b} \end{bmatrix} \begin{bmatrix} F_2 \\ v_2 \end{bmatrix} = \mathbf{M} \begin{bmatrix} F_2 \\ v_2 \end{bmatrix} \tag{2.35}
$$

where the acoustic impedances a and b are given by:

$$a = jZ_a \tan\left(\frac{kt}{2}\right) \tag{2.36}$$

$$b = \frac{Z_a}{j\sin(kt)} \tag{2.37}$$

and the $ABCD$ transmission matrix, $\mathbf{M}$, of this layer can be simplified using trigonometric identities to give [69, 100]:

$$\mathbf{M} = \begin{bmatrix} \cos(kt) & jZ_a\sin(kt) \\ \frac{j\sin(kt}{Z_a} & \cos(kt) \end{bmatrix} \tag{2.38}$$

The non-piezoelectric materials in a BAW resonator such as the electrodes, reflector layers and substrate are represented by this transmission matrix.

The equivalent circuit for piezoelectric materials is given by the Mason model.[101] An electrical port consisting of V and I is used to represent the application of an electric field through the piezoelectric slab (Figure 2.8 (a)), and transformer turn ratio hC_0 to demonstrate the electrical to mechanical energy as shown in Figure 2.8 (b).

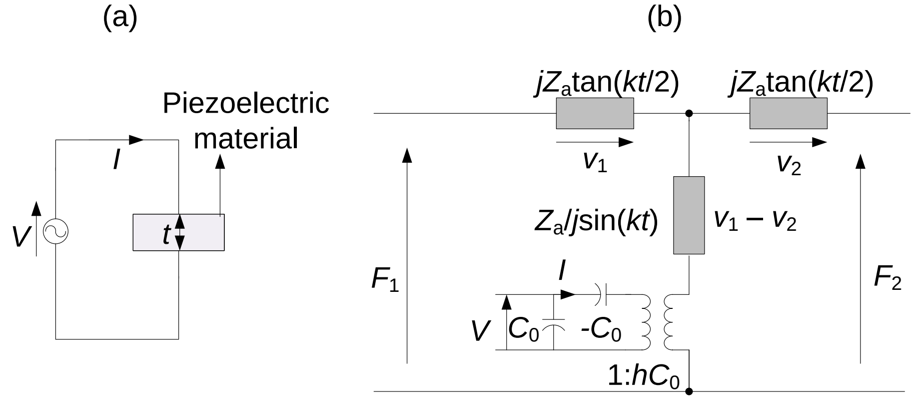

Figure 2.8: (a) A representation of the ac voltage and current through a piezoelectric layer, (b) the Mason model of the piezoelectric layer and its relation with the transmission line model.

The static capacitance, C_0 is given by:

$$C_0 = \frac{\epsilon^S A}{t} \tag{2.39}$$

and h represents the electromechanical energy conversion ratio given by e/ϵ^S, where e is the piezoelectric stress constant and ϵ^S is the dielectric constant. Considering the stress equations 2.10, the corresponding forces and particle velocities for a piezoelectrically active material are given by [97]:

$$\begin{aligned} F_1 &= \frac{Z_a}{j\sin(kt)}(v_1 - v_2) + jZ_a \tan\left(\frac{kt}{2}\right) v_1 + \frac{h}{j\omega} I \\ F_2 &= \frac{Z_a}{j\sin(kt)}(v_1 - v_2) - jZ_a \tan\left(\frac{kt}{2}\right) v_2 + \frac{h}{j\omega} I \end{aligned} \tag{2.40}$$

This one-dimensional model leads to a piezoelectric layer with a transmission matrix of the form [69]:

$$\begin{bmatrix} V \\ I \end{bmatrix} = \begin{bmatrix} 1 & 0 \\ j\omega C_0 & 1 \end{bmatrix} \begin{bmatrix} 1 & -\frac{1}{j\omega C_0} \\ 0 & 1 \end{bmatrix} \begin{bmatrix} \frac{1}{hC_0} & 0 \\ 0 & hC_0 \end{bmatrix} \begin{bmatrix} A & B \\ C & D \end{bmatrix} \begin{bmatrix} F_2 \\ v_2 \end{bmatrix} \tag{2.41}$$

where the $ABCD$ matrix is given in the same way as equation (2.35) for a non-piezoelectric material. The acoustical transmission line models of devices consisting of electrodes and the reflectors are illustrated in Figure 2.9 (a) and (b). FBARs are represented as a three layer structure with a piezoelectric material in between two electrodes (Figure 2.9 (a)). Conversely SMRs are represented as a multi-layer structure with the addition of reflector layers and the substrate (Figure 2.9 (b)). Subscripts in the acoustic impedances denote the layer position in the structure. If the devices have no mass loading, F_1 is zero on the top electrode. By combining the top electrode and the piezoelectric transmission line structures, a simpler circuit of a BAW resonator can be obtained as shown in Figure 2.9 (c), which provides a direct relation between the electrical and mechanical parameters through transmission line matrices. The combined transmission structure of the piezoelectric layer with the top electrode has the $ABCD$ matrix, $\mathbf{M_{piezo}}$ [69]:

$$A = \frac{a_2 + b_2 + a_1 + \frac{a_1 b_1}{a_1 + b_1}}{b_2 + a_1 + \frac{a_1 b_1}{a_1 + b_1}}, \quad B = \frac{1}{b_2 + a_1 + \frac{a_1 b_1}{a_1 + b_1}}$$

$$C = b_2 + a_2 + \frac{a_2 b_2}{a_1 b_2 + \frac{a_1 b_1}{a_1 + b_1}} \;\;,\;\; D = \frac{a_2 + b_2 + \frac{a_1 b_1}{a_1 + b_1}}{b_2 + a_1 + \frac{a_1 b_1}{a_1 + b_1}} \tag{2.42}$$

The total transmission of the device can then be calculated by multiplying the individual transmission matrices [69]:

$$\mathbf{M_{device}} = \mathbf{M_{piezo}} \times \mathbf{M_{bottom}} \times \mathbf{M_{reflectors}} \times \mathbf{M_{sub}} \tag{2.43}$$

Since all the reflector layers are designed with a thickness of $\frac{\lambda}{4}$, the value of kt becomes $\frac{\pi}{2}$, the transmission matrix of a single reflector layer, $\mathbf{M_{reflector}}$ becomes:

$$\mathbf{M_{reflector}} = \begin{bmatrix} 0 & jZ_a \\ \frac{j}{Z_a} & 0 \end{bmatrix} \tag{2.44}$$

With a pair of low acoustic impedance layer and a high impedance layer, the total reflector matrix becomes:

$$\begin{aligned} \mathbf{M_{reflectors}} &= (\mathbf{M_l} \times \mathbf{M_h})^m \\ &= \left(\begin{bmatrix} 0 & jZ_{a,l} \\ \frac{j}{Z_{a,l}} & 0 \end{bmatrix} \begin{bmatrix} 0 & jZ_{a,h} \\ \frac{j}{Z_{a,h}} & 0 \end{bmatrix} \right)^m \\ &= \begin{bmatrix} -\frac{Z_{a,l}}{Z_{a,h}} & 0 \\ 0 & -\frac{Z_{a,h}}{Z_{a,l}} \end{bmatrix}^m \end{aligned} \tag{2.45}$$

where m is the number of reflector pairs, $Z_{a,l}$ and $Z_{a,h}$ represent the acoustic impedances of the low and high acoustic impedances layers respectively. The voltage V and current I at the electric port are related to the mechanical ports F_5 and v_5 by:

$$\begin{aligned} \begin{bmatrix} V \\ I \end{bmatrix} &= \mathbf{M_{device}} \begin{bmatrix} F_5 \\ v_5 \end{bmatrix} \\ &= \begin{bmatrix} M_{device}(1,1) & M_{device}(1,2) \\ M_{device}(2,1) & M_{device}(2,2) \end{bmatrix} \begin{bmatrix} F_5 \\ v_5 \end{bmatrix} \end{aligned} \tag{2.46}$$

(a) FBAR

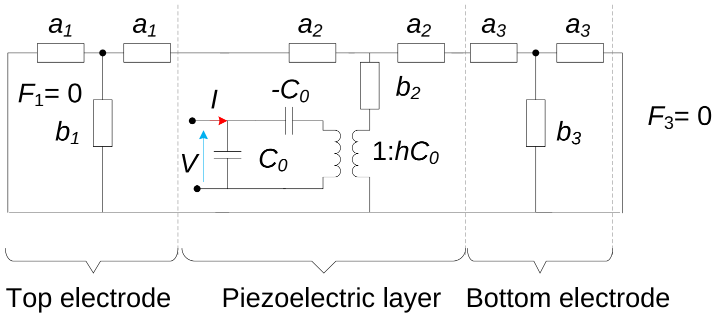

(b) SMR

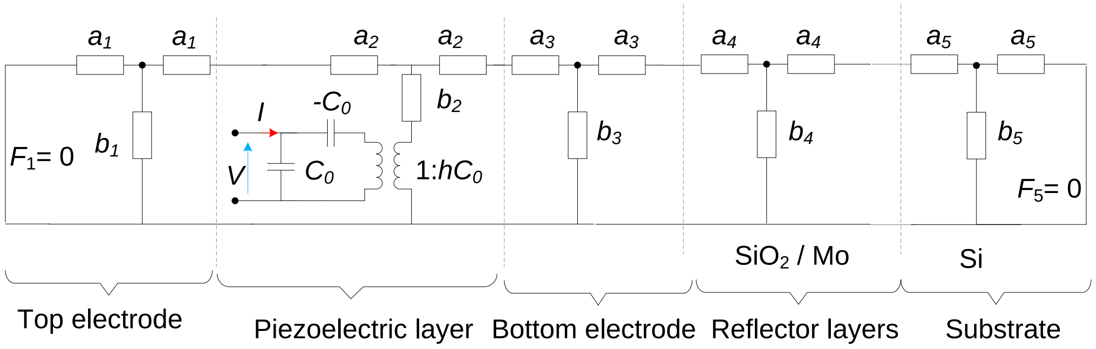

(c) Transmission line modified

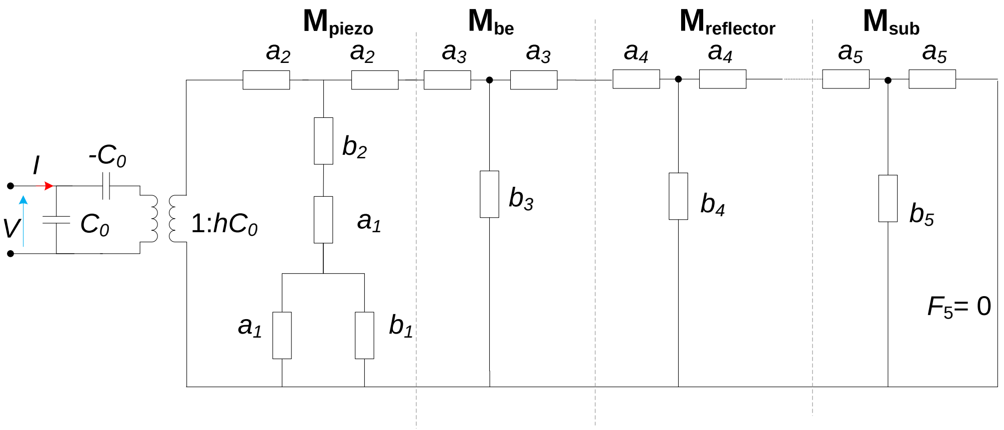

Figure 2.9: Transmission line models of FBAR in (a), SMR with reflectors and substrate in (b) and a converted transmission model for simpler analysis in (c).[69, 100]

The input electrical impedance, Z_{in} of the device can be obtained using the matrix elements of $\mathbf{M_{device}}$:

$$Z_{in} = \frac{V}{I} = \frac{M_{device}(1,1) \times F_5 + M_{device}(1,2) \times v_5}{M_{device}(2,1) \times F_5 + M_{device}(2,2) \times v_5} \tag{2.47}$$

$F_5 = 0$ if there is no mass loading on the substrate. The electrical impedance can then be obtained as matrix elements only:

$$Z_{in} = \frac{M_{device}(1,2)}{M_{device}(2,2)} \tag{2.48}$$

For FBARs, the frequency response can be obtained by removing the reflector matrix in equation (2.43). Mass loading at the top and bottom surface of a device can be modelled by setting either F_1 or F_5 to non-zero values. The mechanical impedance of the load, Z_L, is related to F_1 or F_5 by:

$$Z_L = \frac{F_1}{v_1} \text{ or } Z_L = \frac{F_5}{v_5} \tag{2.49}$$

2.6.2 Butterworth-Van-Dyke model

The classical approximation of BAW resonators is the Butterworth-Van-Dyke (BVD) model, where a RLC-circuit is in parallel with a static capacitance, C_0. A BVD circuit consists of a mechanical resonance branch (L_m, C_m, R_m) in parallel with C_0, which is simply the plate capacitance formed by the piezoelectric film or crystal sandwiched between the electrodes and is given by equation (2.39) (ignoring fringing field contribution). R_m, L_m and C_m are the motional resistance, inductance and capacitance respectively.[62] The BVD model only considers the mechanical loss of the piezoelectric films, while the medium loss and the electrode loss are not included in this model. In order to describe the electronic behavior more accurately, the modified BVD (mBVD) model is adopted. The modifications shown in Figure 2.10 by Larson *et al.* [102] include the addition of two loss resistors (R_s and R_0) to compensate for electrodes and intrinsic losses in real thin film BAW devices. A series inductance L_s is added to represent the inductance formed by the electrode layout of the resonator and the finite resistivity of the piezolayer can be described by the resistor R_p, which is usually insignificant. R_s describes the electrode resistance,

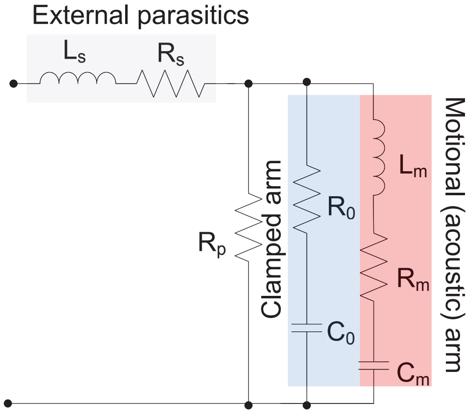

Figure 2.10: Modified Butterworth-Van-Dyke model for FBAR and SMRs demonstrating a motional arm for the piezoelectric layer, its associated intrinsic losses with a clamped arm and external parasitics caused by the presence of electrodes.

R_0 the dielectric losses in the piezoelectric layer, R_m the acoustic losses (viscosity, radiative) and R_p the finite resistance of the piezoelectric layer. According to this mBVD model, the parameters of the electrical response of BAW resonators can be approximated by [62, 64]:

$$f_r = \frac{1}{2\pi\sqrt{(L_m C_m)}} \tag{2.50}$$

$$f_a = \frac{1}{2\pi}\sqrt{\frac{(C_0 + C_m)}{L_m C_0 C_m}} \tag{2.51}$$

The k^2_{eff} is dependent on C_0, which is determined by the active area, and therefore the geometry of the resonator:

$$k^2_{\mathit{eff}} = \frac{C_m}{C_0 + C_m} \tag{2.52}$$

The Q value at resonance and anti-resonance can be approximated by:

$$Q_r \approx \frac{\omega_r L_m}{R_s + R_m} \tag{2.53}$$

$$Q_a \approx \frac{\omega_a L_m}{R_0 + R_m} \tag{2.54}$$

Q_r depends on the loaded resistance caused by the electrodes, whereas Q_a is dependent on internal losses in the piezoelectric material.[64] Q_r is the most commonly used parameter for evaluating the performance of sensors based on BAW resonators as it includes the electrodes.[62] In practical BAW resonators, Q_a is not affected by the electrode resistances or contact resistance in the measurement, and can be used to assess the mechanical losses in the piezoelectric layer. In addition a purely mechanical Q_{mech} can de defined as:

$$Q_{mech} = \frac{\omega_a L_m}{R_m} \tag{2.55}$$

Optimised Q values can be achieved by reducing R_s by suitable electrode morphology, thickness, geometry, dimension and material. The quality of the piezoelectric layer and the resonator active area determine the values of L_m, R_m and C_m.[69]

2.7 Gravimetric principle

Sensors based on BAW resonators operate by tracking the resonant frequency shift, Δf_r when there is a perturbation on the surface such as mass loading as shown in Figure 2.11 (a). This mass load causes f_r to decrease and the mass sensitivity, S_m is the resonant frequency shift per unit mass change when target molecules bind to the receptors on the surface. This parameter can be estimated from Sauerbrey's equation [38] when the mass attached on the surface of the sensor is rigid and less than 2% of the total resonator mass.[103] The higher frequency of operation and smaller dimensions of BAW resonators leads to higher sensitivities.[104] Although Sauerbrey's equation [38] for QCMs (equation (2.56)) holds approximately true for FBARs and SMRs, multi-layered structures require simulations and more precise analysis.[105] According to Wingqvist *et al.* [48] the sensitivities calculated from Sauerbrey's equation are in fact underestimates of the actual sensitivities observed in BAWs.

$$S_m = \frac{-2f_r^2}{nA\sqrt{\rho_p \mu_p}} \propto f_r^2 \tag{2.56}$$

where n is the harmonic number, A is the active area, ρ_p is the piezoelectric film density and μ_p is the film stiffness. The mass sensitivity of sensors based on frequency shifts is generally determined in practice using:

$$S_m = -\frac{1}{f_r}\frac{\Delta f}{\Delta m} \tag{2.57}$$

where Δm is the change in surface mass density (mass/area) on top of the resonator. The limit of detection (LOD), or mass resolution, m_r is the minimum mass or quantity of a target per unit area that can be sensed. It can be defined using S_m, and the minimum detectable resonant frequency shift $\Delta f_{r,min}$ as [13]:

$$m_r = \frac{\Delta f_{r,min}}{S_m} \tag{2.58}$$

The value of Δf_{min} depends not only on the resonator but also on electronic readout circuitry. A minimum mass, m_{min} that can be detected is then the product of the mass resolution and the active area, A:

$$m_{min} = m_r \times A \tag{2.59}$$

It then follows that to detect trace amounts of biochemicals, the active area should be small; it should ideally be of the same size as the target molecule.[106] Mass loading on the resonator surface is expressed through the addition of a series inductance, L_3, in the mBVD model as shown in Figure 2.11 (c) and it is given by [69, 96]:

$$L_3 = \frac{4 f_r L_m \rho_3 t_3}{\rho_p v_p} \tag{2.60}$$

where ρ_3 and t_3 are the density and thickness of the coating layer respectively.

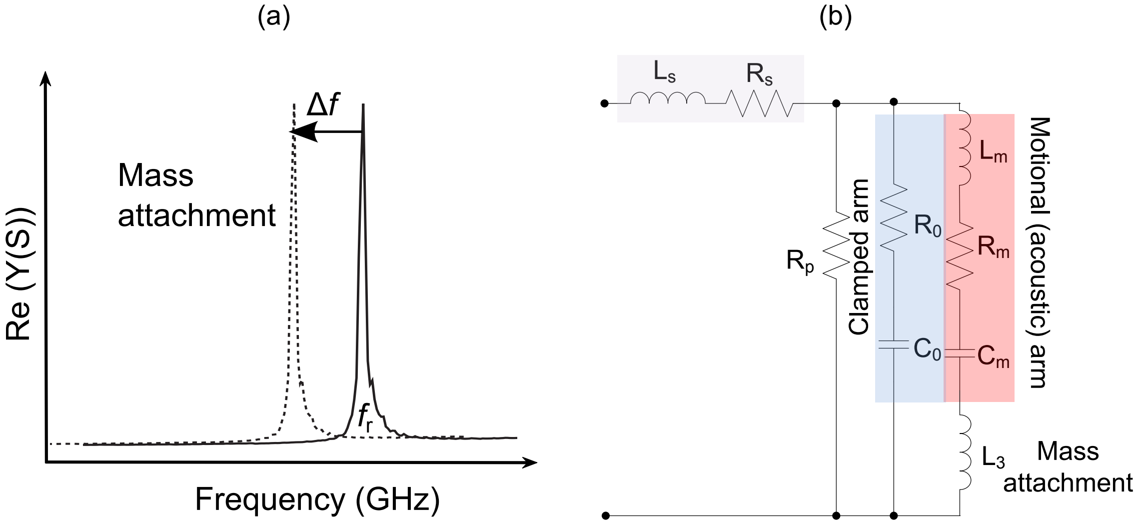

Figure 2.11: (a) shows the frequency shift observed in the real part of the admittance (Y), when mass is loaded on the resonator, the frequency decreases. (b) represents the modification of the mBVD model when mass attaches to the resonator, which is shown by the addition of an inductance in the motional arm.

2.8 Materials

In this section, the common materials used in BAW resonators are discussed and the requirements to achieve high Q value and k^2_{eff} are outlined. Silicon is the material of choice for the substrate because of its well-known fabrication process, abundance, integration and affordability. However it can absorb the acoustic waves generated by the FBARs and SMRs, therefore rendering acoustic insulation essential below the active area.[67] Resonators have also been fabricated on glass substrates for optically transparent devices [107] and arbitrary polymers such as polyimide for different flexible applications.[108]

2.8.1 Piezoelectric layer

In biosensing applications, a piezoelectric layer with a high acoustic coupling is required for efficient transduction of biorecognetion events. Low acoustic losses increase the energy confined in the resonator resulting in high Q.[109] High acoustic velocities ensure higher resonant frequencies for similar film thicknesses, which then translate into a higher mass sensitivity.[109] A summary of the important longitudinal mode electromechanical characteristics of common piezoelectric materials can be found in Table 2.1.

Table 2.1: Electromechanical properties of some common piezoelectric materials, data from [82, 102, 110–112]

Material	ρ (g/cm^3)	ϵ_{33}	v_L (m/s)	Z_a (MRayl)	k_t^2 (%)	Loss (dB/µs)
CdS	4.82	9.5	4465	21.5	2.56	> 50
ZnO	5.68	10.2	6330	36.0	8.38	8.3
AlN	3.27	10.2	10400	34.0	6.37	~ 5
$LiNbO_3$	4.64	29	7320	30.6	2.66	0.7
$LiTaO_3$	7.45	43	6160	46.4	3.25	0.8
PZT	7.60	> 80	4570	29.8	9.88	> 400

$LiNbO_3$ and $LiTaO_3$ have low acoustic losses and high acoustic velocities, but they are expensive and are not easily integrated in standard electronics because of their difficult deposition techniques.[34, 39, 110] Lead zirconate titanate (PZT) films are unsuitable because of their high piezoelectric attenuation, low acoustic velocities and poor biocompatibility.[39]

ZnO is an optically transparent II-VI semiconductor which is also referred to as a metal oxide. The crystal structure is found in three forms: wurtzite, zincblende or rocksalt. At room temperature and pressure, wurtzite is the most thermodynamically stable form of ZnO. In the most common wurtzite configuration, it has a hexagonal structure with $a = 3.25$ Å and $c = 5.21$ Å lattice spacing and c/a ratio of $\sim$1.60. The stacking pattern for the wurtzite structure is ABABABABAB with A representing the Zn atoms and B representing the O atoms. Each set of atoms forming a tetrahedral shape creating a polar stacking. Initially, ZnO was the material of choice but Lakin [113] reported AlN as a substitute in 1981. AlN is a III-V compound with a wurtzite crystal structure. The lattice constants are $a = 3.112$ Å, $c = 4.982$ Å. AlN has some outstanding physical properties that have attracted much interest: AlN has a wide band gap of 6.2eV. Its hardness (stiffness constants slightly inferior to those of diamond films) and low density of 3300 kg/m^3 leads to a high v_L of 11550 m/s.[114] However the stoichiometry of AlN films is more difficult to control.[39] Conversely ZnO has better acoustic coupling and can be deposited easily.[115] In addition, as described in [39], ZnO interacts with biological species safely, without contaminating samples. Still AlN is a strong material with a Young modulus similar to quartz, and it is also resistant to chemical attack at temperatures below 700 °C.[48] The acoustic velocity of ZnO has a larger temperature coefficient, TCF, of (-60 ppm/°C) compared to AlN (-25 ppm/°C), implying that a larger Δf_r is produced in ZnO for the same temperature change.[116] This can cause large and undesired Δf_r in ZnO biosensors operating in thermally unstable environments. Even so this property could be employed in temperature sensing in conjunction with other properties such as pressure and mass.[117, 118] Nonetheless for higher f_r and thus enhanced S_m, AlN is the primary choice.[29, 57, 119]

The electromechanical properties of ZnO and AlN are given in detail next as they will be used in future chapters. The elastic stiffness matrix for ZnO is:

$$\boldsymbol{c^E_{ZnO}} = \begin{bmatrix} 2.10 & 1.21 & 1.05 & 0 & 0 & 0 \\ 1.21 & 2.10 & 1.05 & 0 & 0 & 0 \\ 1.05 & 1.05 & 2.11 & 0 & 0 & 0 \\ 0 & 0 & 0 & 0.423 & 0 & 0 \\ 0 & 0 & 0 & 0 & 0.423 & 0 \\ 0 & 0 & 0 & 0 & 0 & 0.44 \end{bmatrix} \quad (10^{11}\,\mathrm{Pa})$$

the ZnO piezoelectric stress constant:

$$\boldsymbol{e_{ZnO}} = \begin{bmatrix} 0 & 0 & 0 & 0 & -0.48 & 0 \\ 0 & 0 & 0 & -0.48 & 0 & 0 \\ -0.57 & -0.57 & 1.32 & 0 & 0 & 0 \end{bmatrix} \quad (\mathrm{C/m^2})$$

while the clamped dielectric constant of ZnO is:

$$\boldsymbol{\epsilon^S_{ZnO}} = \begin{bmatrix} 7.6 & 0 & 0 \\ 0 & 7.6 & 0 \\ 0 & 0 & 9.0 \end{bmatrix} \quad (10^{-11}\ \mathrm{F/m})$$

In comparison the elastic stiffness matrix for AlN is:

$$\boldsymbol{c^E_{AlN}} = \begin{bmatrix} 3.45 & 1.25 & 1.20 & 0 & 0 & 0 \\ 1.25 & 3.45 & 1.20 & 0 & 0 & 0 \\ 1.20 & 1.20 & 3.95 & 0 & 0 & 0 \\ 0 & 0 & 0 & 1.18 & 0 & 0 \\ 0 & 0 & 0 & 0 & 1.18 & 0 \\ 0 & 0 & 0 & 0 & 0 & 1.10 \end{bmatrix} \quad (10^{11} \text{ Pa})$$

whereas its piezoelectric stress constant is given by:

$$\boldsymbol{e_{AlN}} = \begin{bmatrix} 0 & 0 & 0 & 0 & -0.48 & 0 \\ 0 & 0 & 0 & -0.48 & 0 & 0 \\ -0.58 & -0.58 & 1.55 & 0 & 0 & 0 \end{bmatrix} \quad (\text{C/m}^2)$$

and AlN has the following clamped dielectric constant:

$$\boldsymbol{\epsilon^S_{AlN}} = \begin{bmatrix} 8.0 & 0 & 0 \\ 0 & 8.0 & 0 \\ 0 & 0 & 9.5 \end{bmatrix} \quad (10^{-11} \text{ F/m})$$

The thicknesses of other layers in BAWs are in practice comparable to the piezoelectric film and loss mechanisms through such acoustically ‘dead’ layers should also be reduced for better electromechanical performance to achieve high S_m and improved LOD.[41] New designs and appropriate material choice are necessary to improve signal to noise ratio and eliminate spurious modes in FBARs and SMRs.[41, 120]

2.8.2 Electrodes

Electrical losses are caused by the resistance of the resonator electrodes and wires connecting resonators and bonding/probing pads. Low resistivity materials such as Au or Al in the electrodes with suitable thickness can reduce ohmic losses, but thicker electrodes reduce k^2_{eff}, which implies necessary trade-offs.[64, 71] Dielectric loss and eddy current losses are the other reported electrical loss paths.[116] Ideally the electrode should have a low mass density to minimise mass loading and a high acoustic impedance to confine energy within the piezoelectric film, thus suppressing spurious responses.[116, 121] Yokoyama *et al.* [116] estimated that the acoustic impedance of the electrode should be at least 1.5 times the acoustic impedance of the piezoelectric material. A graph illustrating the acoustic impedance of common electrode materials against their densities is shown in Figure 2.12. Accordingly the most suitable electrode materials would be in the top-left corner of the impedance against density graph.[66] Clement *et al.* [122] recently demonstrated Ir as an excellent electrode material for AlN BAWs because of its superior acoustic impedance, but at the expense of a high density that causes additional damping. Au has higher acoustic losses; yet it is a common electrode material since immobilisation of biological entities is more amenable on Au.[39, 65] Mo is another common electrode material owing to its high Z_a and low ρ, which implies that thicker Mo can be used without causing large mass loading effects.[64]

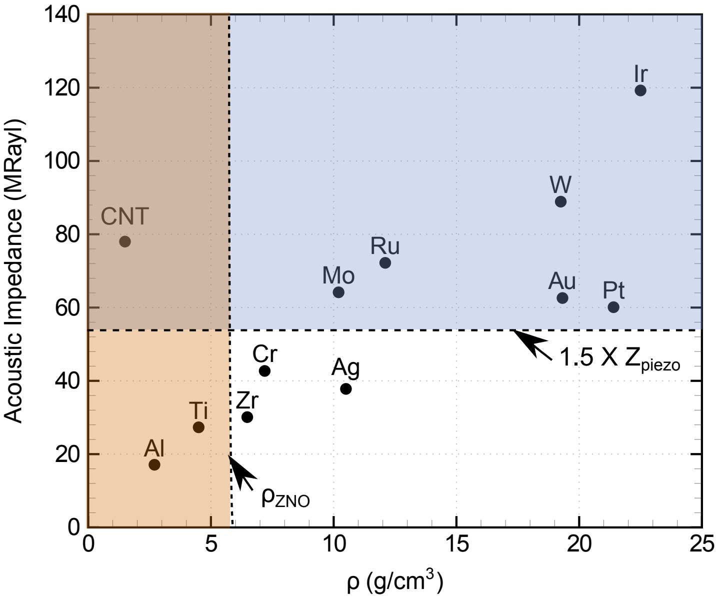

Figure 2.12: Acoustic impedance for different electrode materials as a function of their densities. Materials in the left hand corner (only CNTs) of the overlapping region meet the low density (Density of ZnO used as reference for the mass load) and high acoustic impedance requirements (1.5 × Z_{piezo}).

From Figure 2.12, carbon nanotubes (CNTs) have the desired properties as electrodes for BAW resonators. The low density of CNTs reduces mass loading on the resonator and their high acoustic impedance improves acoustic wave confinement within the piezoelectric layer.[66, 123, 124] In addition CNTs have a higher surface area to volume ratio, which increases the number of binding sites and hence the sensitivity.[13, 125] They are also easily functionalised with biological species to improve the sensor selectivity towards target molecules.[125–127] Eventually these characteristics are beneficial for biosensors because a single layer of interconnected CNTs could function simultaneously as the electrode and the biorecognition layer.[66, 121]

2.8.3 Acoustic reflectors

FBARs were recently shown to have better sensitivities than SMRs by García-Gancedo *et al.* [65] for identically designed devices. The main source of losses was ascribed to the Bragg reflector, which introduced additional loss mechanisms in SMRs.[57, 65] Designing the acoustic reflector layers with the best film quality is essential for confining the mechanical vibration in the piezoelectric cavity. Layers with excess stress and strain can cause improper reflection at the interfaces, thus the deposition of low-stress materials is necessary for best performance.[96, 128] The number of layers and materials should be appropriately chosen and deposition conditions should be tuned to obtain the optimum thicknesses and acoustic properties.[64, 69]

SiO_2 is a low acoustic impedance material used in the acoustic reflectors, due to its compatibility with silicon processing and its easy deposition.[129] The mirrors require a high acoustic mismatch at the interfaces, which is achieved with alternating layers of high and low acoustic impedance.[64] The total reflectivity of the mirror is determined by the number of layers and the materials utilised. High acoustic impedance materials such as W or Mo are normally chosen.[64, 69] Silicon oxy-carbide (SiOC) is also a low Z_a material but it has significant acoustic losses and does not adhere well on other materials.[130, 131] Both Si_3N_4 and SiO_2 have similar densities but the higher acoustic velocity of Si_3N_4 gives it a relatively higher Z_a.[64, 132] However the impedance mismatch is only 2.9. Comparatively a SiO_2/Mo interface impedance mismatch is 5 while a SiO_2/W interface has a corresponding mismatch of 8.5 leading to better confinement of the acoustic wave as shown in Figure 2.13.[69] Dielectric materials such as Ta_2O_5 and WO_3 have also been adopted in acoustic reflectors but they have lower acoustic impedances than metals.[89, 131, 133] A high acoustic mismatch reduces the number of layers required to reach the maximum reflection and a low acoustic velocity implies that a thinner layer is needed in the mirror fabrication.[64, 69] The simulated transmission using the transmission line model from section 2.6.1 in MATLAB, of the longitudinal and shear mode through 5 layered reflector made with different high acoustic impedance materials with a center frequency at 1.5 GHz are shown in Figure 2.13. Marksteiner *et al.* [129] also demonstrated that the shear reflection characteristics of the Bragg reflector can have profound effects on the Q value of a longitudinal mode resonator at antiresonance. A logarithmic transmission, T, of the form:

$$T = 10\log_{10}\left(1 - \left|\frac{Z_{mirror} - Z_{piezo}}{Z_{mirror} + Z_{piezo}}\right|^2\right) \tag{2.61}$$

can demonstrate the details of the reflection lobes in the reflector spectrum.

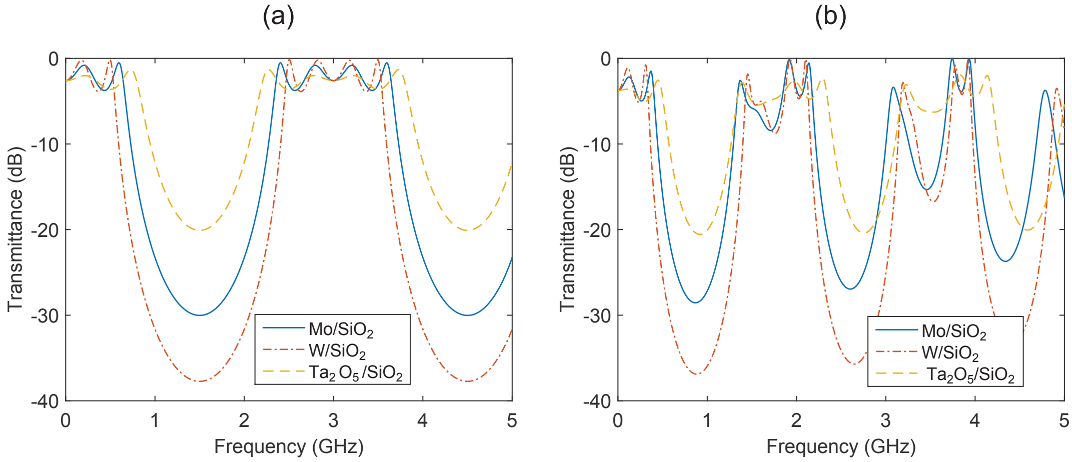

Figure 2.13: Acoustic wave transmission through the reflector made of 5 layers for longitudinal mode of 1.5 GHz in (a) and with the same thicknesses, the reflection spectra for the shear mode in (b) Different high acoustic impedance materials are compared, with W and Mo having lower transmission compared with dielectrics such as Ta_2O_5.

In addition the acoustic reflector can be designed to reduce the TCF of the resonators, which eliminates the active compensation techniques reported in [73, 134] that are costly, complex and require reference devices. Intrinsic or passive compensation can be achieved using layers with opposite temperature coefficients to eliminate thermal interferences.[118, 135] The unique TCF (+80 ∼ +100 ppm/°C) of SiO_2 can reduce the f_r sensitivity to temperature.[34, 72] Designing the reflector layers with the correct thickness and properties as described in [136, 137] can reduce the temperature sensitivities in order to detect only mass attachment.

2.9 In-liquid operation

BAW shear waves are associated with in-plane displacements which couple to the liquid through internal friction forces at the interface and which forces depend on the viscosity of the liquid. Assuming no-slip, the particles at the liquid-resonator interface move synchronously with the resonator surface and couples motion into the liquid. Since liquids do not support shear waves the amplitude of the motion decays rapidly with distance from the surface as shown in Figure 2.14.

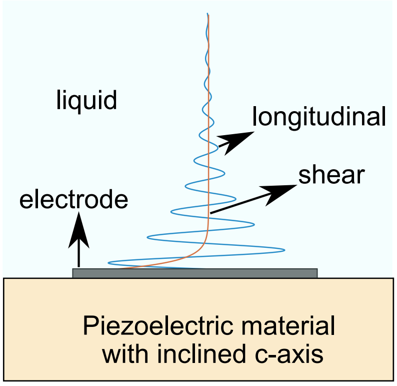

Figure 2.14: Propagation of shear and longitudinal mode from the piezoelectric layer into a liquid, the shear mode decays immediately in a short length, whereas the longitudinal mode propagates and the energy is lost in the liquid causing a higher damping compared to the shear mode.

The characteristic length or decay length (δ) depends on the angular frequency (ω), liquid viscosity (η_l) and density (ρ_l) as given by [74]:

$$\delta = \left(\frac{2\eta_l}{\omega\rho_l}\right)^{0.5} \tag{2.62}$$

The decay length in water at 5 MHz is 250 nm whereas at 1 GHz this value is one order magnitude less (∼20 nm), demonstrating the fundamental difference between QCM and FBAR operation in liquids. However, the shear frictional motion in the near surface region represents energy radiated into the liquid and causes a reduction in Q. The Δf_r when the piezoelectric material borders a liquid can be represented as an increase in motional inductance (L_l) while the acoustic loss due to energy dissipation can be seen as an increase in the motional resistance (R_l) in the equivalent circuit. This motional resistance leads to resonance damping and is ideally proportional to $(\eta_l \rho_l)^{0.5}$.[138, 139]

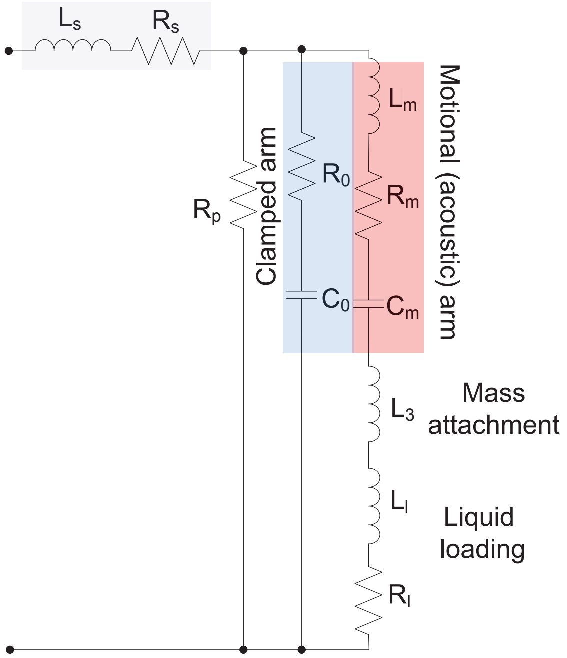

Figure 2.15: Addition of a resistance R_l to the mBVD model to represent acoustic attenuation in liquid, and an inductance, L_l to show the mass change that occurs depending on the viscosity and density of the liquid. The mass attachment inductor L_3 is still present to show the mass loading.

The Q_r of the resonator is therefore:

$$Q_r = \frac{\omega_L}{R} \approx \frac{2\pi f_r (L_m + L_l + L_3)}{R_m + R_l + R_s} \tag{2.63}$$

It is noted that this model assumes smooth surfaces and laminar flow while the coupling to the liquid is through viscosity only. In reality there can be additional factors that result in deviations from above calculations. Rough surfaces can cause non-laminar flow and also out-of-plane motions that will increase the motional elements and consequently reduce the Q.[48, 77, 140] The Δf_r with η_l is given by Kanazawa and Gordon [138] model, which leads to a viscosity sensitivity, S_v, of:

$$S_v = \frac{-f_r^{3/2}}{\Delta\eta}\sqrt{\frac{\rho_l\eta_l}{\pi\rho_p\mu_p}} \tag{2.64}$$

Several works have reported the use of BAW resonators for in-liquid biosensing. Weber *et al.* [141] first demonstrated shear mode SMR biosensor in liquid media. A ZnO thin-film with an inclined c-axis of 16° was fabricated to excite a quasi-shear mode at ∼800 MHz.[141] The sensitivity was reduced in the shear mode (S_m = 585 Hz cm^2/ng) compared to the longitudinal mode (S_m = 938 Hz cm^2/ng). However the minimum detectable in ng/cm^2 was improved from 21 to 2.3 in the shear mode operation. Similar to [141] Link *et al.* [105] fabricated a ZnO shear mode SMR with Q of 199 in liquid compared to 380 in air. Wingqvist *et al.* [48, 140] reported liquid sensing using a shear mode AlN FBAR with an inclination of around 30° and f_r of 1.2 GHz. In the liquid the shear mode Q was 150 compared to only 30 in the longitudinal mode.[140] Bjurström *et al.* [88] also reported that the same AlN FBAR shear mode Q was 350 in air. The resonance of the longitudinal mode in liquid was indiscernible.[140] Wingqvist [6] also demonstrated that an inclination of 50° between the electric field, E, and the c-axis produced the strongest shear mode. In the same review by Wingqvist [6], the minimum detectable mass using shear mode in liquid was shown to be in the range of 0.3 ng/cm^2 to 7.5 ng/cm^2. Hence it can be deduced that a pure shear mode is not ideal. A quasi-shear wave obtained with an inclination of approximately 50° is well-suited to liquid sensing, illustrated by Bjurström *et al.* [142]. Pure shear mode FBARs were succesfully fabricated using $(11\bar{2}0)$ textured ZnO by Yanagitani *et al.* [53] but this method requires significant modification to the deposition chamber. The most effective method to excite the TSM has been achieved by the deposition of seed layers with controlled roughness and orientation in conjuction with an off-axis deposition to promote the growth of inclined c-axis piezoelectric films.[50, 88, 143]

Zhang and Kim [78] demonstrated liquid sensing with the second harmonic of longitudinal mode of a ZnO FBAR. It was shown that the Q at $f_{r,0}$ decreased from 210 in air to 12 in water (by 94%). The Q of the second harmonic was reduced from 340 to 40 in water (by 88%). Although the work by Zhang and Kim [78] explained that there is a smaller acoustic loss in liquid when sensing with higher order harmonics, a Q of 40 is still not adequate for sensing low quantities of biomolecules in liquids. Additionally the second harmonic will likely produce a lower mass sensitivity, with $n = 2$ in by equation (2.57), than a device with a corresponding high $f_{r,0}$. Besides the LOD of $10\,\mathrm{ng/cm^2}$ achieved by the second harmonic resonance reported by Zhang and Kim [78] is one order of magnitude worse than the corresponding value for QCMs, which is $1\,\mathrm{ng/cm^2}$.[13, 42, 43]

Longitudinal modes with high Q in liquids were shown by Pottigari and Kwon [144] with a design incorporating a parylene layer on top of the resonator. A vacuum gap was created between the resonator surface and the parylene layer to eliminate acoustic energy leakage in the liquid.[144] In air, a Q of 153 was measured and it decreased by only 9% to 140 in liquid.[144] A conventional FBAR would have suffered a Q reduction of more than 85%.[47, 52] Parylene is a polymer that can operate at high temperatures and it is also biocompatible.[145] Additional work needs to be carried out on vacuum-gap FBARs devised by Pottigari and Kwon [144] to confirm their viability for sensing actual biological specimens in liquid with high sensitivities. Xu *et al.* [94] reported high S_m and relatively better Q in a microfluidic integrated FBAR for direct liquid sensing with the longitudinal mode. At $f_r = 2\,\mathrm{GHz}$, S_m of $1000\,\mathrm{Hz\,cm^2/ng}$ (3 times greater than the shear mode) and a LOD of $1.35\,\mathrm{ng/cm^2}$ were extracted.[94] According to Xu *et al.* [94], the thickness of microfluidic channel should be a multiple of half the acoustic wavelength in water to maximise acoustic reflection at the interface. However imprecise liquid thickness can lead to exponential acoustic leakage, making this technique difficult to implement in practice.[94]

Despite the lower damping of the TSM in liquids, the acoustic leakage through more viscous liquids is large, which damps the TS resonance substantially.[139] Also the use of the shear resonance limits S_m to be only one-third that of a longitudinal mode BAW resonator with similar dimensions.[94, 141] Moreover the scalability of fabricating inclined c-axis films is limited compared to c-axis oriented films for the longitudinal modes, which remains the desired mode of operation for in-liquid sensing. An interface layer that can provide an acoustic mismatch between the resonator and the liquid to confine the wave and with low mass density can reduce this damping significantly, in order to achieve a Q value sufficient for biological detections.

2.10 Carbon nanotubes integration

Owing to their extraordinary electronic and mechanical properties, CNTs have great potential to find applications ranging from molecular electronics to ultrasensitive biosensors. Their biological compatibility provides them with specific chemical handles that would make several of these applications possible. Besides the larger surface area to volume ratio of CNTs makes them an attractive alternative to metallic electrodes for improving the S_m and the LOD of BAW resonators. Indeed the surface area of a thin film of interconnecting CNTs is significantly greater than the surface area of a metal thin film electrode; hence the binding area is increased without physically increasing the size of the devices.[66, 121] Consequently, for the same concentration of biological samples, a larger number of targeted molecules can be bound onto the resonator surface compared to devices with metal electrodes; devices with higher S_m can therefore be realised. In addition CNTs have lower ρ (1.3 g/cm^3) compared to metals, which reduce mass loading and their high Z_a (comparable to Mo) ensures maximum confinement of the acoustic wave in the piezoelectric material.[127] CNTs offer an additional benefit compared to metals in that it is possible to functionalise CNTs for direct covalent bonding to molecules, or with different types of polymers which could be used for non-covalent bindings, thereby preventing non-specific binding or the need for additional bonding layers.[146] Ultimately, CNTs have the simplest chemical composition and atomic bonding configuration, being entirely composed of carbon atoms, which provide a natural match to organic molecules.

Previous works on CNTs by Dragoman *et al.* [147] demonstrated a 10 times improvement in the longitudinal mode Q in air due to enhanced acoustic confinement in the resonator by CNT electrodes. Penza *et al.* [148] functionalised single-wall CNTs (SWCNTs) using the Langmuir-Blodgett technique before performing multiplexed detection on vapours of acetone, ethylacetate and toluene.

High sensitivities were obtained in all cases: acetone (12 kHz/ppm) and ethylacetate (17.3 kHz/ppm).[148] The minimum detected concentrations were well below their threshold limit values.[148] The sensitivity of an AlN FBAR with CNT top electrode fabricated by García-Gancedo *et al.* [66] was 0.25 MHz cm^2/ng compared to 0.14 MHz cm^2/ng using Au/Cr electrodes. It was the highest S_m reported to date in dry measurement with the ability to low quantities of materials.[66, 117] Hence, the potential exists to use chemically-modified CNTs for in-liquid sensing with the longitudinal mode which would function both as the electrode and as the sensing layer. To fulfill this simultaneous use, CNT forests have to be grown directly and surface-bonded to the piezoelectric film of the resonators.[61] However electrodes made purely of CNTs introduce parasitics in the BAW resonator, which deteriorate the Q_r in air.[149] Indeed it was shown by Iborra *et al.* [150] that the high electrical resistance and the surface roughness of the CNTs are detrimental to the resonator response if grown directly on the piezoelectric material. Consequently CNTs can be grown on metallic electrodes in the active area to function solely as the sensing layer rather than an electrode.

2.11 Research objectives

This chapter described the piezoelectric effect and the operation of BAW resonators both with an oriented *c*-axis and an inclined *c*-axis. In this thesis the following works will be carried out to address the limitations of achieving high frequency BAW resonator for biosensing applications on a large scale:

- Growth and characterisation of inclined *c*-axis BAW resonators using seed layers and textured electrodes. The objective is to find controllable methods to grow *c*-axis piezoelectric films for large scale applications of shear mode resonators;
- CNTs with different morphologies as sensing layer for the shear mode resonators. In addition the interaction of CNTs in liquids and their viability as an interface layer providing an acoustic mismatch, thus minimising longitudinal mode damping in liquid, will be assessed.

Chapter 3

Thickness shear mode resonators

In this chapter, the methods used to achieve the shear mode resonance in ZnO SMRs are discussed. The chapter begins with a description of the process used to grow ZnO and the optimum conditions to deposit inclined c-axis ZnO. Generally polycrystalline ZnO with good piezoelectricity are obtained when all the microcrystals are parallel to a given direction and exhibit same crystal polarity.[151] This is achieved during sputtering under certain conditions that favour the preferential growth of the (0002) planes parallel to a given direction, as the (0002) orientation is more thermodynamically stable and such wurtzite structures are polarised along the c-axis.[152] Usually the c-axis of the grown film is normal to the substrate surface, which is the desired orientation for TLM operation. The nature, roughness and crystallographic orientation of the surface are all essential parameters for controlling the c-axis orientation of the piezoelectric films.[153] In order to effectively excite the shear mode, this polarisation axis of the film should have a inclination angle from 20° to 50° as shown in the chapter 2.[48]

Piezoelectric films with inclined c-axis can be sputtered on a surface with controlled roughness immediately below the active layer as depicted in Figure 3.1.[53, 141] If the flux of atoms impinging on the exposed facets is constant, the grains of the piezoelectric material will grow in different directions, leading to a randomly-oriented layer with poor piezoelectric characteristics. However, if the substrate is displaced from the center of the target as shown in Figure 3.1, an impinging direction is favoured. Therefore the grains will grow faster on the facets that are most exposed to the atom flux and their inclination angle will be more uniform as illustrated in Figure 3.1 (b).[50] A sawtooth surface profile is the best possible structure to achieve homogeneously inclined grains; yet such topography is difficult to fabricate. Instead, a layer with a textured surface is commonly used to grow piezoelectric films with inclined c-axis.[50, 88] The aim of this chapter is to achieve homogeneously inclined c-axis ZnO for SMRs with high shear mode Q_r and k^2_{eff} to be used in liquid for biological detection. Surfaces with different roughnesses and properties are compared: the inherited random roughness of an acoustic reflector, the controlled roughness of a seed layer and finally a textured bottom electrode with controlled roughness.

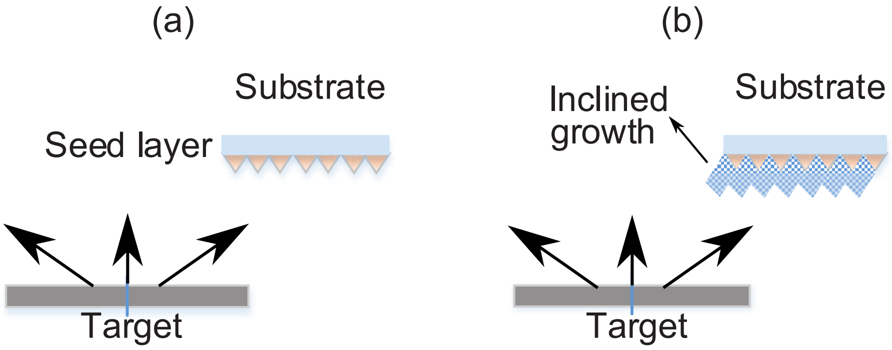

Figure 3.1: (a) Off-axis between the sputtering target and a substrate having a seed layer that will promote the growth of a forthcoming piezoelectric film. (b) Growth of the inclined c-axis ZnO favoured by the presence of seed layers of a certain orientation and the off-axis deposition to get the desired inclinations. Growth of this inclination is dictated by the initial seed layer.

3.1 Polycrystalline AlN seed layer and inherited reflector roughness

In this section, AlN seed layers with mainly (103) orientation are considered as the first seed layer in this work as this has already been shown to achieve inclined c-axis AlN with an inclination angle of ∼25°.[50] To compare the effect of the homogeneous polycrystalline seed layer, a random roughness generated by the sputtering of an acoustic reflector stack is also used.

3.1.1 SMR fabrication process

The devices fabricated in both cases are schematically represented in Figure 3.2. First five layers alternating between porous SiO_2[154] and Mo are deposited by Dr. Mario DeMiguel-Ramos in Spain on (1 0 0)-oriented Si substrates to form the acoustic mirror. The five reflector layers (three of SiO_2 and two of Mo) are sputtered in a pulsed (pulsing at 250 kHz) DC Leybold Z550 system with 150 mm diameter targets of Si and Mo in Ar/O_2 mixtures and in pure Ar respectively. Table 3.1 provides the conditions used for the sputtering. The thicknesses (521 nm for SiO_2 and 629 nm for Mo) are designed so that the reflectors have a reflection bandwidth for the shear mode centered at 1.2 GHz in frequency. One set of reflector is mechanically polished using alumina slurry to reduce the root mean square (rms) surface roughness of the top SiO_2 layer from around 20 nm to less than 1 nm.

Table 3.1: Sputtering conditions of porous SiO_2 and Mo.

Parameters	SiO_2	Mo
Ar (sccm)	44.1	18.1
O_2 (sccm)	16.5	0
Pressure (Pa)	1.2	0.2
Power (W)	1200	400

After sputtering 120 nm of Mo as the bottom electrode using the DC Leybold Z550 system, the AlN seed (∼150 nm) is deposited on the polished samples in an ultra-high vacuum sputtering system pumped down to a base pressure of 1.3×10^{-6} Pa to avoid contamination with O_2. A 150 mm diameter 99.999% purity Al target located at a distance of 55 mm from the substrate holder is used. The sputtering process is performed at a pressure of 0.67 Pa with a 60% N_2 in Ar admixture and a pulsed (pulsing frequency of 250 kHz) DC power of 600 W without any intentional heating of the substrate; these conditions promote the growth of (103) oriented AlN microcrystals as shown in [155, 156]. A high target utilisation sputtering (HiTUS, S500, PlasmaQuest Ltd, Hook, UK) system [157] is then used to reactively sputter the piezoelectric ZnO layer (∼0.8-1.0 µm thick) from a 100 mm diameter 99.999% Zn target in a 60% O_2 in Ar gas admixture, at a total pressure of 0.24 Pa. A power of 1000 W from a 13.56 MHz COMDEL RF supply generated the remote plasma and the Zn target is biased with a DC power of 800 W producing a DC

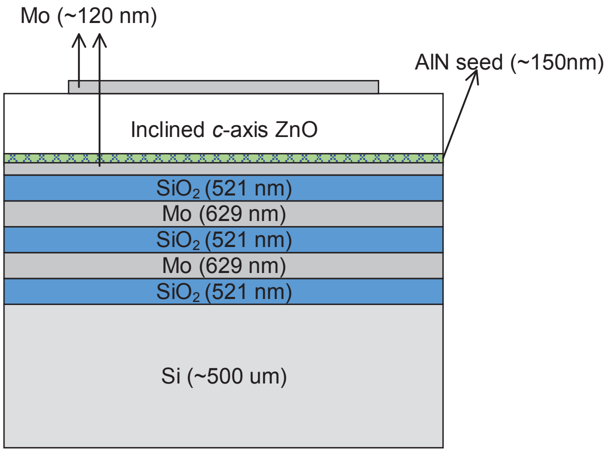

Figure 3.2: SMR with AlN seed layer at the interface between the bottom Mo electrode and the ZnO layer. The SMR devices have 5 layers in the acoustic reflector using porous SiO_2 and Mo with thicknesses of 521 nm and 629 nm respectively and achieving a reflector center frequency of 2.2 GHz in the longitudinal mode.

voltage of ~670 V during the deposition. The chamber is first pumped down to a base pressure of 2×10^{-4} Pa and the target is cleaned for 7 mins in Ar (gas flow rate: 25 sccm), before O_2 (gas flow rate: 37 sccm) is introduced and stabilised for another 7 mins. Off-axis deposition of the piezoelectric ZnO is achieved by reducing the distance separating the substrate holder and the target to 50 mm as shown in Figure 3.3 (a) and (b).

A lower substrate holder is made to move the substrate at a vertical distance of 5 cm from the target in the HiTUS (Figure 3.3 (b)). With this method, the substrate can be kept horizontal for off-axis deposition, whereas at longer distances, the substrate has to be held vertically to obtain the inclined *c*-axis growth, a method that is not scalable. In addition the ZnO film is sputtered at a low pressure of 0.25 Pa to increase the directionality of the atom flux; the thickness variation on a Si sample is evident from Figure 3.3 (c). Thickness measurement is carried out using a Dektak V2 stylus profilometer with 10 mg force. The sputtering conditions provided a sputtering rate of approximately 40-60 nm/min at the edge of the substrate holder as illustrated by the graph in Figure 3.3 (e). The chosen range of sample placement is selected as a trade-off for the sputtering rate, axis offset and plasma glow effect

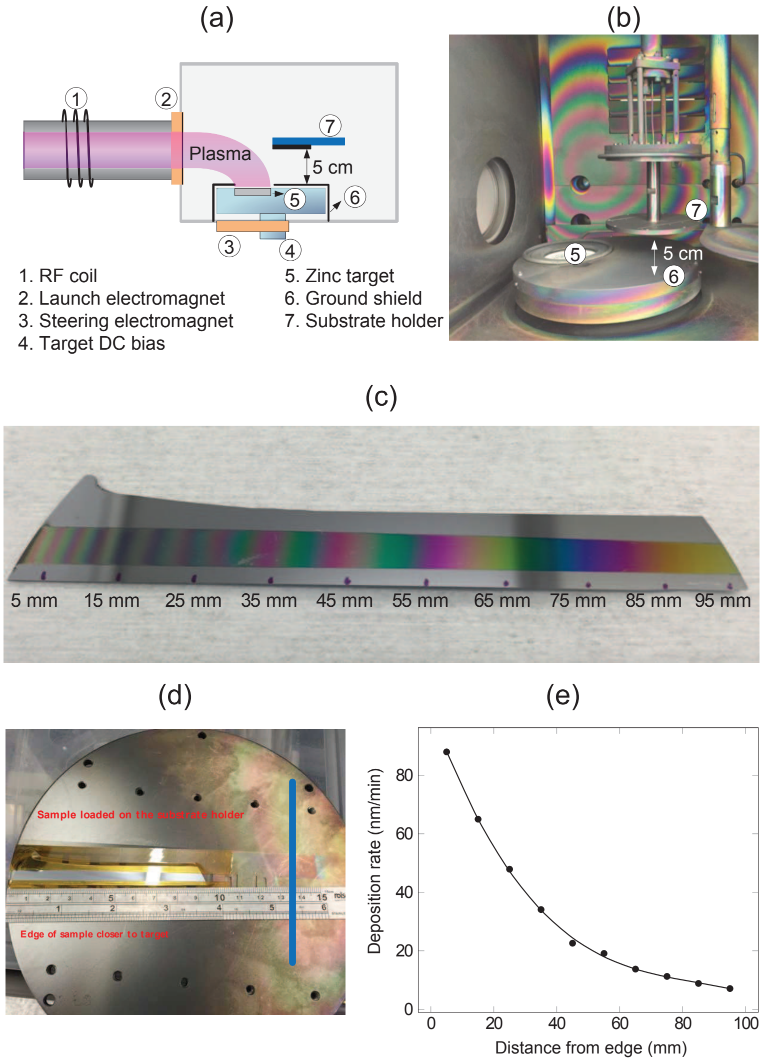

Figure 3.3: (a) The generation of the plasma and bias applied to the target in the HiTUS system and the position of the substrate relative to the target for off-axis deposition (b) Holder fabricated as an addition to the existing susbtrate holder to reduce the substrate to target distance to 50 mm and create a large offset (c) ZnO sputtered off-axis from the target along the substrate, showing rapid colour variations initially and a more gradual change towards the end of the sample. (d) The position of the sample on the substrate holder for the deposition rate calibration showing that the thickness variation also decreases further away from the target thus increasing the uniformity of the film. (e) Deposition rate of inclined ZnO along the substrate holder width confirming the rapid decrease close to the target which becomes more uniform towards the edge.

on the samples. Indeed having the samples too close to the edge caused the samples to be inside the plasma glow and subsequently the samples are highly stressed due to heat and Ar bombardment. A horizontal distance from the edge of the sample holder ranging from 10 mm to 30 mm from the is found to be the optimum. Mo (~120 nm) is then deposited as the top electrode using a 99.95% Mo target at a power of 100 W and pressure of 0.30 Pa in a White Magic DC magnetron sputtering system. Finally, the top electrode is defined using standard photolithography with Microposit S1818 photoresist followed by a dry etch process (Phillips reactive ion etching (RIE)) system with a CF_4/O_2 plasma using 100 W forward power and 20% O_2 (10 sccm of O_2 in 40 sccm of CF_4) at a total pressure of 20 Pa. Devices are also fabricated on Bragg reflectors designed for another frequency (0.9 GHz shear) to assess the effect of film thickness on the shear mode resonance. It is also determined that the AlN seed has to be above the bottom electrode because when the AlN seed is below the electrode, a highly stressed ZnO film is obtained after off-axis deposition, which peeled off in the photolithography stage when defining the top electrode.

3.1.2 Characterisation of AlN seed layers and ZnO films

The exposed facets of the AlN seed layers are observed by scanning electron microscopy (SEM, Carl Zeiss, Cambridge UK) (Figure 3.4 (a)) using an acceleration voltage of 3 kV. The surface of an unpolished reflector (Figure 3.4 (b)) demonstrates larger grains (~100 nm) compared to the AlN seed layers, which have grains of approximately 50 nm and a clear faceting. A cross-sectional cut of a device on the AlN seed layer is shown in Figure 3.4 (c) and on a rough reflector is shown in Figure 3.4 (d). These reveal an inclination of approximately 40° in the ZnO grains.

The X-ray diffraction (XRD) polar measurements around the (0002) axis of the ZnO (Figure 3.5) confirm that the film on the AlN seed layer (Figure 3.5 (a)) have a *c*-axis inclination of ~45° and a narrower inclination distribution compared to those deposited on the rough surface (Figure 3.5 (b)), which have a mean inclination of only ~25° and a greater dispersion because of the more dispersed and less homogeneous local surface microscopic planes. Conversely the substrates with AlN seed layers mainly have a (103) orientation showing uniformly distributed facets of

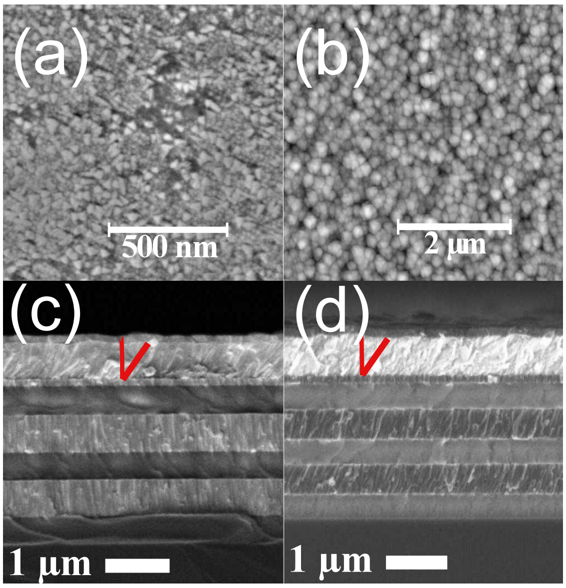

Figure 3.4: SEM micrographs of surface and cross section of the devices. (a): The AlN seed layer with exposed (103) facets that promote the growth of the inclined ZnO, (b): the surface of the unpolished reflector with large grains (∼100 nm). (c): An inclined 800 nm ZnO sputtered on AlN and, (d):an inclined 800 nm ZnO sputtered on rough surface. The Mo and SiO_2 layers from the reflector stack are also observed in (a) and (d).

the basal plane inclined ∼60° from the substrate surface as explained by DeMiguel-Ramos *et al.* [50]. These promote the growth of a more uniformly inclined layer.[50] ZnO films grown on surfaces with controlled roughness therefore have high *c*-axis inclination angles without requiring significant and complex modifications to the deposition system outlined in other similar work.[53, 105]

3.1.3 Electro-acoustic characterisation

A vector network analyser (ENA series, E5062A Agilent Technologies, Palo Alto, CA, USA) is used to characterise devices in the frequency range from 0.5 GHz to 3.0 GHz in this chapter. This network analyser is connected to ground-signal-ground (GSG) RF probes (Picoprobes, from GGB industries, Naples, FL, USA) with 150 µm pitch, which are fitted to micropositioners on a coplanar probe station. The electrical input impedance, Z_{in}, spectra measured for representative devices of each set of resonator are shown in Figure 3.6. In total ten devices are characterised in each case and the devices showing the best responses are analysed.

The SMRs exhibit appreciable shear and longitudinal modes but the frequencies are higher than the predicted value of 1.2 GHz for the TSM, because of thickness variation caused by the off-axis deposition. An estimate for the ratio of the longitudinal resonant frequency, f_L, to the shear mode resonant frequency, f_S, is calculated from v_S, and v_L using equation (2.21) and equation (2.22). At an inclination angle of 25° for the rough reflector, the calculated ratio (f_L/f_S) of ZnO is 2.06, whereas at 45° for the AlN seed, this ratio is 1.95. These are close to the experimental frequency ratios of 2.10 ($f_S = 1.35 \pm 0.02$ GHz, $f_L = 2.67 \pm 0.03$ GHz) for the rough surface and 1.98 ($f_S = 1.36 \pm 0.04$ GHz, $f_L = 2.87 \pm 0.02$ GHz) for the AlN seed. Devices fabricated on rough substrates had longitudinal modes with k^2_{eff} of only 0.95%. For comparison, values of k^2_{eff} for the longitudinal mode of resonators fabricated with the same conditions on polished substrates located along the axis of the target (pure *c*-axis oriented films) are around 5.4% at 2.5 GHz. Therefore with the inclined grains the electrical energy couples less efficiently into the longitudinal mode and more into the shear resonance. The electromechanical performances outlined in Table 3.2 demonstrate that devices with ZnO grown on AlN seed layers had higher k^2_{eff} (∼2.2% at 1.35 GHz) compared to the rough substrates (∼1.3% at 1.36

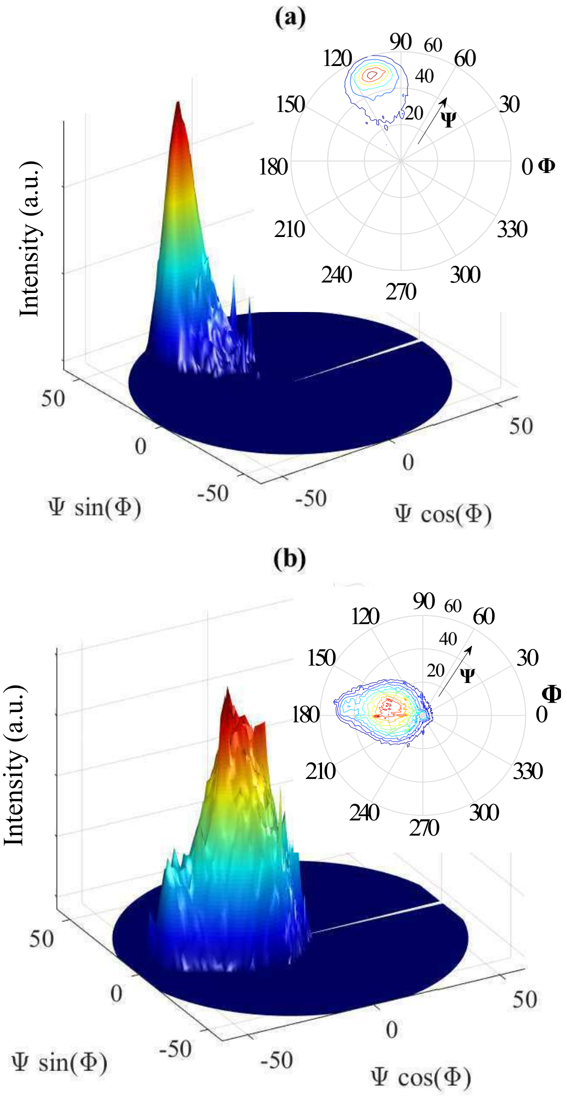

Figure 3.5: Polar measurements of the angles in 3D representation and plain view for ZnO films deposited on (a) AlN seed with ∼45° inclination and narrower dispersion and (b) rough substrate with a 25° inclination and broader dispersion.

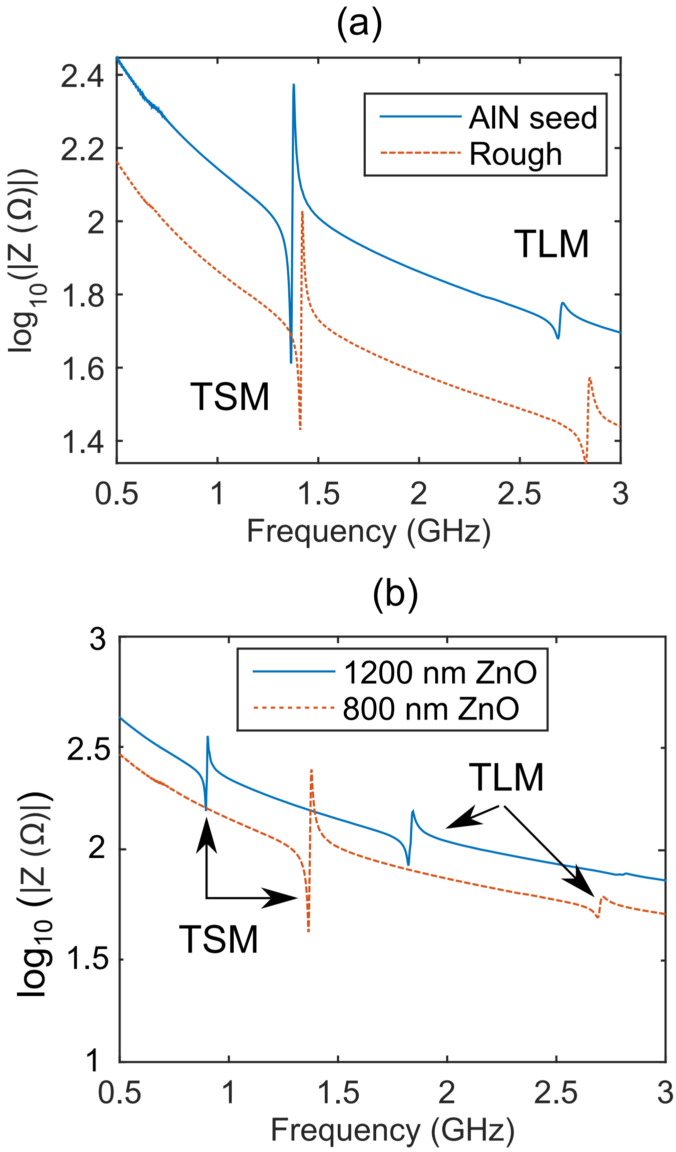

Figure 3.6: (a) Frequency response of the typical devices measured, the blue solid line represents the device with AlN seed layer and the dashed red line shows the response of SMR with the rough reflector. Both set of devices demonstrate the shear mode (TSM) and longitudinal mode (TLM) mode, but devices on the rough reflector had a more pronounced longitudinal resonance. A comparison of the different thicknesses of the ZnO on the shear mode and longitudinal mode is shown in (b).

GHz). Growing ZnO on a layer of AlN with controlled orientation improves the homogeneity of the inclination angles in the ZnO, which explains the higher k^2_{eff} of the shear mode in these SMRs. However the random roughness of the acoustic reflector surface leads to a larger range of inclination orientations as observed in the polar patterns (Figure 3.5 (b)), which deteriorate the electromechanical performance of the resonator. The shear mode Q_r is low (80-140) compared to similar work with inclined c-axis ZnO without a seed layer.[105] A lower Q_r is equivalent to a broader resonance peak, which reduces the number of frequencies that can be resolved and hence limits m_r. However, the Q_r can be improved by using an electrode with a controlled roughness as will be described in section 3.2. This would eliminate the interfacial and scattering losses caused by either the random roughness of the acoustic mirror or the piezoelectrically 'dead' AlN seed layer. Furthermore thicker ZnO layers lose the homogeneous inclination as the grains re-start to orient parallel to the c-axis as this is the more stable state thermodynamically. Eventually depositing thicker ZnO leads to more pronounced longitudinal modes as observed in Figure 3.6 (b). Therefore 800-1000 nm thick ZnO layers are ideal for obtaining a strong shear modes for in-liquid operation in the GHz regime.

Table 3.2: Shear mode performance of typical devices measured for the AlN seed layer and rough reflector layer

Substrates	f_S (GHz)	Q_r	Q_a	k^2_{eff} (%)
AlN seed	1.350	139	116	2.22
Rough	1.364	115	102	1.35

The electro-acoustic spectra are then analysed and the key parameters for the mBVD model outlined in section 2.6.2 are extracted by means of a MATLAB® software (details in Chapter 5). Table 3.3 lists these parameters which will be compared in section 3.2.

3.1.4 In-liquid performance

The effects of liquids with different products of viscosities (η) and densities (ρ) on the shear mode of a device with an AlN seed layer resonating at 1.35 GHz are shown in Figure 3.7. The shear mode Q_r decreases from 139 to 76 (by 45%) in acetone ($\rho =$

Table 3.3: MBVD model parameters extracted for the inclined *c*-axis ZnO grown on AlN seed layer and rough reflector.

Surface	C_0 (pF)	C_m (pF)	L_m (µH)	R_m (Ω)	R_0 (Ω)	R_s (Ω)
AlN seed layer	1.385	0.025	1.080	63.78	9.23	3.95
Rough reflector	1.363	0.021	0.802	75.79	4.93	2.46

0.79 g/cm^3, $\eta = 0.3$ mPa·s). In contrast, longitudinal mode Q_r (shown in Figure 5) is reduced by 87% in contact with acetone, thus rendering it unsuitable for in-liquid sensing. The shear mode Q_r decreased by 72% in water ($\rho = 1.00$ g/cm^3, $\eta = 1.0$ mPa·s) and by 92% in AZ5214E photoresist ($\rho = 1.00$ g/cm^3, $\eta = 22$ mPa·s).[158] As a comparison human blood typically have values of $\rho = 1.06$ g/cm^3 and $\eta \approx$ 2.0-3.0 mPa·s.[159, 160]

This Q_r decreases because the shear modulus of the liquid is non-negligible when its viscosity increases and acoustic energy leaks into the liquid. Furthermore the shear mode f_r decreases linearly with the product of $(\eta\rho)^{0.5}$ as shown in Figure 3.8 and predicted by Kanazawa and Gordon [138] model for the shear mode. The sensitivity of f_r to $(\eta\rho)^{0.5}$ is calculated to be -340 ppm/$\{(\mathrm{g/cm^3})\cdot\mathrm{mPa\cdot s}\}^{0.5}$

Nonetheless the number of liquid measurements is limited to 9 trials on average because of microcracking of the ZnO layer due to its porous nature and sensitivity to liquids, but this is acceptable for disposable sensors to which this technology is most suited. Therefore capping with SiO_2 or Si_3N_4 outside the active area could solve this problem. It has been shown in this section that by using a surface with controlled roughness and an off-axis deposition, polycrystalline ZnO films with a controlled and uniform inclined *c*-axis are grown at room temperature, which is promising for process compatibility and plastic substrates. However the AlN seed layers are electrically insulating and piezoelectrically inactive, which consequently reduce the capacitive coupling and the electric field, hence lowering Q_r and k^2_{eff}. The devices fabricated using AlN seed layers had Q_r of up to 140 in air, which decreased to less than 70 in liquids. A low Q_r increases the upper limit on the minimum resolvable frequency shift, Δf_{min}, and hence m_r, that can be detected is therefore large. Increasing Q_r is essential to track smaller mass attachment and improve the LOD.

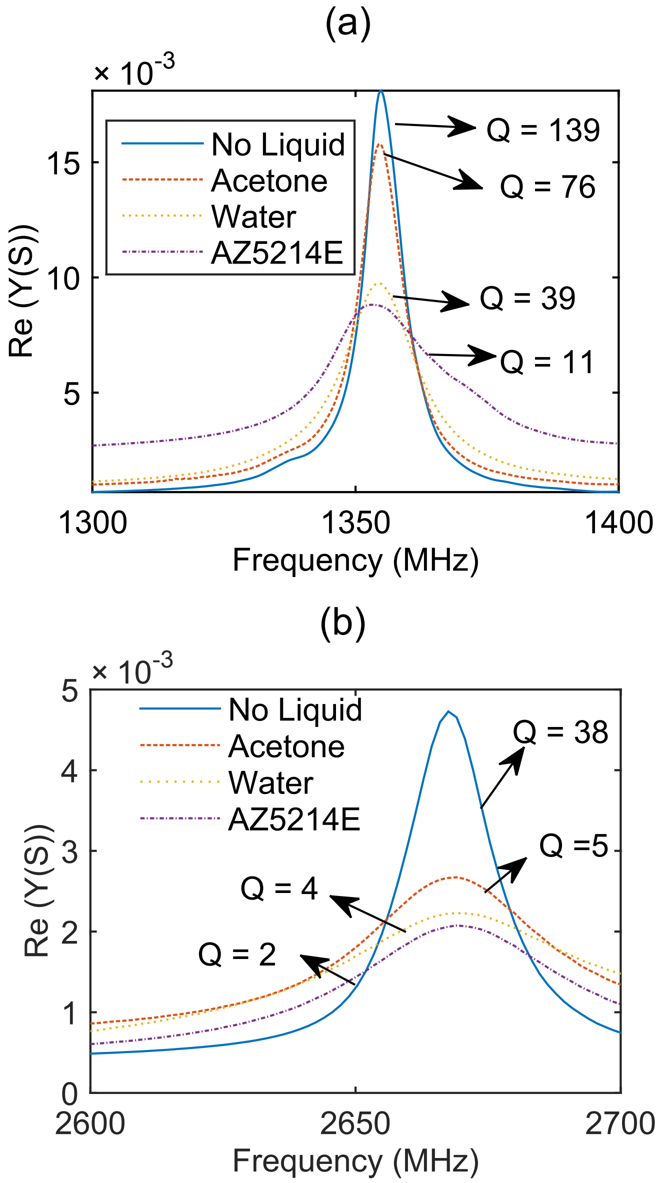

Figure 3.7: Effect of liquids of different viscosities and densities on the shear resonance electrical admittance, $Y(S)$ (a) (of a device with AlN seed layer with shear mode at 1.35 GHz) demonstrating that when viscosity increases (acetone to AZ5214E photoresist), the Q_r decreases due to damping (b) the longitudinal mode resonance has much higher damping in all liquids.

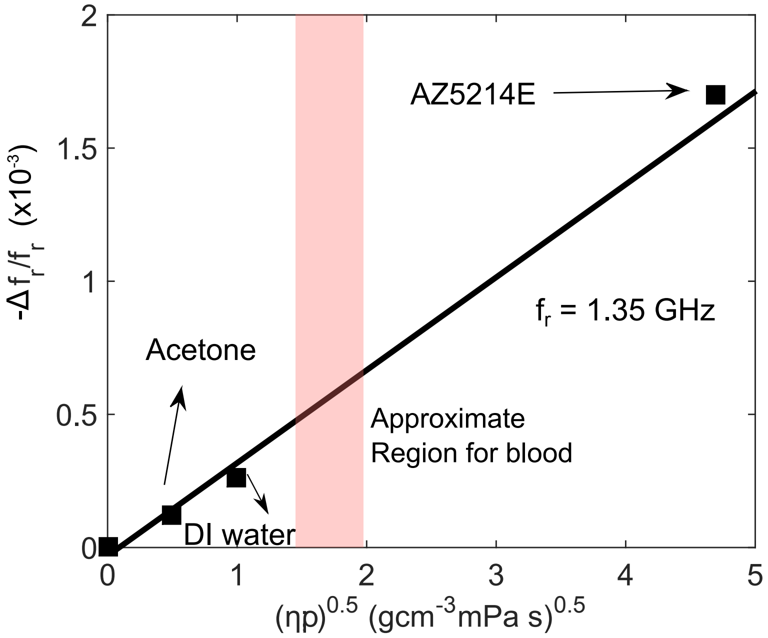

Figure 3.8: Shear mode frequency shifts observed with the variation of the $(\eta\rho)^{0.5}$ product, with the approximate region for blood shaded in red. The shear mode f_r decreases linearly with $(\eta\rho)^{0.5}$ as predicted by the Kanazawa model. The line is only for a guide to the eye.

3.2 Textured Al electrodes

From section 3.1, it is deduced that an electrically conductive surface with a controlled roughness promoting the growth of inclined *c*-axis ZnO is necessary to reduce the parasitic losses between ZnO and the bottom electrode, which were undesired features of the insulating AlN seed layer. Earlier works have shown that the morphology of sputtered metals such as Al can be controlled by the substrate temperature, T_S during deposition.[161, 162] At higher temperatures, more energy is supplied to the deposition atoms resulting in a higher migration mobility, which in turn favours the crystallisation of the film.[163] Indeed, with higher energy, the sputtered particles form nucleation islands that coalesce in crystals, hence promoting the formation of oriented grains and crystalline materials.[164] By varying T_S the adatom mobility on the surface and the resulting film morphology can be tuned to achieve a surface with optimum roughness necessary for growing inclined *c*-axis piezoelectric films. The potential of using Al as a textured surface to favour the growth of inclined *c*-axis ZnO and operating as an electrode simultaneously for shear mode resonators is attempted in this section. The objective is to eliminate a parasitic seed layer to improve the electromechanical performance of shear mode SMRs. Al electrodes sputtered at different T_S are compared by fabricating SMRs with inclined *c*-axis ZnO to determine the suitability of this method.

3.2.1 Device fabrication

The SMRs shown in Figure 3.9 are fabricated by first depositing a five layer acoustic reflector stack designed for 1.2 GHz shear mode. This is composed of alternating layers of porous SiO_2 and Mo, sputtered using the conditions outlined in section 3.1.1. The final layer is again mechanically polished by alumina slurry to reduce the roughness inherited from the sputtering process.

Al films (~180 nm) are deposited off-axis from the target in the HiTUS system.[157] A power of 1100 W from a 13.56 MHz RF supply generated the remote plasma in a 0.25 Pa Ar atmosphere and the Al target (99.999% purity) is biased with a DC power of 900 W, giving a DC voltage of 590 V during the deposition, and a sputtering rate of ~16 nm/min. The Al deposition process is performed at four different substrate temperatures, T_S: room temperature (RT) (25 °C), 100 °C, 200

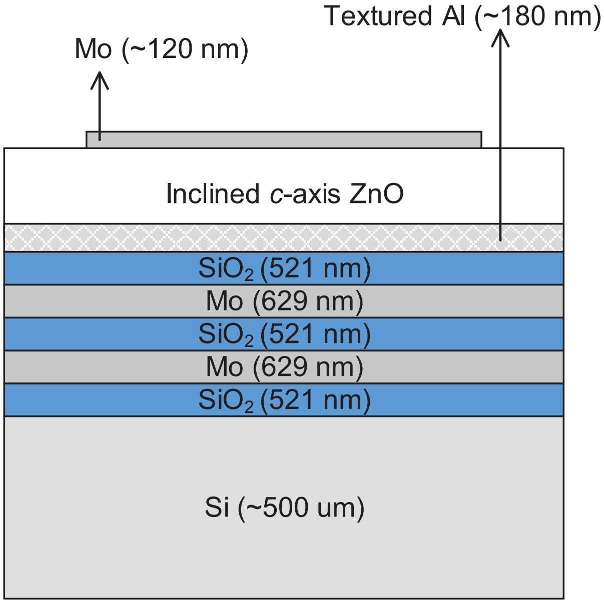

Figure 3.9: SMR with textured Al as bottom electrode for growing inclined c-axis ZnO, the reflector layers are designed for 2.5 GHz operation, the difference is the absence of the parasitic AlN seed layer.

°C and 300 °C. This upper limit on T_{S} is due to the equipment safety and therefore higher T_{S} are not tested. Inclined c-axis ZnO films (∼1 µm) and the Mo electrode are deposited with the conditions provided in Section 3.1.1.

3.2.2 Structural and morphological properties of the Al and ZnO films

The film structure of the Al electrodes observed in SEM and AFM are shown in Figure 3.10. The histogram in Figure 3.10 (d) is obtained by determining the grain diameter of 100 particles on the SEM images and classifying the diameters in 10 nm size ranges to produce a spectrum of the distribution for each value of T_{S}. At low temperatures (25 °C) the Al surface consists of small grains (<100 nm in size) and low roughness (<10 nm); when T_{S} increases, the Al grains become larger (>100 nm), and more disordered, leading to an increase in rms surface roughness (∼16 nm) as shown in Figure 3.10 (a), (b) and (c). When $T_{\mathrm{S}} = 300$ °C, a mixture of large (>100 nm) and small Al grains are present as observed in Figure 3.10 (c) and

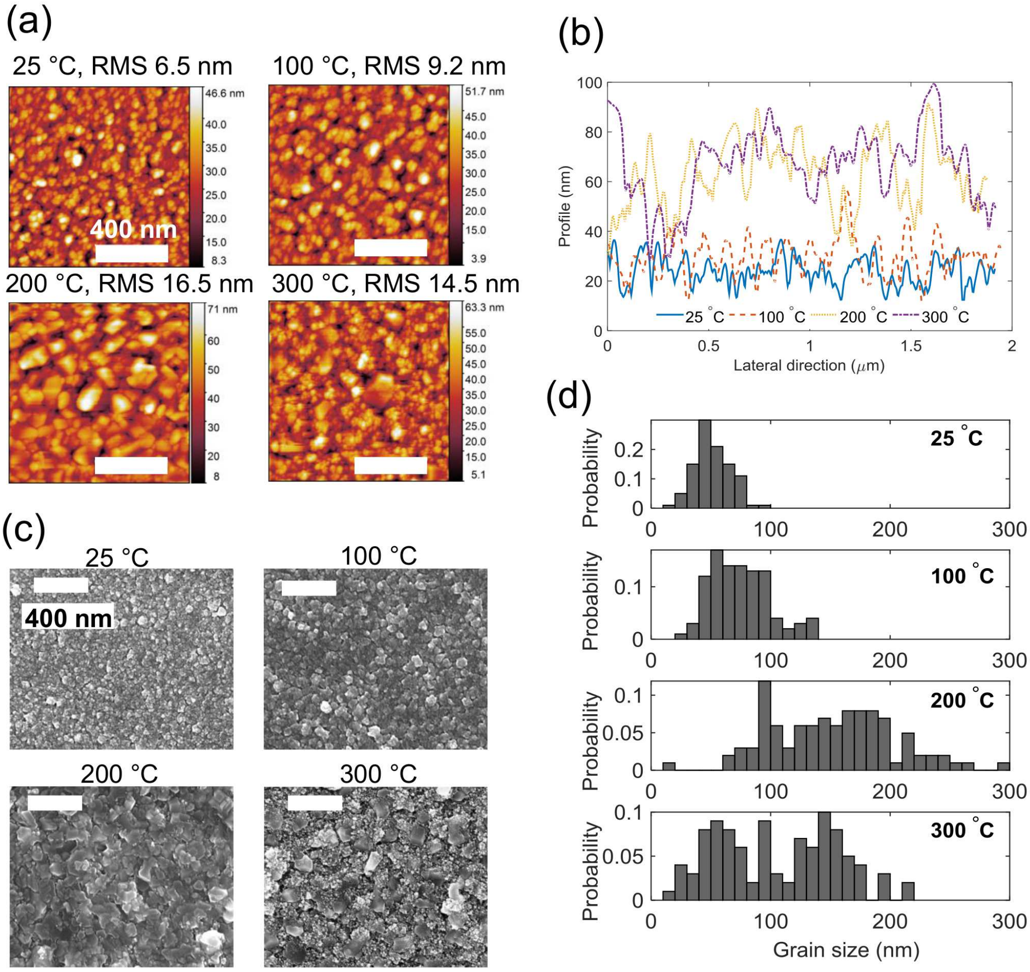

Figure 3.10: (a) Topography of the Al electrodes observed with AFM showing the effect of temperature on roughness, (b) Lateral cut profile across the AFM images showing increased roughness and grain sizes with $T_S < 300$ °C, (c) SEM images of the Al showing the increased grain sizes as temperature increases and a mixed phase at 300 °C and (d) Histogram of the grain size distribution of the Al electrode at different sputtering temperatures. All scale bars in (a) and (c) represent 400 nm.

(d). Nonetheless Al grains larger than 200 nm are less common when $T_S = 300$ °C compared to when $T_S = 200$ °C, which had grains of up to ~300 nm (Figure 3.10 (d)). Therefore the surface of the Al sputtered at $T_S = 300$ °C has lower roughness (14.2 nm) compared to when $T_S = 200$ °C, which has a roughness of 16.2 nm.

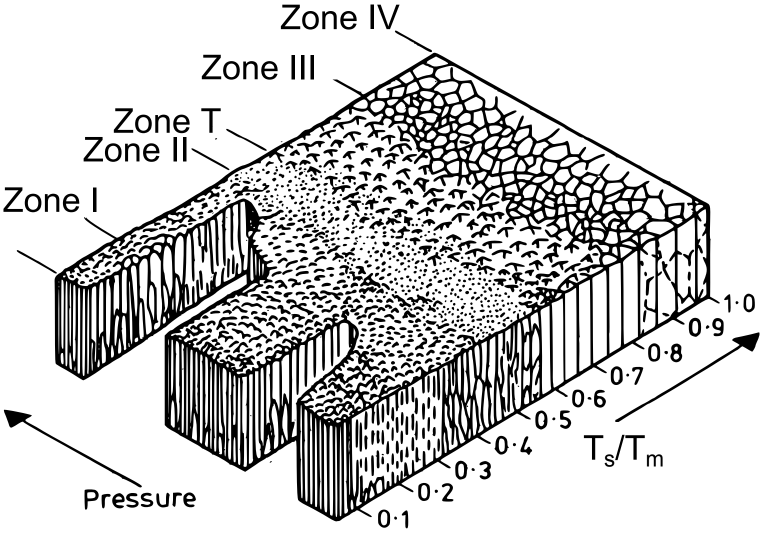

Figure 3.11: Schematic representation of the Thornton zone structure diagram[163] for sputtered materials at different pressures and substrate temperatures, T_S, showing the evolution of the grain structure with substrate temperature to melting temperature (T_S/T_M) ratios. In Zone I, the grains are porous and become larger as T_S/T_M increases. The transition zone (T) has densely packed and smaller grains and in Zone II the film crystallises and have large columnar grains.

The morphology of the Al films at different T_S observed in Figure 3.10 can be explained by the zone structure diagram.[163, 164] A schematic of the morphology of films sputtered at a different pressure and temperatures is illustrated in Figure 3.11. With a melting temperature (T_M) of 660 °C the different ratios of T_S/T_M can be related to the structures observed in Figure 3.10 (c).[165] When T_S is less than 200 °C, the ratio of T_S/T_M for the Al film is < 0.3 where the film structure will be in Zone I, thus being porous and having tapered crystallites, as illustrated in Figure 3.11. The roughness of these crystallites increases as T_S increases, which is observed in the growth of the Al electrodes. When $T_S = 300$ °C, the ratio of T_S/T_M for the Al layer is therefore 0.45 and the film morphology is located at the boundary of Zone T (transition) and Zone II (shown in Figure 3.11) leading to a mixture of densely packed fibrous (small) grains and columnar (large) grains, as shown in the grain distribution in Figure 3.10. Moreover in Zone T, the Al films have high residual compressive stress leading to poor adhesion to the substrate and hence delamination of films in contact with liquids.

SEM micrographs of the cross-section of the ZnO films subsequently deposited on the textured Al electrodes are displayed in Figure 3.12. An appreciable inclination angle (~30°) from the surface normal of the ZnO film is observed in each case. However when $T_\mathrm{S} = 25$ °C, the ZnO c-axis inclination angles are non-uniform as the ZnO microcrystals change orientation after the initial growth. This can because of the lower roughness (6.2 nm) of the Al electrode at $T_\mathrm{S} = 25$ °C, which does not favour the continuous and homogeneous growth of the inclined ZnO films. For the Al electrodes deposited at higher T_S, the ZnO films have more uniform c-axis inclination angles as observed in Figure 3.12 for $T_\mathrm{S} = 100$, 200 and 300 °C.

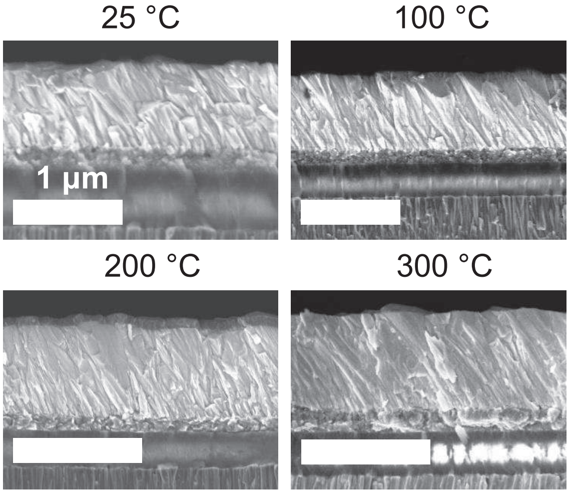

Figure 3.12: SEM cross-sections of the ZnO films deposited on the Al surfaces at different T_S, showing an appreciable inclination of ~30° from the surface normal. Uniform inclinations are observed at 100 °C, 200 °C and 300 °C. At 25 °C, the ZnO inclination is discontinuous as the film becomes thicker. All scale bars represent 1 µm. The last two reflector layers of SiO_2 and Mo are observable.

XRD pole figures of the (0002) orientation of ZnO (1 µm thick) around $2\theta =$ 34.42° (Figure 3.13 (a)) sputtered on Al deposited at different T_S shown in Figure

3.14 indicate that the c-axis inclination angle, Ψ, with respect to the surface normal is approximately 20°. When T_S increases from 25 °C to 200 °C, the ZnO c-axis inclination angles are more distributed (area of maximum contour intensity in Figure 3.14 increases), and follows a similar trend to the Al grain size distribution (Figure 3.10 (d)) except when T_S = 100 °C. In addition the mean c-axis inclination angle (center of red regions in Figure 3.14) of the ZnO films shifts gradually from $\sim$20° to $\sim$26° as the Al T_S increased from 25 °C to 300 °C. At T_S = 300 °C, the mean c-axis inclination angle is approximately 26° (Figure 3.13 (b) for Φ cuts along the maximum intensities). The inhomogeneous Al grain distribution and larger grains at 200 °C and 300 °C cause a wider distribution in the Ψ value ($\sim$ 40°, and area enclosed in Figure 3.14 are > 100 unit^2), and hence more disperse ZnO c-axis inclination angle around the average value as shown in Figure 3.14. At 300 °C the population mix of small and large Al grains improves the intensities observed compared to when T_S = 200 °C, which is dominated by mostly large grains causing smaller intensity. The morphologies of the Al and ZnO films demonstrate that homogeneous c-axis inclination angles can be achieved when the Al films are sputtered at temperatures, $T_\mathrm{S} < 200$ °C. In this work the optimum T_S is therefore 100 °C as the ZnO c-axis inclinations are more concentrated around a mean angle of 20° compared with other values of T_S. At lower T_S the dispersion is large and the mean c-axis inclination is less than 20° as the surface does not have the optimum roughness to promote the homogeneous c-axis inclinations and the grains re-orient in the more energetically favorable c-axis oriented direction. The difference in Φ for T_S = 25 °C is caused by sample positioning in the XRD scans and has no effect on determining Ψ.

3.2.3 Electro-acoustic characterisation

The electrical admittance, $Y(S)$ spectra of typical devices with T_S = 100 °C are shown in Figure 3.15 (a). The reflector transmittance (red dashed line in Figure 3.15 (a)) is simulated with the Mason transmission line model to ensure that the shear resonance is confined within the ZnO layer.

The shear mode resonant frequency of the device shown in Figure 3.15, f_S is 1.10 GHz while the longitudinal mode frequency, f_L is 2.18 GHz. From Figure 3.15 (a), it can be observed that the shear resonance is located within the reflector

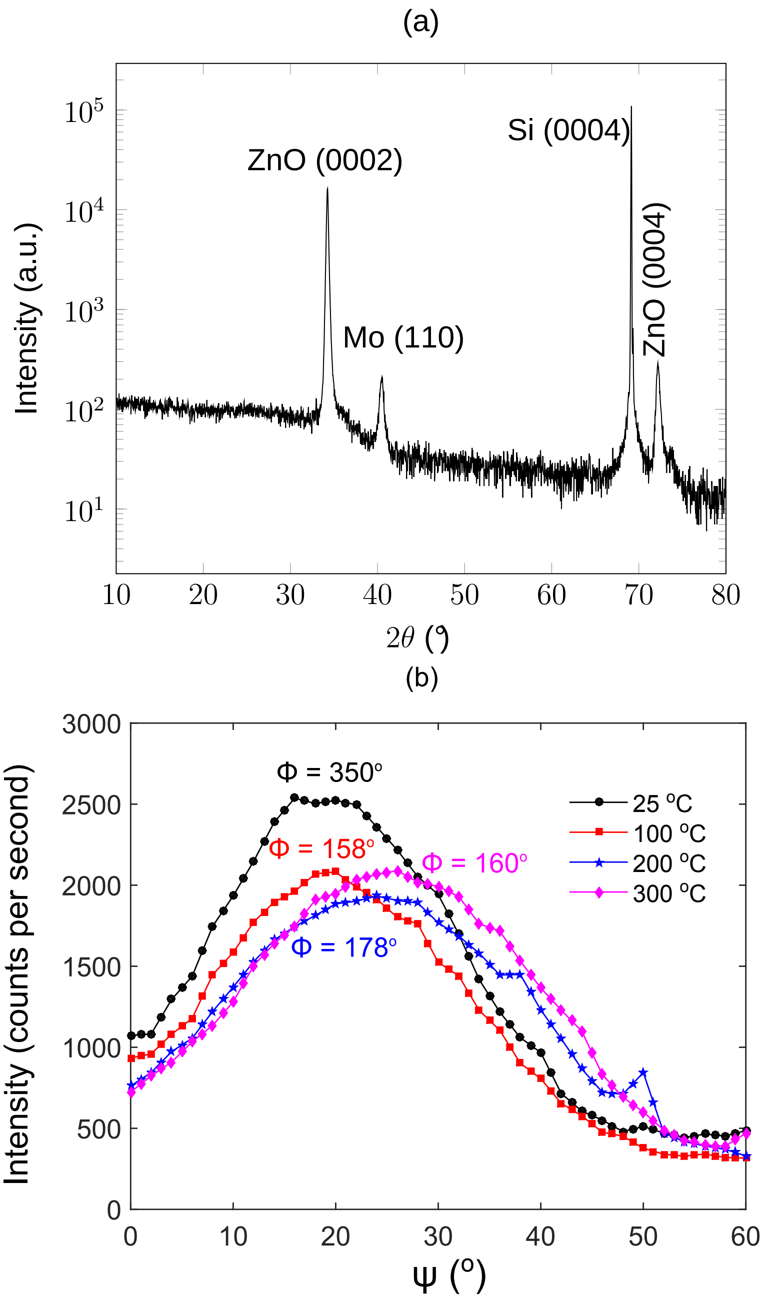

Figure 3.13: (a) X-ray diffraction spectrum of ZnO fabricated on the acoustic reflectors showing the presence of the ZnO peak at 34.42° (b) XRD intensity at the position where the maximum intensities occur, with the different values of T_S showing that the c-axis inclination angle increases as T_S increases but the distribution also increases.

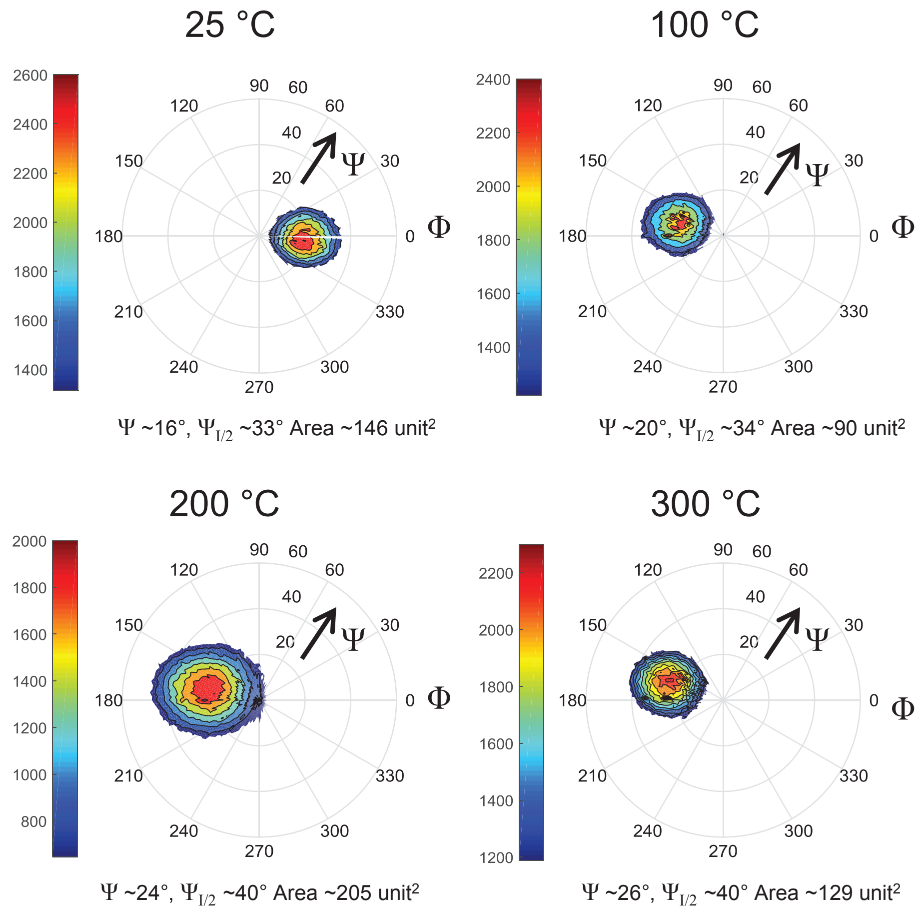

Ψ ~16°, $\Psi_{I/2}$ ~33° Area ~146 unit²

Ψ ~20°, $\Psi_{I/2}$ ~34° Area ~90 unit²

Ψ ~24°, $\Psi_{I/2}$ ~40° Area ~205 unit²

Ψ ~26°, $\Psi_{I/2}$ ~40° Area ~129 unit²

Figure 3.14: X-ray pole figures of ZnO grown on Al deposited at different T_S, showing distribution of *c*-axis inclination angles with respect to the surface normal ($\Psi = 0$). The calculated areas enclosed within the contour surrounding the maximum intensity indicate the dispersion of the *c*-axis inclination angles. Narrower dispersions (smaller area) are observed when ZnO is deposited on Al sputtered at $T_S = 100$ °C. Large dispersions are observed in the case of Al sputtered at T_S of 200 °C and 300 °C. A gradual increase of the mean value of Ψ (position of center of red regions) and the FWHM ($\Psi_{I/2}$) of the peak intensity can be observed as T_S increases from 25 °C to 300 °C.

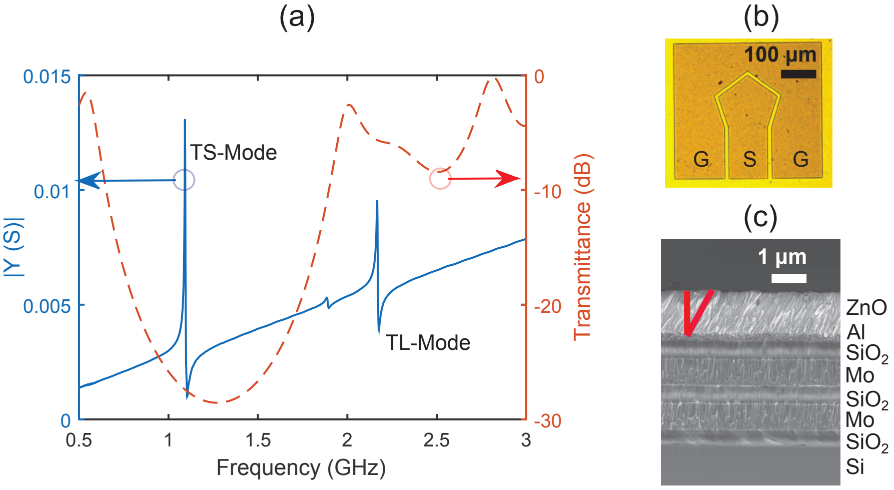

Figure 3.15: (a) Electrical admittance spectrum of a typical device showing a TSM resonance at 1.1 GHz and a TLM at 2.2 GHz. Dashed red line shows the modelled shear mode transmittance spectrum of the fabricated acoustic reflector. (b) Optical image of a device on the inclined *c*-axis ZnO. (c) SEM cross-section of a device before top electrode showing a inclination of ∼30° in the ZnO and acoustic reflector layers.

bandwidth, thereby ensuring an efficient reflection of the shear wave. A resonance of smaller amplitude can be observed at 1.8 GHz, which corresponds to resonances from the reflector layers that are either thinner or thicker than estimated during the deposition process.

The impedance spectra for all the best devices measured for each T_S are shown in Figure 3.16 demonstrate values of f_L/f_S between 1.98 to 2.01, corresponding to theoretical *c*-axis inclinations of approximately 20° to 25°.[95] However this value is only an estimate as the material properties are assumed to be those of bulk ZnO. Q_r and k^2_{eff} outlined in Table 3.4 are calculated for each set of Al deposition temperatures using the standard definitions from Chapter 2.

Figure 3.17 is obtained by extracting the values of 25 devices from each set and calculating the average values and standard deviation (error bars) in each direction from the mean value. These values are tabulated in Table 3.4. SMRs with ZnO grown on Al deposited at 100 °C had the highest shear mode Q_r. Devices are measured with Q_r of up to 180 as shown in Figure 3.17 (a). Therefore the optimum

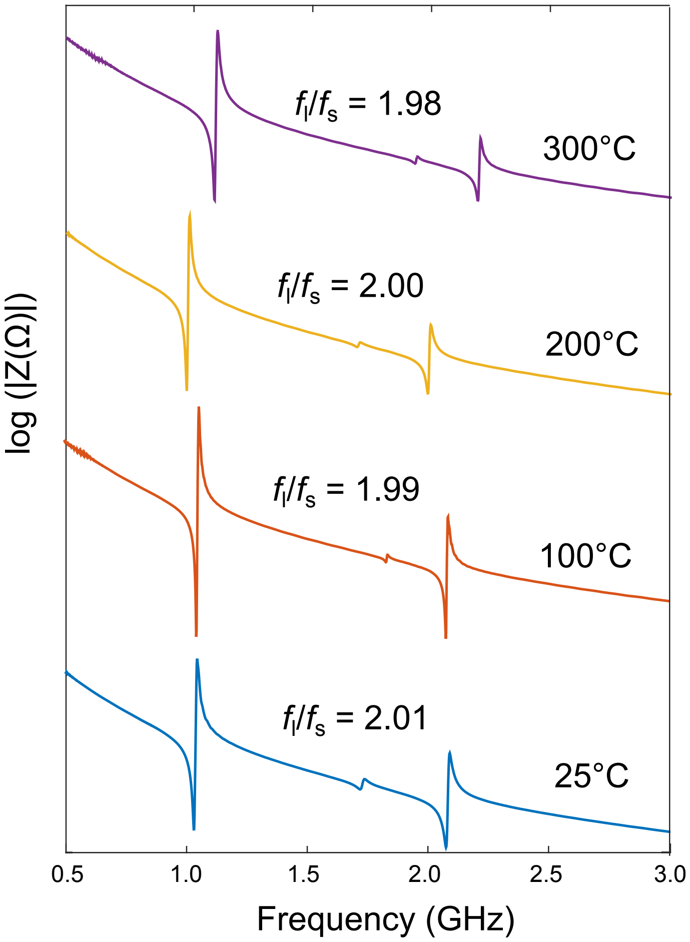

Figure 3.16: Electrical impedance spectra of devices with Al at different T_{S}, the graphs have been separated for clarity. The performance of samples with Al grown at $T_{\mathrm{S}} = 100$ °C gives the best performance for both the longitudinal and shear modes.

Table 3.4: Shear mode performance of typical devices (25 best devices) measured at different T_{S}

T_{S} (°C)	f_S (GHz)	Q_r	Q_a	k^2_{eff} (%)	$f_L//f_S$
25	1.00	138	110	2.48	2.01
100	1.00	145	110	2.90	1.99
200	0.98	133	109	2.22	2.00
300	1.00	123	94	3.59	1.98

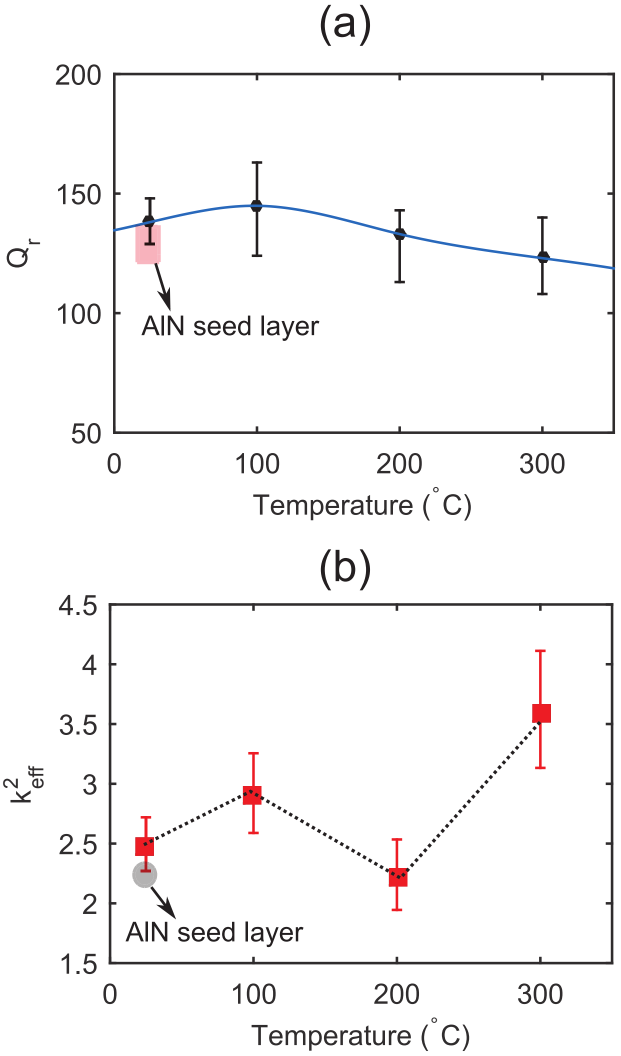

Figure 3.17: The average Q_r of devices measured at each Al deposition temperature, T_{S}, the highest Q_r is achieved at 100 °C. (b) shows the k^2_{eff} of devices, which follow a similar trend as Q_r except at 300 °C where a mean k^2_{eff} of 3.5 is achieved. Shaded areas show the performance of devices from section 3.1 using AlN seed layer to grow inclined *c*-axis ZnO.

T_S for the electrode surface is determined to be 100 °C. At this temperature, the surface has the ideal roughness to promote the homogeneous growth of the inclined ZnO, achieving the highest average Q_r of 150 (Figure 3.17 (a)). This value decreases at higher T_S because of the increased roughness as the series resistance, R_s increase. At lower T_S, the shear mode is not effectively excited leading to both a lower Q_r and k^2_{eff} as displayed in Figure 3.17. This is because the Al surface has low roughness, which does not favour the ZnO grains to orient in an inclined c-axis. The rough electrode without the use of a seed layer such as AlN ensures a higher piezoelectric performance of the shear mode ZnO. When T_S is 300 °C, the highest k^2_{eff} of ~3.5% is obtained, which is probably because of the wide distribution of different grain sizes in the Al film leading to the presence of grains of the appropriate sizes and roughness to promote the TSM mode. This is also evident in the larger error bars in the case of T_S = 300 °C demonstrating the variations across the devices. Nevertheless the SMRs fabricated at this T_S value exhibit high stress and delaminate easily in the fabrication steps, and the SMR yield was consequently low when T_S = 300 °C. Using the electro-acoustic spectra of the best devices measured, the equivalent mBVD model parameters are extracted and listed in Table 3.5.

Table 3.5: MBVD model parameters extracted for the inclined c-axis ZnO grown at different T_S, average of 10 devices are used for each set.

T_S (°C)	C_0 (pF)	C_m (pF)	L_m (µH)	R_m (Ω)	R_0 (Ω)	R_s (Ω)
25	0.762	0.0170	1.60	101.96	11.60	8.65
100	0.790	0.0167	1.45	64.90	13.81	10.22
200	0.730	0.0154	1.62	81.88	16.93	12.02
300	0.731	0.0157	1.44	72.33	14.12	8.26

In order to obtain a comparison among the different surfaces analysed in this chapter, the ratio of the mBVD model parameters for Q_r, Q_a and k^2_{eff} as described in section 2.6.2 are calculated and listed in Table 3.6. The second column in Table 3.6 relates to Q_r, the third to Q_a and the fourth to k^2_{eff}. It is observed that all the ratios are improved by the use of an electrically conductive textured electrode with controlled roughness. This has been demonstrated by the enhanced electromechanical parameters experimentally and extracted mBVD circuit equivalents. Comparing the Al electrode at T_S = 100 °C, it is shown that the improvement is approximately

Table 3.6: Ratio of extracted MBVD model parameters to compare textured Al electrodes with AlN seed layers and rough reflectors independent of f_S

Surface	$\frac{L_m}{R_s+R_m}\left(\frac{1}{10^6\ \text{Hz}}\right)$	$\frac{L_m}{R_0+R_m}\left(\frac{1}{10^6\ \text{Hz}}\right)$	$\frac{C_m}{C_0+C_m}$ (%)
Rough reflector	0.064	0.062	1.5
AlN seed layer	0.100	0.093	1.8
Al (T_S = 100 °C)	0.121	0.116	2.1

1.2 times in all the parameters. A quick comparison for Q_{mech} between SMRs using the polycrystalline seed layer and those with textured Al can be obtained by analysing L_m/R_m ratios, demonstrating that the SMRs with the textured Al have higher Q_{mech}, as expected. Further improvements in Q_r can be achieved by the use of a textured electrode such as W due to its higher acoustic impedance compared to Al that can confine the mechanical resonance in the piezoelectric layer, thereby suppressing the acoustic leakage through the reflector. However its high T_M also implies that the substrate temperatures need to be high to achieve similar effects as with Al. In addition the HiTUS cannot be safely run at temperatures higher than 300 °C to cause similar effects in W. Although the inclination angle using textured Al electrodes is ~20-30°, compared with AlN seed layers where an inclination of 45° is achieved, the shear mode is most effectively excited (higher k^2_{eff}) by a *c*-axis inclination angle of 20-40°.[6] This inclination angle of the *c*-axis can be increased by further reducing the target to substrate distance to cause a larger offset of the target center to the substrate.

3.3 Chapter conclusion

In summary shear mode devices with high Q_r (>150) are successfully fabricated using an inclined *c*-axis ZnO with thickness ranging from 800 nm to 1 µm. This is achieved using an off-axis deposition by positioning the substrate at a distance from the center of the target and a surface with specific roughness. Different surfaces were tested: a rough reflector layer, polycrystalline AlN seed layer with (103) orientations, and textured electrodes. Homogeneously textured surface are found to be ideal for improving the uniformity of the *c*-axis inclinations compared to random roughness. Textured Al electrodes provide the optimum roughness and conductivity necessary to excite the shear mode resonance; and the ideal inclination angles are achieved with Al electrodes sputtered at a temperature of 100 °C. With this surface a rms roughness of $\sim$9.2 nm is obtained and SMRs demonstrate Q_r as high as 180, and k^2_{eff} of 3%. In Chapter 4 the possibility of having a CNT layer on the surface to isolate the TLM mode from liquid will be discussed.

Chapter 4

Carbon nanotubes integration for SMRs in liquid

In this chapter, the growth optimisation of CNTs on the SMRs will be described. The aim of this work is to mitigate the damping in liquid by using a CNT forest to provide an acoustic mismatch between the BAW resonator and the liquid. More specifically, the investigation will focus on the TLM and the potential of dense CNT forests to enable biosensing with the longitudinal mode owing to its more scalable fabrication process compared to the inclined *c*-axis for shear mode resonators. Challenges in achieving this objective include the height optimisation of the forest to ensure the mechanical wave is still sensitive and the forest density to ascertain that the liquid does not not directly contact with the resonator, which eventually reduces the longitudinal propagation through the liquid.

CNTs can be grown using different methods such as arc-discharge, laser vaporisation or chemical vapour deposition. Arc-discharge uses evaporation of graphite electrodes in electric arcs that involve very high ($\sim$4000 °C) temperatures. Although arc-grown CNTs are well crystallised, they are highly impure; about 60-70% of the arc-grown product contains metal particles and amorphous carbon.[166] In laser-vaporisation a high purity graphite is evaporated by high-power lasers in a high temperature furnace. Despite the higher purity of CNTs grown with this method, the yield is low.[167] On the other hand, chemical vapor deposition (CVD) uses a catalyst-assisted thermal decomposition of hydrocarbons to synthesise CNTs. CVD is an inexpensive and scalable process for large scale growth of CNTs.[168]

Figure 4.1 shows a schematic diagram of the experimental set up used for CNT growth by CVD method in this work. The process is carried out in a cold wall chamber with a graphite heater that is powered by a DC supply and a type-K thermocouple is used to monitor the temperature during growth. CNT growth is achieved by passing a hydrocarbon vapour at sufficiently high temperature (400-1200 °C) over a substrate, on which a catalyst material is present to assist with the decomposition of the hydrocarbon.[168] The hydrocarbon, catalyst, temperature, pressure, gas-flow rate, deposition time, and reactor geometry all play very important roles in the growth of CNTs.[60] In this work the catalyst, temperature, gas flow rates and deposition times are changed to achieve the dense CNT forests. All the parameters are controlled by a software (NanoUSB v1.1) created by Aixtron AG. Low-temperature CVD (300-900 °C) generally yields MWCNTs, whereas a high-temperature (900-1200 °C) reaction is more favourable for SWCNT growth.[60] SWCNTs have a higher energy of formation due to smaller diameters and higher

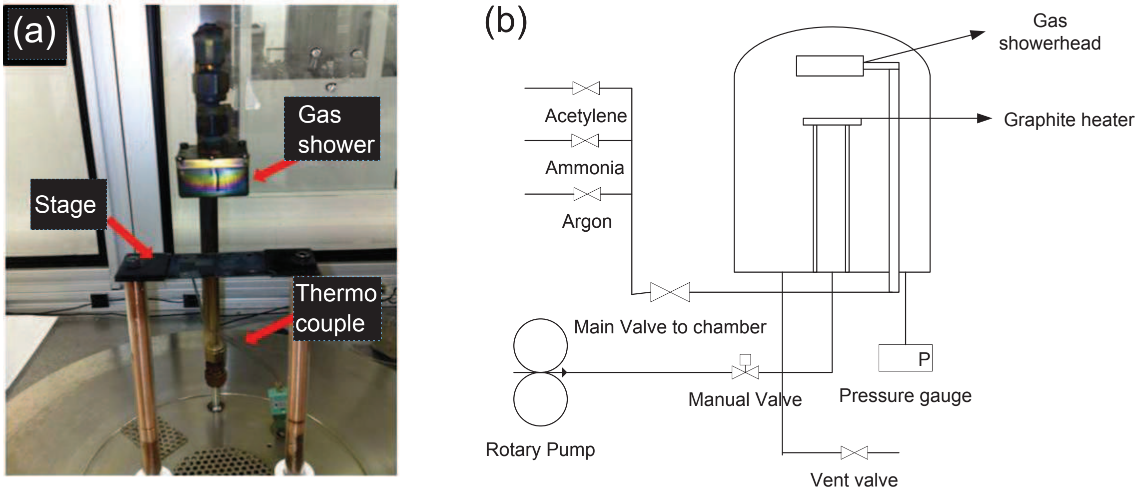

Figure 4.1: (a) Photograph of the cold wall CVD system (Black Magic II) used to grow CNTs, with a graphite stage powered by a DC supply and a gas showerhead at a distance of 3 cm from the stage. (b) Schematic of the cold wall CVD system with the available valves and the gases to grow CNTs, a glass bell jar is used to cover the equipment.[59]

strain energy caused by their smaller radius and therefore larger strain compared to MWCNTs.[169, 170] Therefore MWCNTs are easier to synthesise compared to SWCNTs. Hydrocarbons such as CO or CH_4 are usually preferred for SWCNT growth owing to their stability at high temperatures.[169] In contrast MWCNTs are synthesised with hydrocarbons such as acetylene or benzene; however their instability at higher temperature cause amorphous carbon deposits.[169] Catalyst nanoparticles assist the hydrocarbon decomposition at lower temperature, and catalyst engineering can be used to grow SWCNTs at lower temperatures.[171] Catalysts such as Fe, Ni and Co are typically used because carbon diffuse easily in these metals at the growth temperature.[168, 172] In addition the high melting point and low equilibrium vapour pressure of these metals allow for a larger CVD growth window and CNT growth reproducibility.[173]

The chapter begins with the initial growth of dense CNTs with a Co/Mo/Ti catalyst structure and the results achieved. The work described in this chapter is necessary to compare the effects of the CNTs when used as surface coatings for the BAW resonators. Taller and more reproducible CNT forests are then grown with Al/Fe bi-layer system on AlN SMRs, and the effect of DI water on the TSM and TLM are compared. Attempts are also made to densify the forest further with solvents.

4.1 High mass density CNTs with Co/Mo/Ti system on ZnO SMRs

Initially a low temperature process for growing high mass density and well-packed CNTs is chosen as a demonstration that such a layer can be feasibly grown on the ZnO SMRs. Sugime *et al.* [174] demonstrated that the presence of an interlayer of Mo between a Co-Ti bi-layer can achieve well packed, short and high density CNTs. The thicknesses of the Ti and Co are fixed at 5 nm and 2.5 nm respectively.[174, 175] In addition Co-Mo and Fe-Mo have been reported to enhance the growth of nanotube forests on insulators. The presence of Mo on the Ti layer effectively stabilises small Co[176, 177] or Fe [178] nanoparticles by forming complex carbides or oxides [179, 180] even when the Mo thickness is 1 nm.[178, 181] Co is used here as it can form small nanoparticles at a lower temperature compared to Fe. During this work the top electrode chosen was Au/Cr (Figure 4.2 (a)) because a thick Mo electrode inhibits the growth of the CNTs using this catalyst combination. Different thicknesses of the Mo layer are tested and the results are shown in Figure 4.2 (c). The layers of Co, Mo and Ti are deposited in a DC magnetron sputterer with the conditions outlined in Table 4.1. Between each deposition, the samples are exposed to air.

Table 4.1: Deposition conditions for metal layers for dense CNT growth

Parameter	Ti	Mo	Co
Ar flow (sccm)	30	30	30
Pressure ($\times 10^{-3}$ mbar)	3.5	3.5	3.5
Target clean power (W)	100	100	100
Target clean time (s)	600	600	600
Deposition power (W)	100	20	20
Deposition rate (nm/min)	3.6	1.7	1.9

The growth of the dense CNTs is then carried out using the conditions outlined in Table 4.2. The cold wall chamber is pumped down to 6.0×10^{-2} mbar and NH_3 (ammonia) is added before ramping up the temperature by 200 °C/min to reach the growth temperature of 450 °C and stabilised for 60 s. For the growth, the NH_3 is stopped and the carbon feedstock (C_2H_2, acetylene) is added to grow the dense CNTs. After the growth time (3 mins), C_2H_2 is turned off and Ar is switched on to cool down the chamber until less than 50 °C after which the samples are unloaded.[174, 175] From Figure 4.2 (c) it can be observed that the thickness of the Mo has a strong influence on the CNT morphology. As the thickness of

Table 4.2: Growth conditions for high density CNTs

Parameter	Value
C_2H_2 flow rate	200 sccm
NH_3 flow rate	200 sccm
Growth time	3 min
Pressure	8 mbar

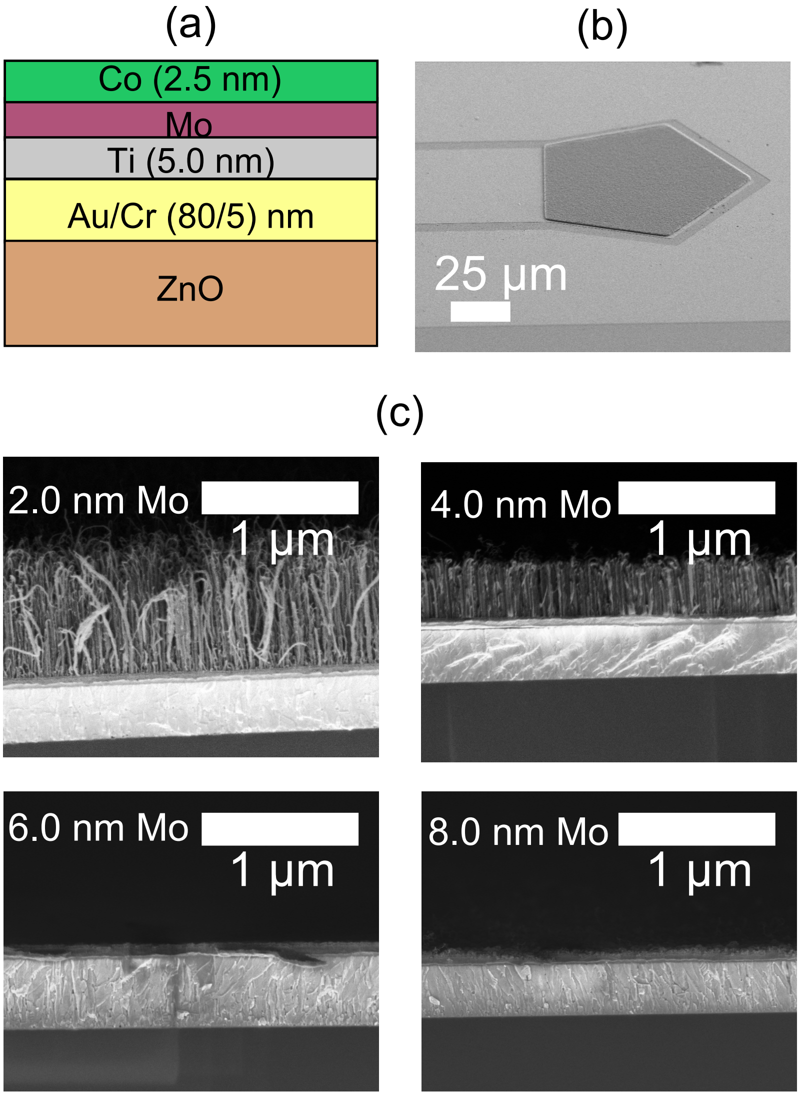

Figure 4.2: (a) Representation of the layers above ZnO consisting of an Au/Cr electrode, with a 5.0 nm Ti layer for adhesion with Mo (variable thickness) and 2.5 nm Co. (b) SEM image of the dense CNTs grown on the active area, the forest thickness is ∼1 µm. (c) SEM cross-sections of the ZnO and CNT layers with different thicknesses of the Mo interlayer

Mo increases from 2.0 nm to 4.0 nm, the CNT forests become shorter and denser. However as the thickness of Mo exceeded 5 nm, the CNTs are very short and the growth is slower. 4.0 nm of Mo demonstrated the best compromise between density and thickness of the forest compared to 2.0 nm of Mo where the CNTs are not well aligned along the vertical axis. The thickness of Mo to achieve similar CNTs is higher than reported by Sugime *et al.* [174], which can be because of the roughness of the ZnO underneath the Au/Cr electrode, requiring a thicker Mo layer to form a film compared to Sugime *et al.* [174] who used Mo thicknesses ranging from 0.3 to 1.0 nm on Cu deposited on polished SiO_2. Despite achieving dense CNTs on the device active areas as shown in Figure 4.2, the SMRs fabricated do not show any resonance; this is attributed to the acoustic damping caused by the high mass density CNTs and the reduction of ZnO exposed layer to Zn by flowing NH_3 during the annealing step. Other commonly used gases such as H_2 also react with ZnO but inert gases such as Ar cause the nanoparticles to be larger than with NH_3 or H_2 and the resulting CNT forest will not be vertically aligned.[61] Moreover the growth of this type of CNTs is not reproducible on different samples and required substantial change to the catalyst thicknesses between layers of different roughness.

4.2 High forest density CNTs with Fe/Al system

To address the issues observed with the growth of CNTs on the ZnO SMRs, a different approach is adopted to grow high forest density and vertically aligned (VA) CNTs with an Fe/Al system, which also enabled the growth directly on Mo, thereby obviating the presence of an acoustically lossy Au layer. This method was demonstrated by Mirea *et al.* [61] and Olivares *et al.* [182] for the growth of vertically aligned and tall CNTs on electrodes commonly used for FBARs and SMRs. Fe is the catalyst, which is stabilised by the presence of the lower surface energy material Al during the growth.[61] Similar to the growth in the previous section, NH_3 is introduced at a rate of 100 sccm in the chamber to raise the pressure to 1.6 mbar and stabilised for 30 s. The substrate is subsequently heated up to growth temperature (ranging from 450 °C to 650 °C) and stabilised for 300 s. Upon heating, the Fe catalyst dewets to form nanoislands and by varying the thickness of Fe (from 0.5 nm to 4.5 nm), different sizes of nanoislands are formed leading to CNTs with different densities and thicknesses. After the annealing step, C_2H_2 is added to commence growth. The ratio of NH_3 and C_2H_2 is 1:1 to prevent the deposition of amorphous carbon during the growth. After the growth time has elapsed, the heater is turned off, and C_2H_2 and NH_3 are switched off before flowing Ar until the system cools down to less than 50 °C. A schematic of the growth process is shown in Figure 4.3.

The Fe/Al layers can either be thermally evaporated in an Edwards E306 evaporator or deposited by DC magnetron sputtering using the White Magic sputter system, the conditions of which are summarised in Table 4.3 with no substantial difference between the two deposition techniques. After each layer, the samples are again exposed to air.

Table 4.3: Deposition conditions for the catalyst layers by sputtering

Parameter	Al	Fe
Ar flow (sccm)	30	30
Pressure ($\times 10^{-3}$ mbar)	3.5	3.5
Target clean power (W)	100	100
Target clean time (s)	600	600
Deposition power (W)	100	20
Deposition rate (nm/min)	4.7	0.6

Attempts are intially made on longitudinal mode ZnO to test the conditions and viability of the SMRs with CNTs on top as shown in Figure 4.4. However no resonance is observed on the devices and it became evident that the ZnO film reacts strongly with NH_3 and is etched away at temperatures higher than 500 °C as illustrated in Figure 4.4 (b). A passivation and insulating layer that remains unreacted in the annealing step is therefore necessary to protect ZnO for CNT growth, however this increases the complexity of the fabrication process. Although at lower temperatures the CNTs grow as demonstrated in Figure 4.4 (c) and (d), the devices are still electrically shorted as the ZnO reacts with the reducing gas, which eventually increases the conductivity of the ZnO exposed surface.[183, 184]

Consequently experiments are carried out of longitudinal mode AlN SMRs as depicted in Figure 4.5. From these experiments no etching is observed even at

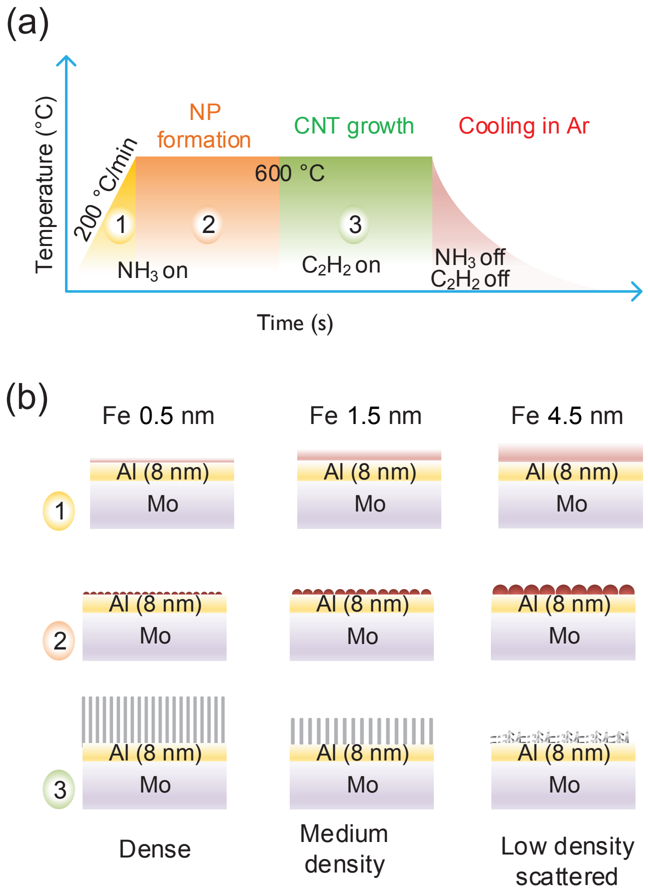

Figure 4.3: (a) Graphical representation of growth of high forest density using Fe/Al system with a 200 °C/min ramping in NH_3 in stage 1. Stage 2 is carried out at a fixed temperature to stabilise and form the nanoparticles, after which the carbon feedstock C_2H_2 is added to commence the growth in stage 3. After growth both NH_3 and C_2H_2 are turned off after the heater is switched off and cooling is carried out in an Ar atmosphere. (b) Representation of the top layers of resonators during the three stages. Different thicknesses of Fe can tune the forest density and height, with 0.5 nm Fe giving the highest density and tallest CNTs while when Fe > 3 nm, the forests are no longer vertically aligned and become “spaghetti” like.

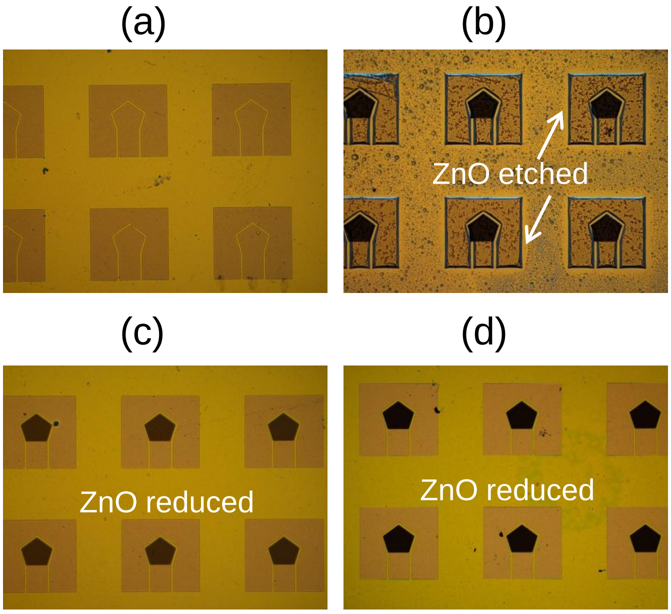

Figure 4.4: (a) No pattern on the active area of the SMR, (b) CNTs grown on ZnO SMRs at 650 °C where ZnO is etched, (c) shorter CNTs grown at 450 °C for 1 min, (d) longer CNTs grown at 450 °C for 3 min.

higher temperatures (>600 °C). However the ramping rate of the annealing step is critical during the process. A high ramping rate of 5 °C/s causes the AlN layer and the underlying reflector layers to delaminate as observed in Figure 4.5 (d) due to residual stress in the film. At lower ramping rates, the CNTs are grown, however the forests are either less dense or short due to agglomeration or the inability of the Fe layer to be activated. A ramping rate of 3-4 °C is chosen as a compromise to minimise delamination of the layers (Figure 4.5 (c)) while avoiding Ostwald ripening of the catalyst.[185]

The TLM performance of the SMRs with different ramping rates are measured and shown in Figure 4.6 (a). At higher ramping rates such as 5 °C/s, the resonance is unclear and less pronounced than at lower ramping rates. However at lower ramping rates tend to form amorphous carbon due to the inactive catalyst layer which causes a larger mass load, and hence larger Δf_r from the SMRs without CNTs, compared to higher ramping rates as observed in Figure 4.6 (a). The trade-off ramping rate of 3 °C/s demonstrated clear resonance and anti-resonance peaks;

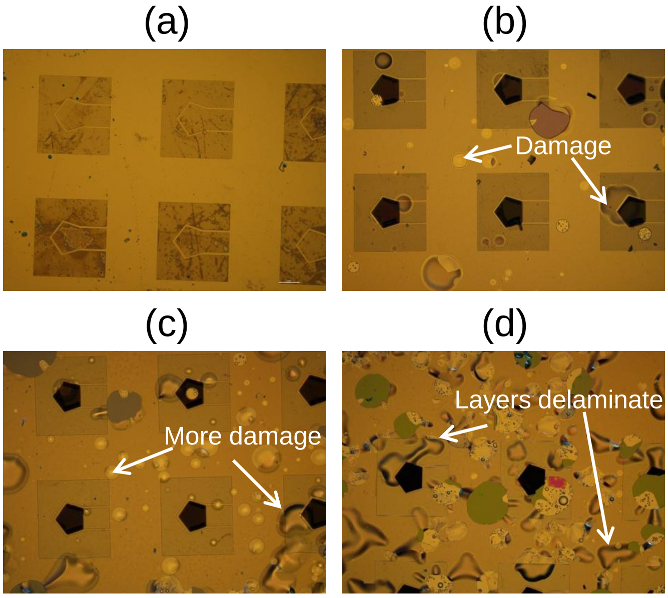

Figure 4.5: (a) No pattern on the active area of the SMR, (b) CNTs grown on AlN SMRs at 650 °C for 3 min with 1 °C/s, (c) CNTs grown on AlN SMRs at 650 °C with 3 °C/s (d) CNTs grown on AlN SMRs at 650 °C with 5 °C/s where the SMR layers delaminate.

nonetheless the peaks are less pronounced compared to the SMR without CNTs, which therefore indicate the addition of acoustic losses by the presence of the CNT layer on the SMRs.

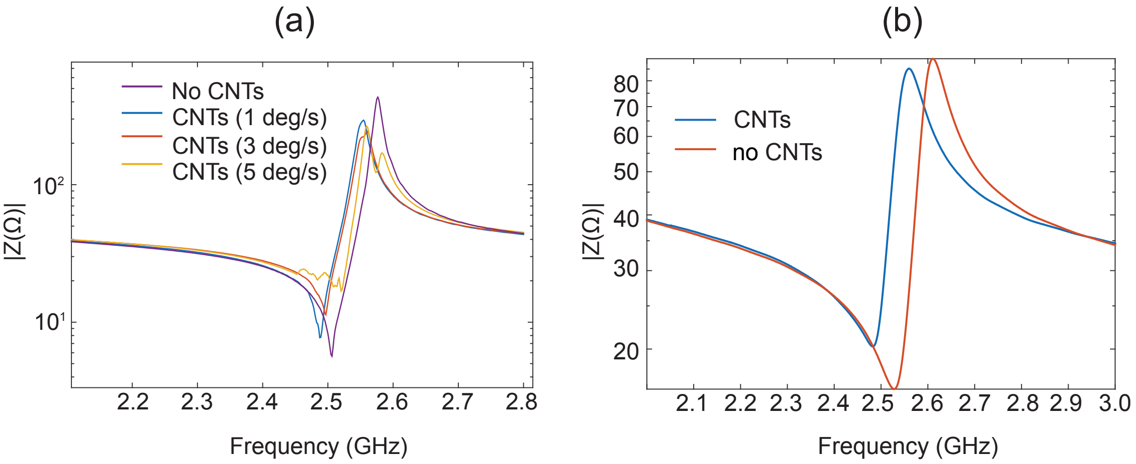

Figure 4.6: (a) Performance of the longitudinal mode AlN-SMRs with CNTs grown at different ramping temperatures. The performance degrades as the ramping speed is increased from 1 to 5 °C due to delamination problems, however a slow ramping speed also gives less dense and shorter CNTs. A tradeoff ramping speed of ∼3 °C is therefore chosen. (b) Effect of IPA on the electrical response of the SMRs with and without CNTs. No significant improvement is observed with the presence of the CNTs as IPA tends to penetrate though the CNT forest due to surface tension.

An experiment using isopropyl alcohol (IPA) on the resonator surface to assess if the CNTs can function as an isolation layer between the resonator and the liquid as shown in Figure 4.6 (b). 50 µL of IPA is dropped on the resonator while measuring the electrical impedance of the resonators. Both the SMR with CNTs and without CNTs have similar Q_r drops of 85%. However this experiment was unsuccessful as IPA is not an ideal liquid for testing the isolation, which therefore wets the CNT forests better than DI water, and causes the liquid to be in direct contact with the resonator.[186]

4.3 Shear mode AlN SMRs for growth of CNTs

The issues with the delamination of the SMR layers are then alleviated by depositing reflector layers optimised for high temperature applications. This optimisation procedure is carried out by Teona Mirea at the Polytechnic University of Madrid, and consists of thermally oxidising Si wafers (wet-oxidation) to obtain ~620 nm of SiO_2 and depositing reflector layers consisiting of Mo (~650 nm) and SiO_2 (~620 nm) sequentially in a Leybold Z550 sputtering system to form a reflector stack of 5 layers with a reflection centered around a frequency of 2.2 GHz for the longitudinal mode. The top reflector layer is polished mechanically using alumina slurry to reduce the roughness to less than 2 nm.

Ir (~150 nm) is deposited as the bottom electrode by electron beam evaporation and patterned by Ar ion-milling using a hard mask of Mo (~400 nm), which is deposited using the Leybold Z550 sputtering system. The ion milling process is carried out in a Phillips RIE system with 200 W RF power, 50 sccm of Ar and an etching pressure of 20 Pa for ~30 mins. Commercial Al etchant is then used to remove the remaining Mo mask. AlN sputtering is performed in an ultra-high-vacuum system, pumped to a base pressure below 8×10^{-7} Pa.[187] A pulsed DC source (MKS ENI 235) operating at 250 kHz powers a high purity (99.999%), 150 mm diameter Al target in an 60% N_2 in Ar admixture. To investigate the effect of CNTs on the shear resonance, inclined *c*-axis AlN layers are grown, which is achieved by growing an AlN seed layer prior to the piezoelectric AlN, at high pressure (0.66 Pa) and 600 W without intentionally heating or biasing the substrate. With these conditions seed layers with mainly (103) orientation are deposited, which is essential to promote the growth of the subsequent AlN films with inclined microcrystals to excite the shear resonance. The seed layer promotes the growth of AlN films with the wurtzite *c*-axis inclined up to 24° with respect to the surface normal with the substrates placed between 2 and 5 cm from the target axis.[50]

The piezoelectric AlN films (~1-1.2 µm thick) is sputtered at lower pressure (0.27 Pa), and 1200 W pulsed DC power, while maintaining the substrate at 550 °C and applying a DC bias of -50 V to keep the residual stress below 200 MPa. The top electrode of Mo (~150 nm) is sputtered in a the White Magic sputter coater with 100 W DC power from a 99.95% Mo target in a 0.35 Pa Ar atmosphere.

This top electrode is then patterned by standard UV photolithography using S1818 Microposit photoresist and dry etched with reactive ion etching using CF_4/O_2 chemistry. For the devices with CNTs, the active area is defined (Figure 4.7 (b)) using standard UV photolithography (AZ2020 nLoF photoresist). The catalyst layers of Fe and Al are deposited by thermal evaporation before growing the CNTs by CVD. A completed device is shown schematically in Figure 4.7.

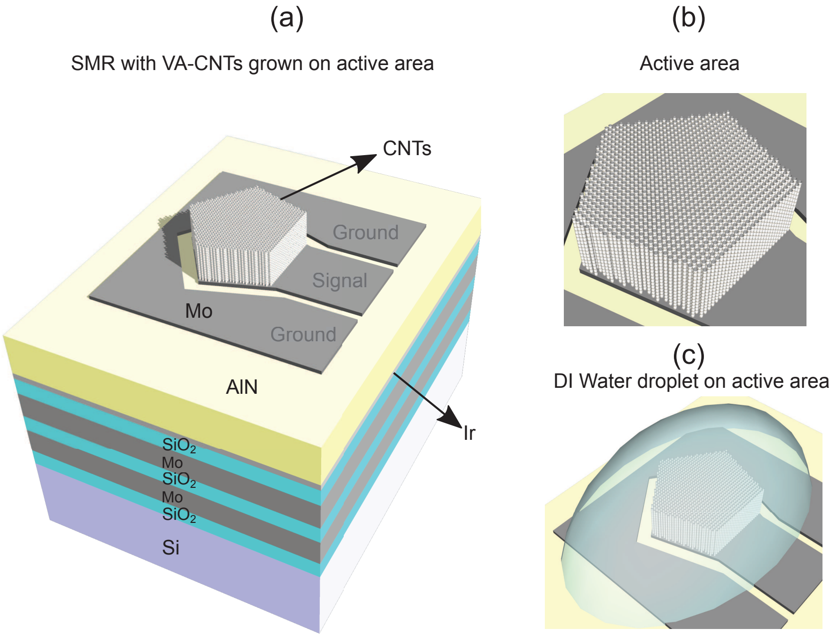

Figure 4.7: (a) Schematic of the SMR structure fabricated on Si showing the 5 layer acoustic reflector, the piezoelectric AlN layer and the top electrode on which VACNTs are grown to cover the active area as shown in (b) and (c) DI water is dropped to cover the resonator active area.

After the fabrication of the devices, the CNTs with different forest densities are characterised by SEM and optical microscopy as shown in Figure 4.8. As the Fe layer thickness decreases from 4.5 nm to 0.5 nm the CNT forests become taller and more dense as confirmed by the reduced transparency of the active area in the optical images in the last row of Figure 4.8. The observed images in Figure 4.8 correspond to 3 min growth time achieving CNTs with heights of ∼20 µm in the case of 0.5 nm Fe and 12 µm when the Fe is 1.5 nm thick. However the presence of thick Fe layers cause the CNTs to grow in all directions resulting in a “spaghetti”-

like structure with a thickness of ∼500 nm to 1 µm as illustrated in the third column of Figure 4.8. In addition the devices fabricated with the optimised reflector have no delamination problems and can be used at temperatures as high as 800 °C.

Different growth times are characterised to obtain an approximate growth rate of the forests as shown by the SEM micrographs in Figure 4.9. A rate of approximately 3 µm/min is achieved with 0.5 nm Fe as illustrated in Figure 4.9 (a) whereas in the case of 1.5 nm Fe, a growth rate of ∼1 µm/min is obtained. With different growth times, the forest height can therefore be controlled to obtain the desired forest heights.

However as demonstrated in the magnified SEM images in Figure 4.9 (b), a catalyst thickness of 4.5 nm yields scattered and "spaghetti"-like CNT layers, whose heights are less than 1 µm although individual tubes can be much longer. The CNT structures are subsequently assessed by Raman spectroscopy using a 532 nm wavelength laser (InVia confocal Raman microscope, Renishaw plc, Gloucestershire, UK). Raman spectra are plotted in Figure 4.10 and demonstrate the increased presence of defects with higher Fe thicknesses. The G/D (G indicating the sp^2 hybridisation peak and D for defect caused by graphite oxide and sp^3 hybridisation) ratio increases from 0.84 to 1.1 as the Fe layer thickness decreases from 4.5 nm to 0.5 nm, indicating an improvement in the quality of CNTs. As there was no radial "breathing" mode (RBM) peak at 220 cm^{-1} (not shown in the Raman spectra) that indicates the presence of SWCNTs, it is concluded that the CNTs grown in this work are MWCNTs, and because the G peak is not substantially larger than the D peak, the CNTs have a higher sp^3 hybridisation compared to other related works.[61]

Devices fabricated with the CNTs on their active areas are then characterised in liquid by dropping 50 µL of DI water on top of the resonator by means of a micropipette. First, devices without CNTs are measured for comparison and the electrical responses are shown in Figure 4.11 (a) and Q spectra in Figure 4.11 (b). In the electrical impedance spectra, quasi-shear and quasi-longitudinal resonances are observed at 1.2 GHz and 1.8 GHz respectively. However the frequencies are relatively lower than predicted because of a thicker AlN layer than designed. Consequently a spurious mode caused by inefficient reflection is also observed at 1.5

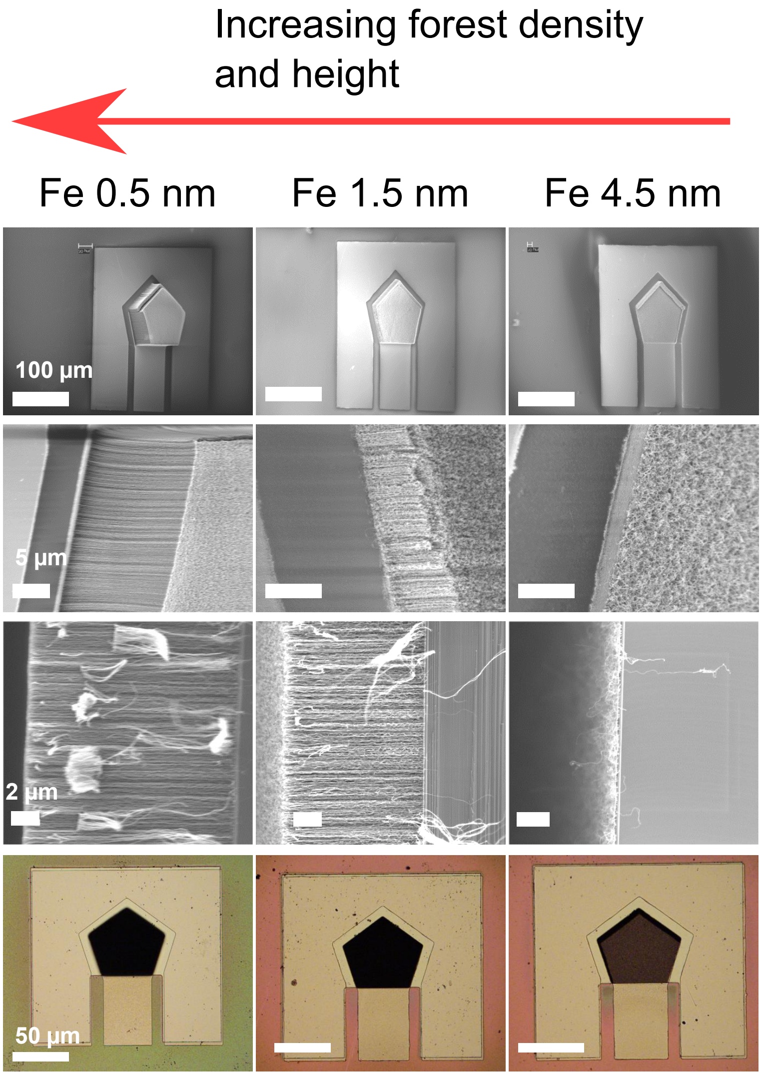

Figure 4.8: First row illustrates the SEM images of devices on which different densities and lengths have been grown with the 0.5 nm Fe giving the highest whereas 4.5 nm Fe gives the lowest density and height. The second row shows magnified images of the CNT grown on the active area confirming the higher tube density in the case of 0.5 nm Fe. The third row displays the cross-sectional cuts of the samples on to illustrate the thickness and spacing of the CNTs and their alignment with the 4.5 nm Fe giving randomly aligned CNTs. In the fourth row optical images of the devices are shown with a clear contrast of the CNTs grown with 0.5 nm Fe and 4.5 nm Fe as the height and density decrease substantially.

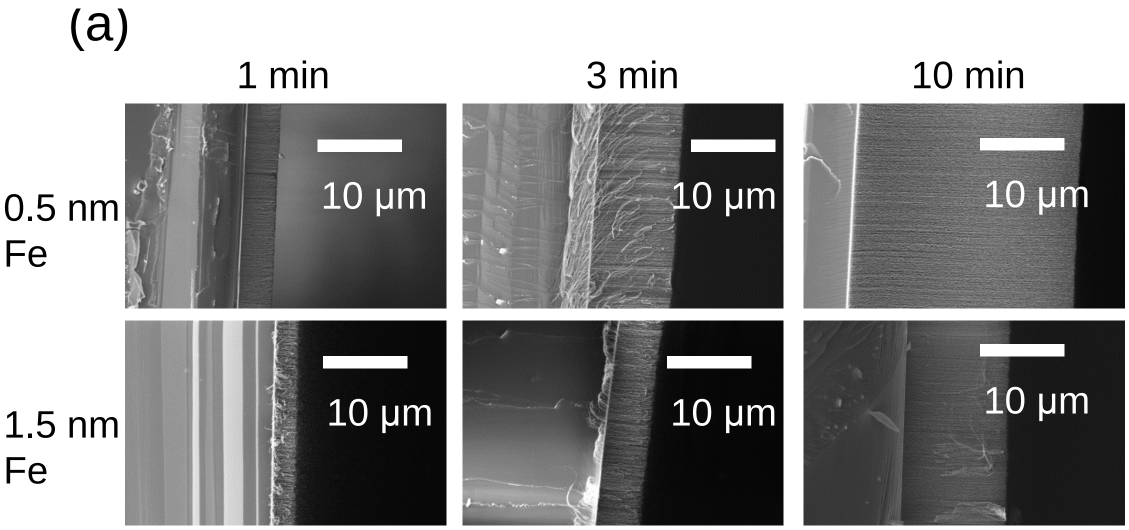

(b) Increasing magnification (growth for 3 mins)

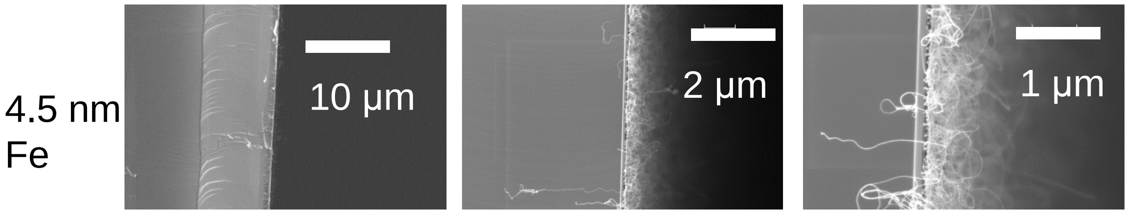

Figure 4.9: (a) Thickness variation with time for the densest CNT forest with Fe = 0.5 nm (forest height growth rate ∼3 μm/min) and medium density of Fe = 1.5 nm (forest height growth rate ∼1 μm/min). (b) When Fe = 4.5 nm, magnified images of the grown CNTs for a growth time of 3 mins, and the CNTs are "spaghetti"-like with thicknesses of less than 1 μm.

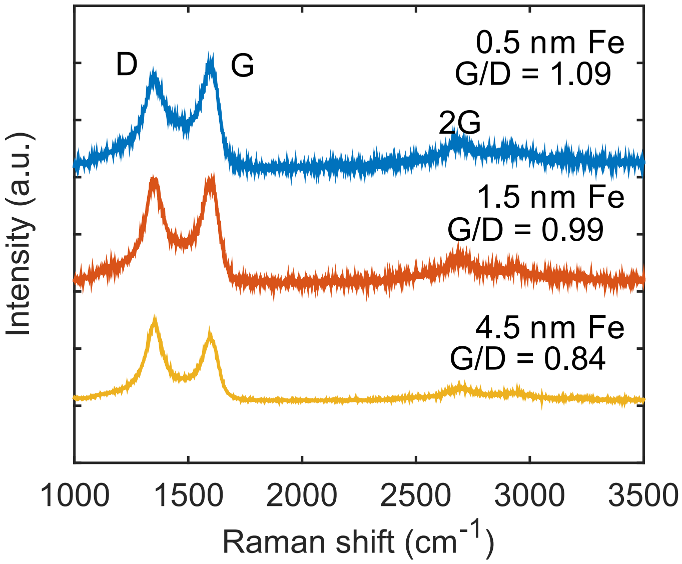

Figure 4.10: Normalised raman shifts of the CNTs with different densities grown on the SMRs, the G/D peak ratio decreases from 1.1 to 0.8 as the thickness of the Fe layer increases from 0.5 nm to 4.5 nm indicating an increase in the defect density in the tubes. G/D peak ratio was found to be ~1, it is deduced that the CNTs are multi-walled with sp^3 hybridisation.

GHz as the reflectors are designed for 2.2 GHz reflection for the longitudinal mode and with this thickness of AlN, a mode of 1.8 GHz is achieved. Adding DI water on the resonator causes a significant damping in the quasi-longitudinal mode as expected with a Q_r degradation of 99% (from 499 to 5). In contrast the quasi-shear resonance damps by ~53% when the Q_r drops from 260 to 120, and the shear mode is still present and can be used for sensing mass attachments.

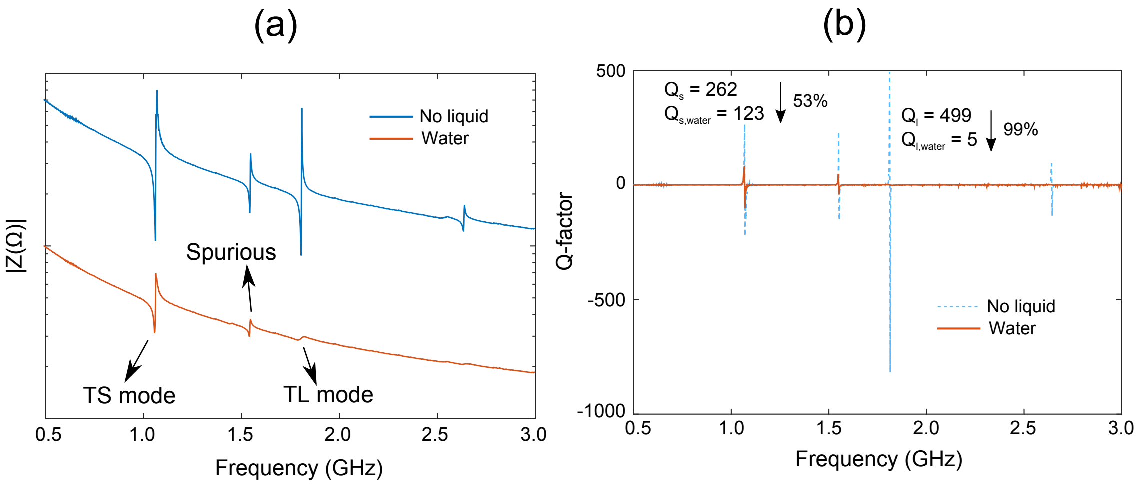

Figure 4.11: (a) Electrical impedance of normal devices in air (blue) and in liquid (red) (graphs displaced for clarity), demonstrating a shear (~1.2 GHz) and a longitudinal mode (~1.8 GHz). A spurious mode from the design of the reflector thicknesses is also observed at ~1.55 GHz. Both modes damp in water but the TSM damps by only 53% as shown in (b) whereas the TLM damps by 99%.

The same procedure is repeated with SMRs having CNTs on the active area. The electrical input impedance and Q spectra are illustrated in Figure 4.12 and Figure 4.13 respectively. Despite the presence of DI water the devices with CNTs grown on the active area still have an appreciable longitudinal mode as compared with devices without. Higher density and taller CNTs have both stronger shear and longitudinal modes, and as the density and height decrease the two modes become weaker.

The Q spectra indicate that the high density CNTs still have Q_r above 100 in DI water whereas this value reduces as the density and length of the CNTs decrease. A

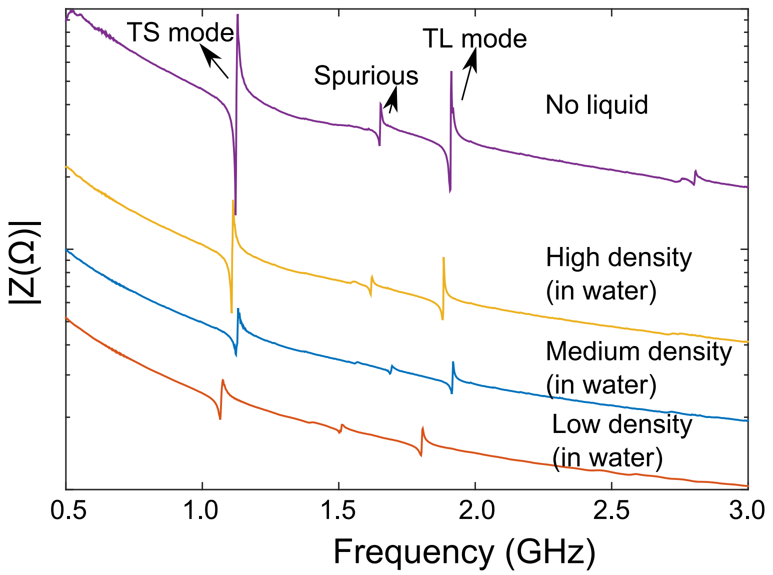

Figure 4.12: Electrical impedance of best devices with CNTs (purple) on the active area demonstrating that the longitudinal mode is still present in water in all cases (the high density CNTs (yellow) were ∼15 µm and the medium density tubes (blue) were ∼10 µm. The shear resonance is still affected but the damping is reduced. Graphs are displaced for clarity.

quantitative analysis demonstrates that Q_r damps by factors ranging between 50-70% in the case of the high density CNTs, 60-80% with medium density CNTs and 70-90% with “spaghetti”-like forests. This is a substantial improvement from the complete reduction of the longitudinal mode in the case without CNTs where Q_r is only 5, which renders mass attachment sensing impractical. The shear resonance is comparatively damped by a smaller proportion as expected, it achieves the best Q_r with the high density CNTs. However as the density and the length of the CNTs reduce, the shear mode Q damps significantly with almost 60-80% degradation. A possible reason is the attenuation of the wave by acoustic leakage through the CNTs caused by the proximity of the DI water with the resonator surface, which renders the CNT isolation layer ineffective. Therefore it is necessary to have a dense CNT forest and optimised height to limit the acoustic wave losses into the DI water, which consequently results in a high Q_r for the TLM.

After exposing the CNT forest grown with 0.5 nm Fe to a low vapour pressure solvent such as IPA and drying, the surface become more hydrophobic as shown in Figure 4.14 where the water droplet maintains its shape on contact with a densified CNT layer. The substrate is densified by using a wipe onto which IPA has been dropped, and gently placing the substrate upside down for 2 min. Upon evaporation of the IPA, the CNTs tend to bundle up into a denser layer, improving the hydrophobicity. For comparison, as illustrated in Figure 4.14, a CNT surface as grown from the CVD system is actually not entirely hydrophobic, and the water droplet spreads over the surface. This densification after rapid evaporation of the IPA is caused by its high surface tension that allows it to flow without assistance through the CNT forest.[188]

In order to understand the effect of the water on the resonator surface SEM is used to investigate the surfaces of the devices. Images before and after liquid are shown in Figure 4.15. A comparison before water (Figure 4.15 (a), (c)) and after water (Figure 4.15 (b), (d)) demonstrates that DI water penetrates inside the CNT forest to a certain extent and the alignment of the forest is maintained. This is necessary to avoid electrical shorts in the event the CNTs fall on the ground pads, which are ∼20 µm from the signal electrode. The penetration of the DI water to a certain extent through the forest is important to ensure that biomolecules attach to the CNTs rather than being completely isolated from the resonance if the liq-

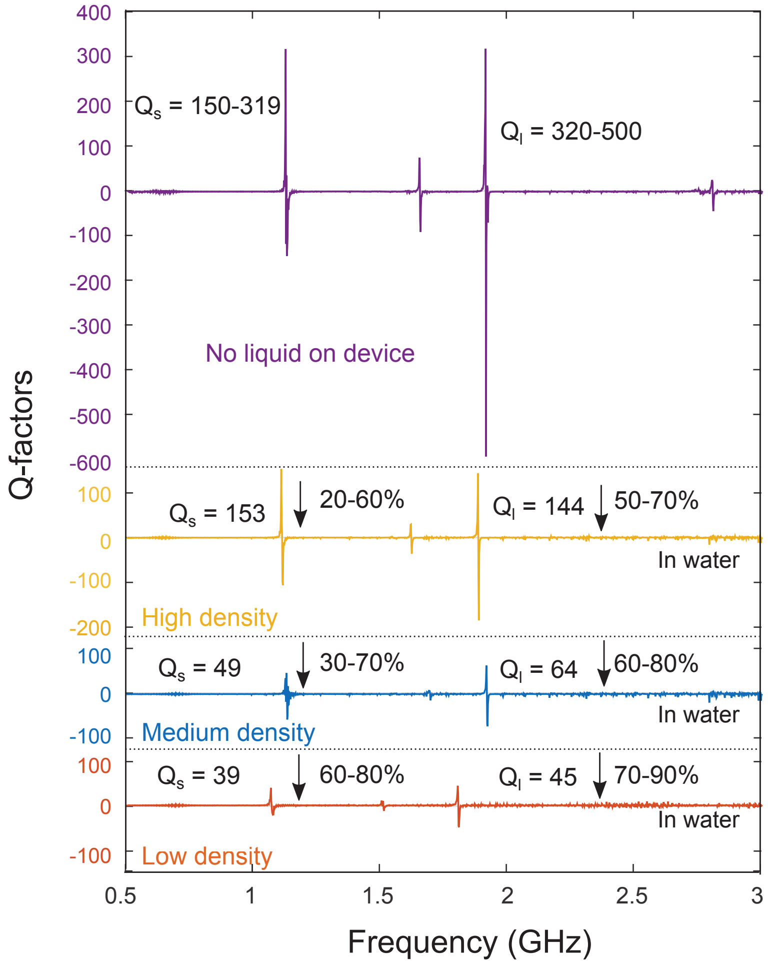

Figure 4.13: Q at resonance (positive values) of the devices obtained showing the the degradation by the presence of the liquid (yellow to red). The highest density CNTs (yellow line) still have high longitudinal mode Q_r in liquid and damps by only 50-70%; this degradation increases as the density decreases (from yellow to red) and the shear mode degradation is also increased.

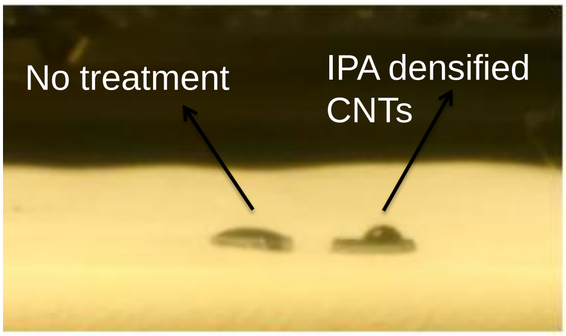

Figure 4.14: Picture of DI water droplets on CNTs as grown (left side) and after densification with IPA (right side), indicating that the CNT forest becomes more hydrophobic as the water does not spread over the surface.

uid droplet does not interact with the CNT forest surface, as is the case in purely hydrophobic layers.[189] The densified CNT forest on the resonators after IPA treatment are shown in Figure 4.15 (e) and (f). However this method can leave part of the resonator surface exposed to direct interaction with DI water as illustrated in Figure 4.15 (e). Furthermore densification of the surface can cause cause voids if the process is non-uniform as observed in Figure 4.15 (f), which eventually allows DI water to go through the forest thereby degrading the longitudinal mode Q_r by similar proportions as without the CNTs as shown in Figure 4.17.

Therefore the CNTs grown in this work are not entirely hydrophobic and can interact with biochemicals in water, which allows the transport and attachment of biological species while decoupling the resonant waves partially from the liquid as illustrated in Figure 4.16.

In addition to the Q_r degradation from 60% to 87% after IPA densified CNT surface, this process also cause a reduction of the longitudinal mode f_r as illustrated in Figure 4.17 (a), which can be due to the increase in the forest density that subsequently function as a bulk carbon layer on the surface. This solid layer eventually causes a larger propagation of the longitudinal mode into the CNT layer, and eventually into a liquid on top of this resonator, which explains the lower Q_r observed in these cases.

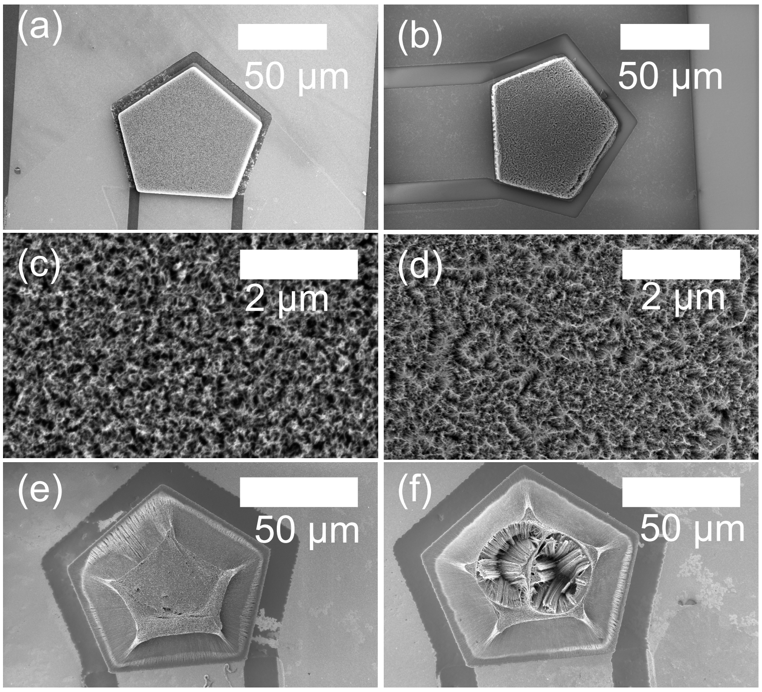

Figure 4.15: (a) CNTs on devices before water showing a vertically aligned tubes, (b) Effect of water on the device, the structure is still intact, (c) The surface of the CNTs before water (d) The surface after water droplet showing some liquid penetration through the tubes, (e) IPA treated CNTs with CNTs bundling up and densifying after IPA evaporation (f) Damage that can result from IPA treatment leaving holes for water to penetrate and deteriorate Q.

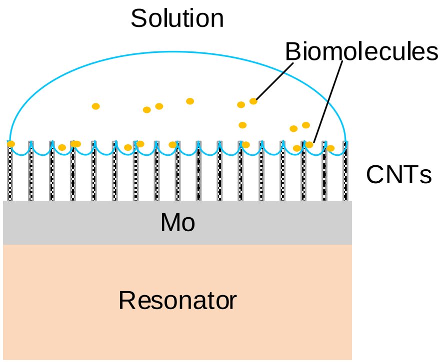

Figure 4.16: Schematic illustrating the attachment of biomolecules on the CNT wall with the liquid only penetrating through a distance short enough to maintain a longitudinal resonance.

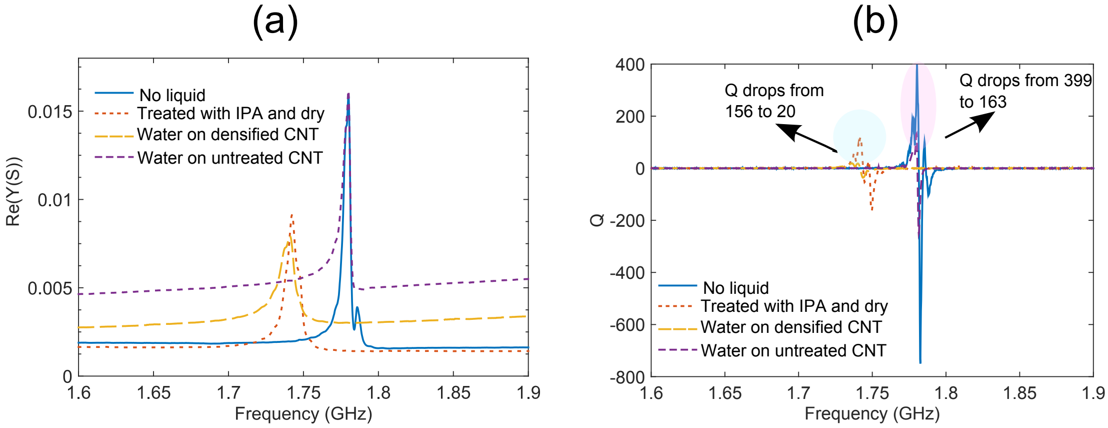

Figure 4.17: (a) Longitudinal mode spectra for IPA treated CNT forest with and without DI water droplet demonstrating that densifying the CNTs reduces the resonant frequency (b) Q calculated from the electro-acoustic responses, showing that the Q_r in DI water is worse (drop by 87% compared to 60%) after CNT densification.

4.4 Chapter conclusion

In summary, SMRs with CNTs grown on their active areas are fabricated and AlN is found to be a better piezoelectric material to support this growth at high temperatures as it is chemically stable. The CNTs provide an acoustic isolation for the longitudinal mode in DI water allowing Q_r comparable to the shear resonance, with the densest and tallest CNT forest providing the optimum isolation. The result is significant as this allows the use of the well-established longitudinal mode operation in liquid using CNTs as a high sensitivity and isolation layer, and to the best of our knowledge, it is the first time that a thickness longitudinal mode has been demonstrated to have a high Q_r in water despite the large volume of DI water above the active area. In Chapter 5 experiments to assess the sensitivity to mass loading of the highest forest density CNT layers will be described.

Chapter 5

Gravimetric sensor performance in air and liquid

In this chapter the application of the SMRs fabricated in Chapter 3 and Chapter 4 for sensors is demonstrated. Parameter extraction and tools used for the data analysis are explained in the first instance. The gravimetric principle of the shear resonance and its frequency shifts with different mass loads are assessed. Subsequently the frequency variations leading to variations acoustic velocities caused by temperature changes in the surrounding medium are also measured. In addition the performance of the shear mode in liquids of different viscosity and density products is evaluated before the viability of the devices as a functionalised sensor for antibodies is demonstrated. Finally experiments are carried out on the CNT isolation layer to investigate if the resonances are responsive to mass attachments. There are two types of measurements: a single frequency sweep using the network analyser where a file is stored for subsequent analysis and a continuous frequency tracking which is carried out with a real time link to the network analyser.

5.1 Experimental data analysis

Single sweep data obtained from the Agilent Technologies E5062A network analyser are handled by designing a graphical user interface (GUI) using MATLAB® (Figure 5.1). The GUI can be used to load both data files containing one-port parameters (S_{11}) and two port parameters (S_{11}, S_{12}, S_{22}, S_{21}) and can handle multiple files simultaneously, which is useful for frequency shift tracking by comparing multiple static measurements. Furthermore electromechanical performance parameters such as Q_r and Q_a, k^2_{eff}, f_r and f_a can be easily evaluated. This software also has the ability to export the plotted figures and the processed data into many different commonly used formats such as TIFF, EPS, PDF, JPEG, FIG and PNG.

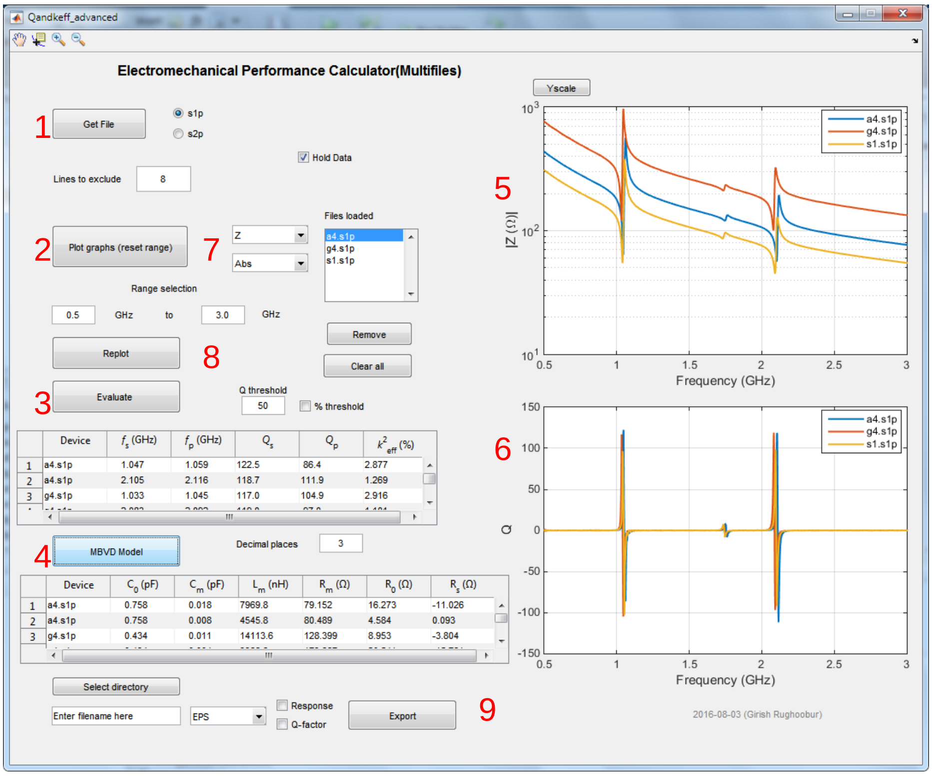

Qandkeff_advanced

Electromechanical Performance Calculator(Multifiles)

● s1p
○ s2p

☑ Hold Data

Lines to exclude: 8

Z
Abs

Files loaded:
a4.s1p
g4.s1p
s1.s1p

Range selection: 0.5 GHz to 3.0 GHz

Q threshold: 50
☐ % threshold

	Device	f_s (GHz)	f_p (GHz)	Q_s	Q_p	k^2_{eff} (%)
1	a4.s1p	1.047	1.059	122.5	86.4	2.877
2	a4.s1p	2.105	2.116	118.7	111.9	1.269
3	g4.s1p	1.033	1.045	117.0	104.9	2.916

Decimal places: 3

	Device	C_0 (pF)	C_m (pF)	L_m (nH)	R_m (Ω)	R_0 (Ω)	R_s (Ω)
1	a4.s1p	0.758	0.018	7969.8	79.152	16.273	-11.026
2	a4.s1p	0.758	0.008	4545.8	80.489	4.584	0.093
3	g4.s1p	0.434	0.011	14113.6	128.399	8.953	-3.804

Enter filename here
EPS
☐ Response
☐ Q-factor

2016-08-03 (Girish Rughoobur)

Figure 5.1: MATLAB® graphical user interface designed for calculating electromechanical parameters of measured resonators for both single port and two-port devices. The interface can plot all the variations of the measured electrical response and extract the electromechanical properties and mBVD model values.

In addition other characteristics of the software are its ability to provide mBVD equivalent resistor and capacitor values, which are good indications of the origin of losses in resonators, and the optimisation necessary to improve the performance of the devices. The spectra can also be narrowed around the region of interest to determine the peaks and Q in detail or to observe interferences such as laterally travelling waves that are common with membrane type resonators. Peak determination in the Z and Q spectra is achieved by the `findpeaks` function in MATLAB®. The software has been a useful tool in this thesis especially to have a rapid electromechanical performance calculator that can output different parameters without the need to handle complex equations for each device.

The data file (usually .s1p or .s2p) is loaded by the "Get file" button (marked by 1 in Figure 5.1) and plotted (2). A selection containing Z, Y, and the S-parameters are available (7) with different outputs such as real part, imaginary part, absolute value or the phase (7). Different thresholds in Q for the evaluation (3) can be set (8) to avoid incorrect calculations, since the parameters are obtained using the peak determination algorithm in MATLAB® on the Z spectra. For resonators with large Q, a larger threshold needs to be set whereas a lower threshold for resonators with lower Q. A threshold of $\sim$20% of the maximum Q is found to give precise electromechanical parameters. Values of k^2_{eff} are obtained by using the peaks obtained and equation (2.7) and the threshold of Q is necessary in this part as erroneous peaks can lead to exaggerated k^2_{eff} values.

5.2 Resonant frequency tracking

For real-time measurements, the MATLAB® interface in the section 5.1 is not able to acquire data and process simultaneously; therefore a LABVIEW® automation software (Figure 5.2) is designed based on a similar interface designed by Prof. Enrique Iborra from the Polytechnic University of Madrid. A connection to the network analyser is first established with a general purpose information bus (GPIB) and the initial response of the device is acquired in real-time and processed to obtain Re (Y), the magnitude of Z and the evaluated Q. The acquisition bandwidth can be tuned to decrease the response time of the software and hence obtain data continuously (within a few milliseconds). In a second step, the spectrum is narrowed (around 200 MHz bandwidth) around the resonance as shown in Figure 5.3 (a) (the region where a peak in Y is observed) of interest to obtain a curve that can be fitted with a polynomial. Alternatively this can be discarded and only the maximum of the real part of Y can be tracked. After selecting the region of interest, the response is fitted with a curve simultaneously while tracking the frequency where

Re (Y) occurs. Depending on the quality of the fit and the roots of a polynomial fit (normally a polynomial order from 5 to 8 to have low residues) are adjusted to determine the frequency of the fitted Re (Y). f_r is obtained by determining the root that is located in the narrowed frequency response. As observed in Figure 5.3 (b), this method reduces the noise significantly in the resonant frequency plot (red line).

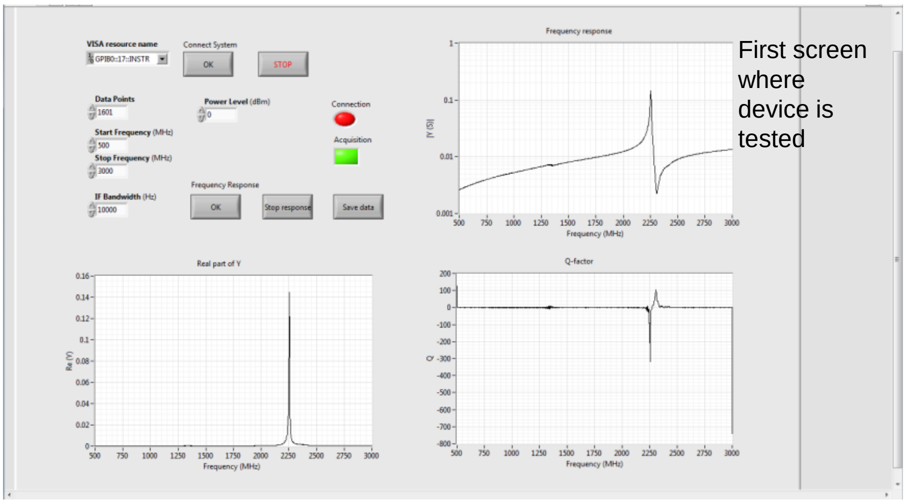

VISA resource name: GPIB0::17::INSTR

Data Points: 1601

Start Frequency (MHz): 500

Stop Frequency (MHz): 3000

IF Bandwidth (Hz): 10000

Power Level (dBm): 0

First screen where device is tested

Figure 5.2: LABVIEW® interface showing the main screen in where the initial response of the device is obtained with plots for Z, Y and the Q. Start and stop frequencies can be changed and the acquisition bandwidth can be adjusted to reduce the response time. Responses can also be saved as s1p files for reference.

In addition the progress of the Q with time is also evaluated (Figure 5.3 (c)), which is necessary when liquids of different viscosities are used. This LABVIEW® program is a state machine implementation allowing easy switching between the frequency response part and the frequency tracking page. However at present the software is only able to track a single frequency at a time. A future implementation will include the possibility of segmenting the data points around 2 regions of interest (for example a TSM and a TLM) and tracking the maximum of Y in each region simultaneously. Such a software will also allow tracking Δf_r of dual-mode resonators and hence mass loading and temperature, viscosity or pressure in parallel.

(a) First screen where response is narrowed to resonance

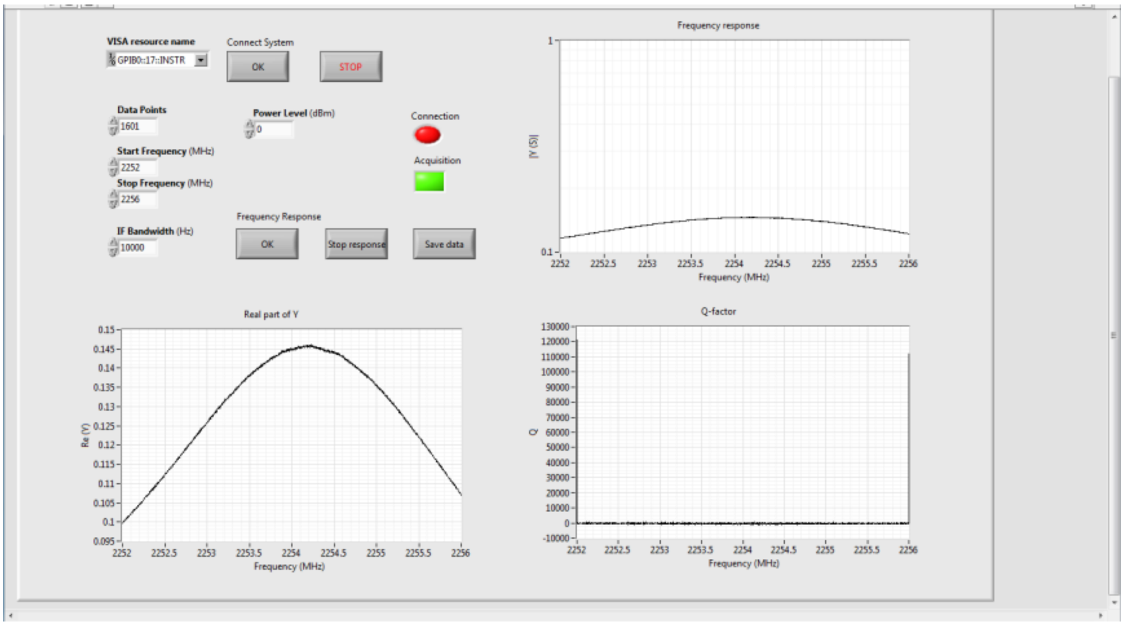

VISA resource name: GPIB0::17::INSTR

Data Points: 1601

Power Level (dBm): 0

Start Frequency (MHz): 2252

Stop Frequency (MHz): 2256

IF Bandwidth (Hz): 10000

(b) Last screen where response is fitted and frequency is tracked

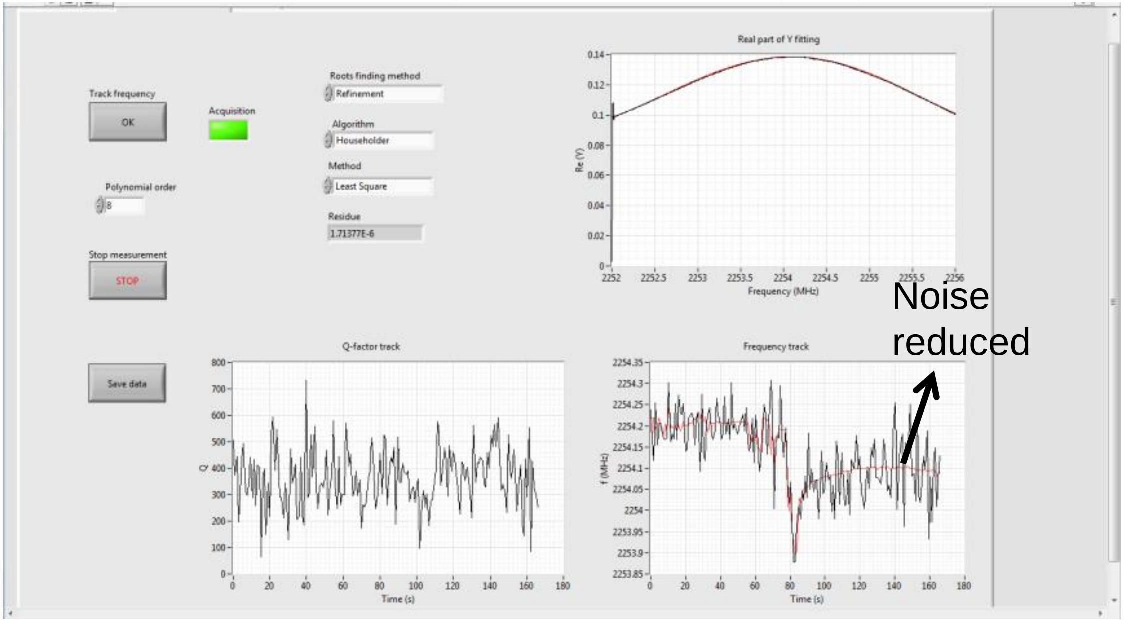

Roots finding method: Refinement

Algorithm: Householder

Method: Least Square

Residue: 1.71377E-6

Polynomial order: 8

Figure 5.3: Interface where the spectrum can be narrowed down to the resonance point to obtain a curve that can fit a polynomial function in (a). After obtaining the narrow response, the user can proceed to the frequency tracking screen (b) where different algorithms can be used to fit with different polynomial orders. The Q at resonance and the maximum of the real part of Y are also tracked simultaneously but the fitting reduces the noise in the signal.

5.3 Mass sensing

The S_m value of the shear mode SMRs from section 3.2 is calibrated by the thermal evaporation of thin films of Al on patterned active areas of the resonator. In this work the thickness of the evaporated Al is determined by a calibrated thickness monitor to obtain a precise mass of the coated layer on the active area. Before this evaporation the Z spectra of the devices are measured to obtain the original f_r. The measurement is repeated after the evaporation to obtain Δf_r. Mass attachment caused by the deposition of the Al reduces the shear mode f_r as shown in Figure 5.4.

Table 5.1: Mass and surface mass density of loaded resonator for different Al thicknesses

t (nm)	f_r (GHz)	m (ng)	m/A (µg/cm^2)
4.0	1.075	0.154	1.080
8.0	1.070	0.308	2.160
12.0	1.064	0.462	3.240
16.0	1.057	0.615	4.320

The added mass on the resonator surface is calculated using:

$$m = \rho A t \tag{5.1}$$

where ρ is the density of Al, A is the active area ($A = 1.42 \times 10^{-4}$ cm^2) for the designed pentagons), and t is the thickness of the Al. Table 5.1 is a summary of the different mass surface density added on the SMRs for different Al thickness. The value of S_m for the shear mode SMRs resonating at ~1.1 GHz is calculated using equation (2.57) from Chapter 2 to be (4.95 ± 0.08) kHz·cm^2/ng, which is sufficiently high for biological detections.[187] In comparison TLM SMRs have higher S_m ($\approx$ 12.3 kHz·cm^2/ng) with thin Al layers due to their higher f_r.[65] Considering a minimum detectable frequency of 1 kHz at a resonant frequency of 1 GHz [52], m_r is calculated as (0.202 ± 0.003) ng/cm^2, and m_{min} is therefore (29.3 ± 0.4) fg. Nonetheless the oxidation of the Al and added mass have not been considered in Δm, which can occur when the the device is heated in air. Assuming ~3 nm of

Al_2O_3 ($\rho = 3.95$ g/cm^3) for each thickness on the surface [190], the value of S_m is then reduced to 4.86 kHz·cm^2/ng.

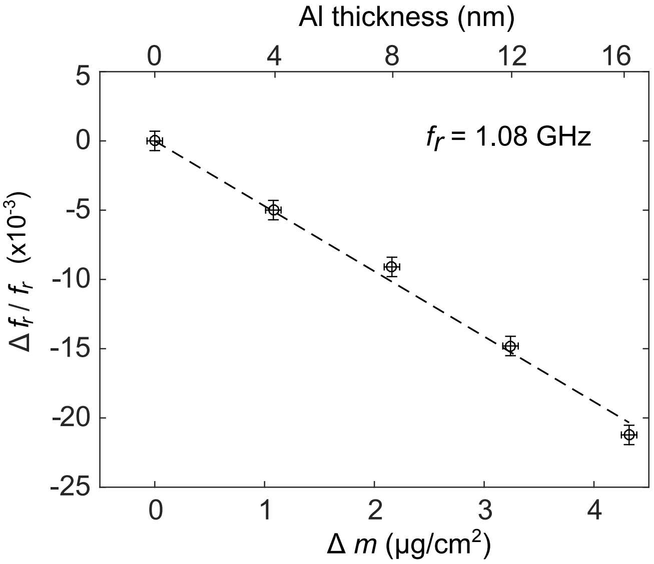

Figure 5.4: Mass sensitivity calibration by the deposition of known thicknesses of Al on the resonator surface area, $S_m = 4.95$ kHz·cm^2/ng.

5.4 Temperature sensing

To evaluate the TCF of the shear resonance, the SMRs are placed on a temperature controlled hotplate and heated while measuring the electrical impedance. After 10 mins between each temperature step to allow for the temperature, T, to stabilise, the spectra are recorded and the shear mode f_r is determined from the maximum of $\mathrm{Re}(Y(S))$. This is shown in Figure 5.5 where a reduction in f_r is observed with ΔT, which is the shift in the hotplate temperature from RT. The measurement errors are estimated by assuming that the temperature on the hotplate is ± 2 °C from the actual set-point.

A TCF value of $-(66 \pm 2)$ ppm/K is extracted from a linear fit of the graph in Figure 5.5, which was close to the value (-63 ppm/K) reported elsewhere.[53] Nonetheless this large TCF should be reduced to ensure positive detection of biomolecules. This can be achieved by tuning the the reflector layer materials and properties by

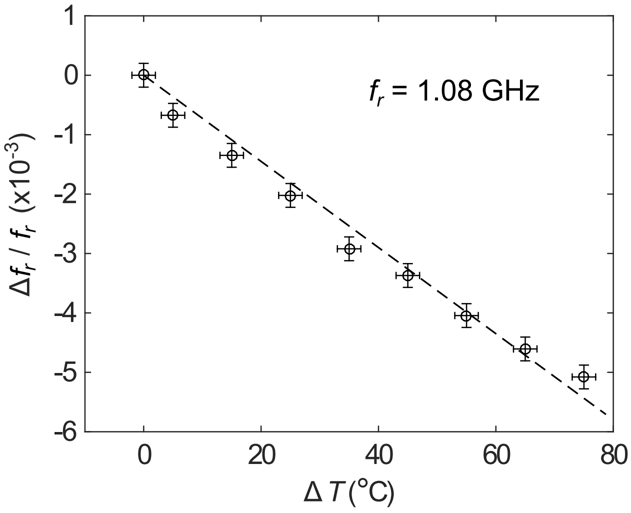

Figure 5.5: Temperature dependence of the shear mode f_r measured for different temperaures ranging from 20 °C to 100 °C.

adjusting the deposition conditions to compensate for the high intrinsic temperature sensitivity of the ZnO sound velocity.[136] However this TCF value can also be useful for monitoring T using both the shear and longitudinal mode using a dual-mode concept as explained in [117, 118]. The shear mode f_r of the SMR decreases because of the decrease in the acoustic velocities of the materials in the structure including the porous SiO_2 in the reflector stack, which also has a negative TCF.[191]

5.5 Viscosity sensing

In this section, the viability of the shear mode SMRs as a viscosity sensor is assessed. Mixtures of different ethanol (EtOH) and DI water compositions ranging from 0-100% are dropped in 50 µL volumes on top of the sensor active area by means of a micropipette and Δf_r for each composition is measured. The values for η and ρ of different water-EtOH compositions are obtained from Khattab *et al.* [192]. These are summarised in Table 5.2 and the product, $(\eta\rho)^{0.5}$, is plotted in Figure 5.7 (a) against the percentage of EtOH in DI water. Water-EtOH mixtures having different η and ρ cause a shift of the shear mode f_r as shown in Figure 5.7 (b), where a linear fit with the product $(\eta\rho)^{0.5}$ is achieved, as proposed by the Kanazawa and Gordon model.[138] This range of $(\eta\rho)^{0.5}$ is suitable for determining the viscosity sensitivity

Table 5.2: Viscosity and density of different water-EtOH compositions obtained from [192]

Percentage of EtOH (%)	ρ (g/cm^3)	η (Pa·s)	$(\eta\rho)^{0.5}$ (g/{cm^2·s$^{0.5}$})
0	1.000	1.003	1.002
10	0.979	2.004	1.401
20	0.958	2.655	1.595
50	0.895	2.787	1.579
80	0.832	1.837	1.236
90	0.811	1.500	1.103
100	0.790	1.190	0.969

because with higher viscosity solutions (> 1000 mPa·s), a divergence from this linear dependence occurs as the liquid cannot be assumed to be Newtonian.[105] From the measurements, a viscosity sensitivity, S_v of (-1860 ± 40) ppm/(g/{cm^2·s$^{0.5}$}) is calculated. In DI water, Q_r decreased by 60% (from 159 to 65), while in EtOH, Q_r reduced by 42% (from 159 to 92) as shown in Figure 5.6.

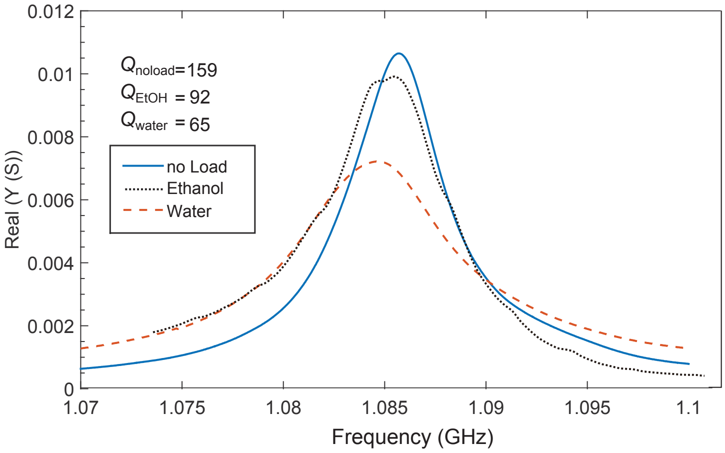

Figure 5.6: Effect of water and ethanol on the thickness shear mode resonance showing a reduction in the Q_r from 159 to 92 in ethanol and 65 in water. Dotted black line corresponds to EtOH, dashed red line to water and solid blue line to device without liquid.

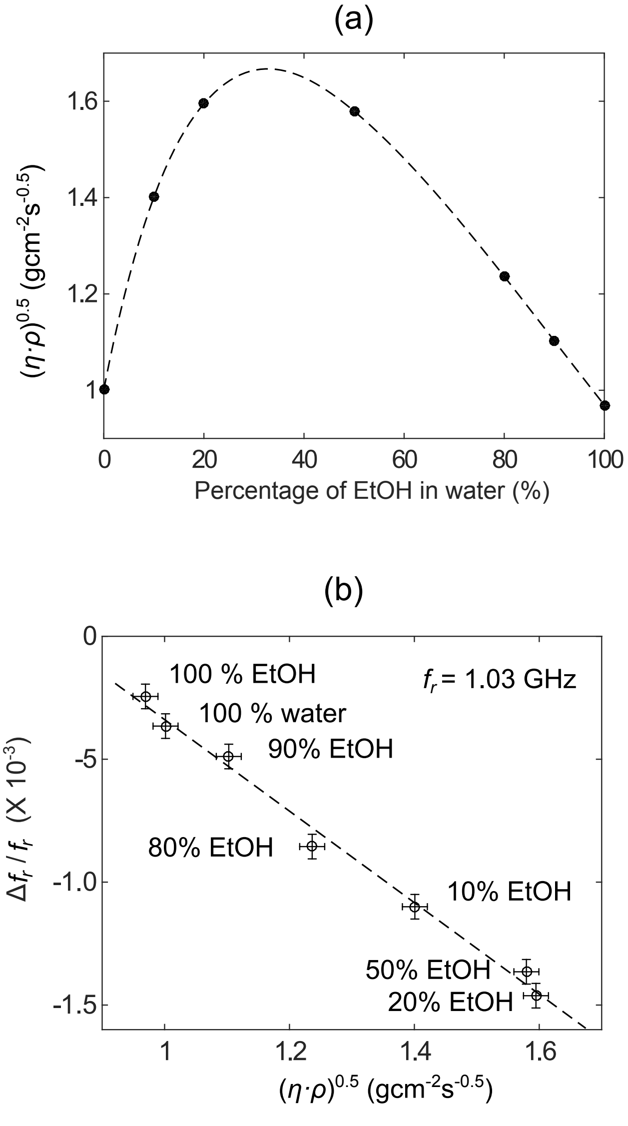

Figure 5.7: (a) A plot of the variation of the product $(\eta\rho)^{0.5}$ with different percentages of ethanol in water with data for the viscosity obtained from literature[192]. (b) shows that the Kanazawa and Gordon prediction that the shear resonance Δf_r decreases linearly with the product of $(\eta\rho)^{0.5}$, the different values of EtOH-water % are listed next to the points.

5.6 In-liquid biosensing with antibodies

To functionalise and assess the performance of the SMRs for in-liquid biosensors, the active areas are patterned by standard UV photolithography with Microposit S1818 photoresist and a thin layer (~50 nm) of SiO_2 is deposited by RF magnetron sputtering on this patterned region before lift-off. This deposition is carried out using the same recipe in section 3.1.1. This active area is then functionalised using a standard (3-Aminopropyl) triethoxysilane (APTES) - glutaraldehyde (GA) functionalisation protocol as shown in Figure 5.8.[187, 193] This functionalisation process is performed with the help of Dr. José-Miguel Escolano and Prof. Enrique Iborra from the Polytechnic University of Madrid. In the first step (labelled as 1 in Figure 5.8) the resonator is treated with capacitively coupled O_2 plasma at 13.3 Pa for 2 mins to generate OH groups on SiO_2. In a second step, the resonator is incubated in a solution of APTES 2% (Sigma-Aldrich) in absolute EtOH for 10 mins at RT. The surface is washed with absolute EtOH, dried with N_2 and cured in air at 110 °C in an oven during 1 hour. Subsequently the resonator is immersed in glutaraldehyde (GA) 1% (Sigma-Aldrich) for 1 hour at RT to bind the GA to the silane. The ultimate aim of the functionalisation process is to cover the entire active area of the resonator with streptavidin as receptor for the biotin marked antibody that needs to be detected. The device is incubated in streptavidin 10 µg/ml (purchased from Sigma-Aldrich) in 50 mM NaCl for 1 hour at RT. To block the free aldehyde groups, the device is incubated for 1 hour at RT with Bovine Serum Albumin (BSA) 1% (from Sigma-Aldrich) in 50 mM NaCl. Finally the device is incubated with the Binding Buffer (PBS pH 7.4, BSA 0.1%, Tween-20 0.05%) for 30 min at RT. The molecule chosen to measure the binding to the biosensor surface is Rabbit Immunoglobin-G (IgG) whole molecule which is biotin conjugated (ab7074 purchased from Abcam). This antibody with concentration of 135 nM (a concentration enough to saturate the active area of the resonator) is incubated in a Binding Buffer recirculating with a peristaltic pump, which is connected to a flow cell sealed around the SMR under measurement. The Δf_r is tracked using a LABVIEW® software (section 5.2) to monitor the attachment of the antibody to the functionalised resonator surface as a function of time.

The viability of the device for in-liquid sensing is carried out using the struc-

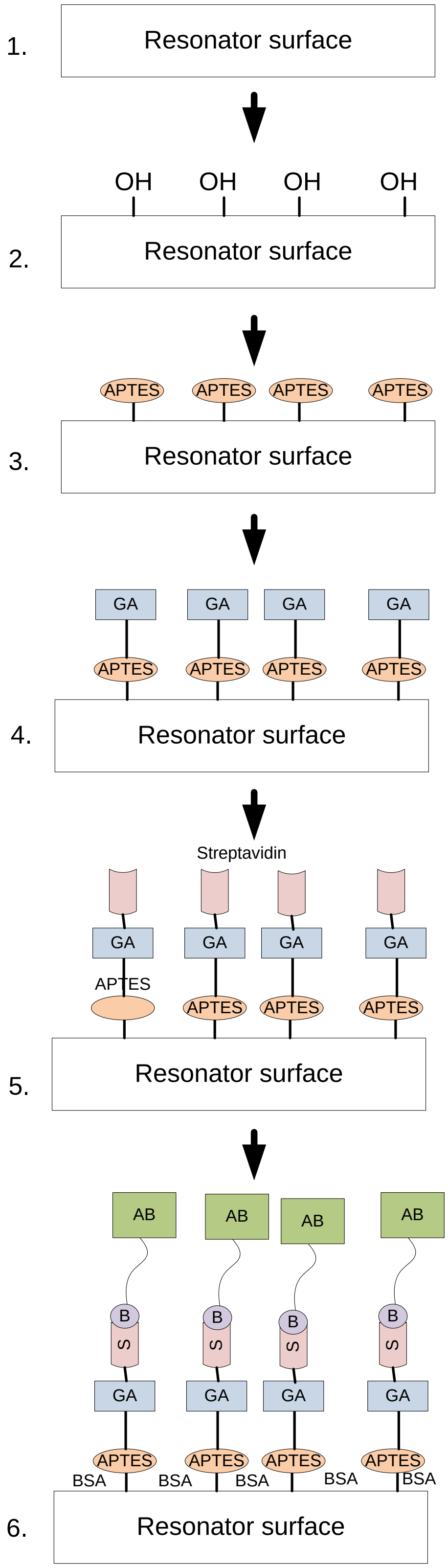

Figure 5.8: Functionalisation steps involved in detecting the antibody identified by the step numbers 1-6 on the resonator surface.

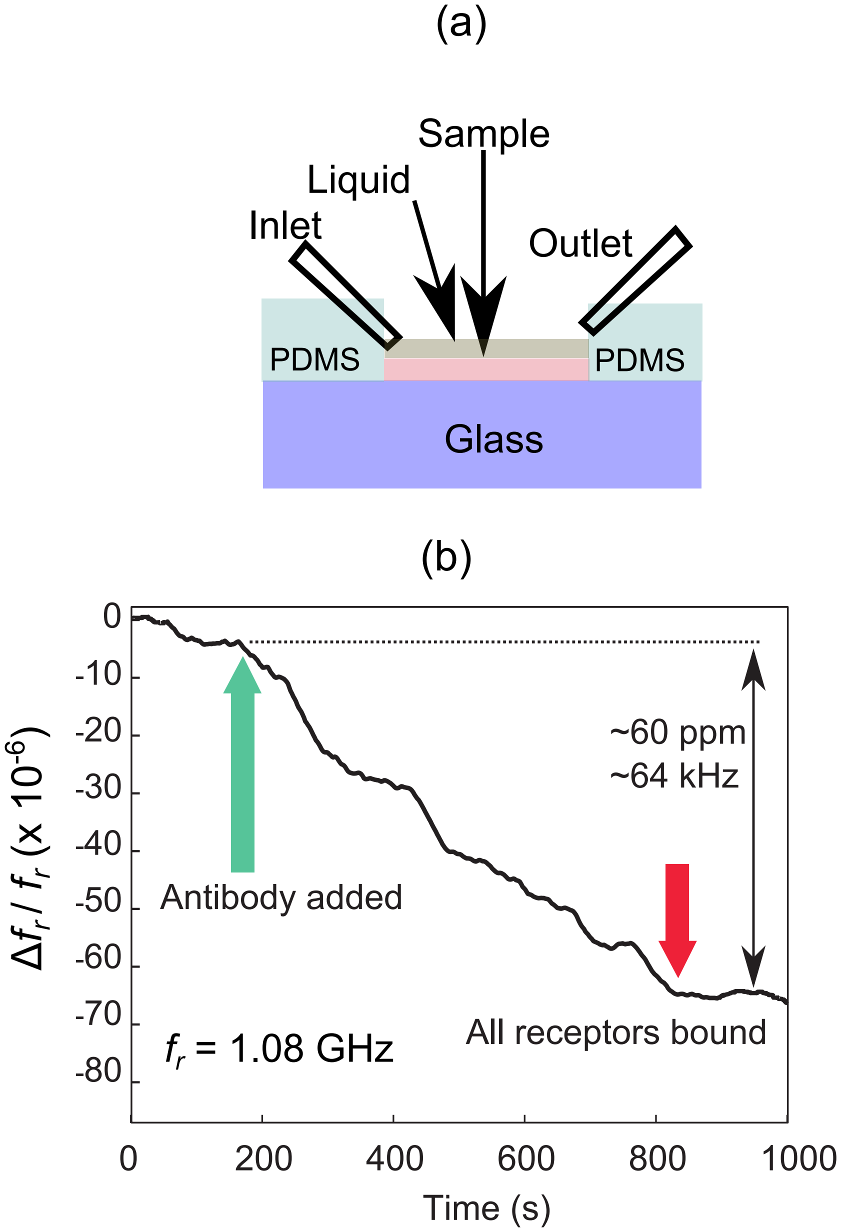

Figure 5.9: (a) Schematic of the inlet and outlet water flow on the substrate held in place by PDMS on a glass slide for the biosensing measurement in liquid. (b)Detection of antibodies in-liquid using the shear resonance of a functionalised device, detection is complete in 600 s. The signal is first stabilised for ∼100 s, after which the antibody is injected in the fluidic arrangement while monitoring the resonant frequency. As the antibodies bind to the recepors of the device, the resonant frequency drops until a stable signal is obtained. A shift of ∼64 kHz is achieved based on the relative shift of -60 ppm at f_r of 1.08 GHz.

ture illustrated in Figure 5.9 (a). After 200 s of stabilisation (±5 kHz) of f_r by recirculating Binding Buffer, the biotin conjugated Rabbit IgG is added to the flow, which caused a Δf_r of approximately -64 kHz as shown in Figure 5.9 (b). All streptavidin receptors are blocked after ~600 s, after which there is no further decrease in f_r. This Δf_r corresponds to a mass surface density of 1.3 ng/cm^2 of the biotin conjugated Rabbit IgG by using the value of S_m from section 5.3 and equation (2.57). The binding of the biotin conjugated antibodies to the streptavidin receptors is completed in a longer time (~600 s) than reported elsewhere: the time to saturate the functionalised surface depends on the microfluidic arrangement and in this case an open system is used.[187] During the biosensing experiments, it is also observed that the ZnO gradually reacts with the buffers, and after long immersion in liquids the surfaces are etched away due to its porous morphology and reaction with chemicals in the buffers. A passivation layer with either SiO_2 or Si_3N_4 is therefore necessary to protect the exposed ZnO layer if such devices are to be used for in-liquid measurements.

5.7 CNTs for in-liquid sensing

In this section, initial experiments carried out using high density CNTs on the active area with a forest height of ~15 µm for in-liquid mass sensing are demonstrated. Devices fabricated in section 4.3 are considered in this section, BSA is chosen as it is water soluble and adsorbs easily on the CNTs.[194, 195] BSA dissolved in water with a concentration of 20 mg/mL is obtained from Sigma Aldrich, which is then diluted into 3 different concentrations ranging from 50 µg/mL, 1000 µg/mL and 2500 µg/mL. The compositions of the solutions from the base BSA concentration is shown in Table 5.3.

Table 5.3: Volumes of BSA solution from the 20 mg/mL base to prepare 3 different concentrations for testing

BSA concentration (mg/mL)	BSA volume (µL)	DI water (mL)
0.05	10	3.99
1.00	200	3.80
2.50	500	3.50

The SMR with CNTs is measured with a droplet of DI water initially and the spectra for the shear and longitudinal modes are recorded. A volume of ∼50 µL is dropped by means of a micropipette. After allowing the device to dry in air, a similar volume (50 µL) of the prepared BSA solution is dropped on SMRs under measurement, and allowed to bind for 5 mins before recording the measurement. The process is repeated for each BSA concentration and the spectra are analysed with the GUI from section 5.1.

Figure 5.10 illustrates the real part of the electrical admittance, Y, for each concentration with the shear mode in Figure 5.10 (a) and the longitudinal mode in Figure 5.10 (b). Clear Δf_r are observed in the longitudinal mode of the devices, and the attachment of the BSA on the CNTs increases with concentration as there are more BSA in the solution, leading to a decrease in the longitudinal mode f_r as demonstrated by the blue curve in Figure 5.11. However the shear mode Δf_r are smaller compared to the longitudinal mode as shown in the inset of Figure 5.10 (a) and Figure 5.11. This can be attributed to the low Poisson's ratio of MWCNTs [196]; and accordingly the shear wave does not propagate efficiently through the thick forest. In addition individual tubes are mainly held by van der waal's forces and the transverse vibrational mode decays rapidly across the forest.[197]

The graphs in Figure 5.11 reach a plateau after a BSA concentration of approximately 1 mg/mL because the concentration saturates the CNTs; the binding sites on the CNTs are completely occupied, leading to a lower shift (< 50 ppm) in f_r at higher concentrations. With the Δf_r at 1 mg/mL of BSA in water, the longitudinal S_m ($\Delta f_r/f_r \approx -280$ ppm) can be estimated to be ∼7 times higher than the shear mode ($\Delta f_r/f_r \approx -40$ ppm) by the presence of the high density CNT forest. From the results in this section, it is deduced that the resonator with vertically aligned CNTs, which achieves a longitudinal mode Q_r of ∼95 in water, can be used for in-liquid biosensing measurements. In addition it is shown that the longitudinal mode has a higher S_m than the shear mode in the devices isolated by the CNT layer, which is a significant outcome of this work.

Yet with the addition of BSA solutions (even at the saturation concentration of 2.5 mg/mL) on top of taller CNT forests (∼30 µm), there are no significant changes to the f_r and Q as illustrated by the electro-acoustic responses in Figure 5.12.

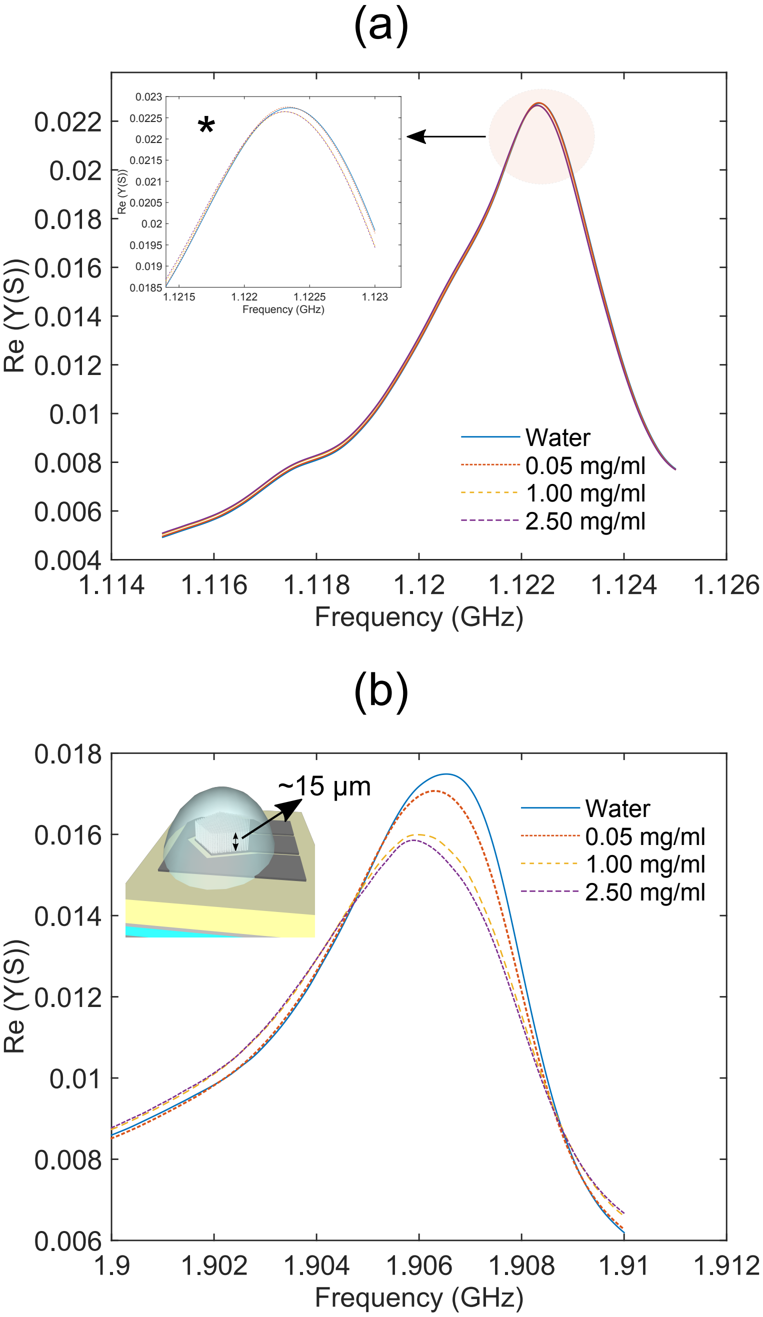

Figure 5.10: (a) Effect on the shear mode by different BSA concentrations (inset is a magnified spectrum near resonance) (b) Longitudinal mode f_r decreases as BSA concentration increases indicating mass binding is still detected with VACNTs of ∼15 µm in height.

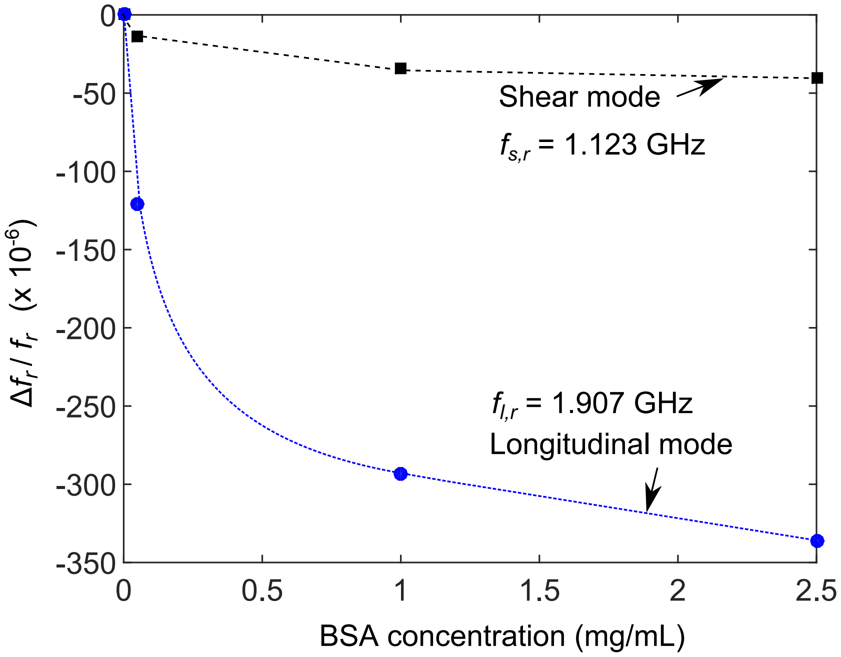

Figure 5.11: Graph showing of the effect on the relative frequency shifts for the shear and longitudinal modes with different BSA concentrations. Dashed lines are guides for the eye. The longitudinal mode (blue line) has a larger shift compared to the shear mode (dark line). A saturation point is reached at high concentrations.

High $Q_r > 200$ are obtained in both the TSM (Figure 5.12 (c)) and the TLM (Figure 5.12 (d)) despite the presence of the high concentration BSA solution on top of the resonators. The results indicate a tall forest becomes hermetic and to the liquid, which consequently yields the highest Q_r.

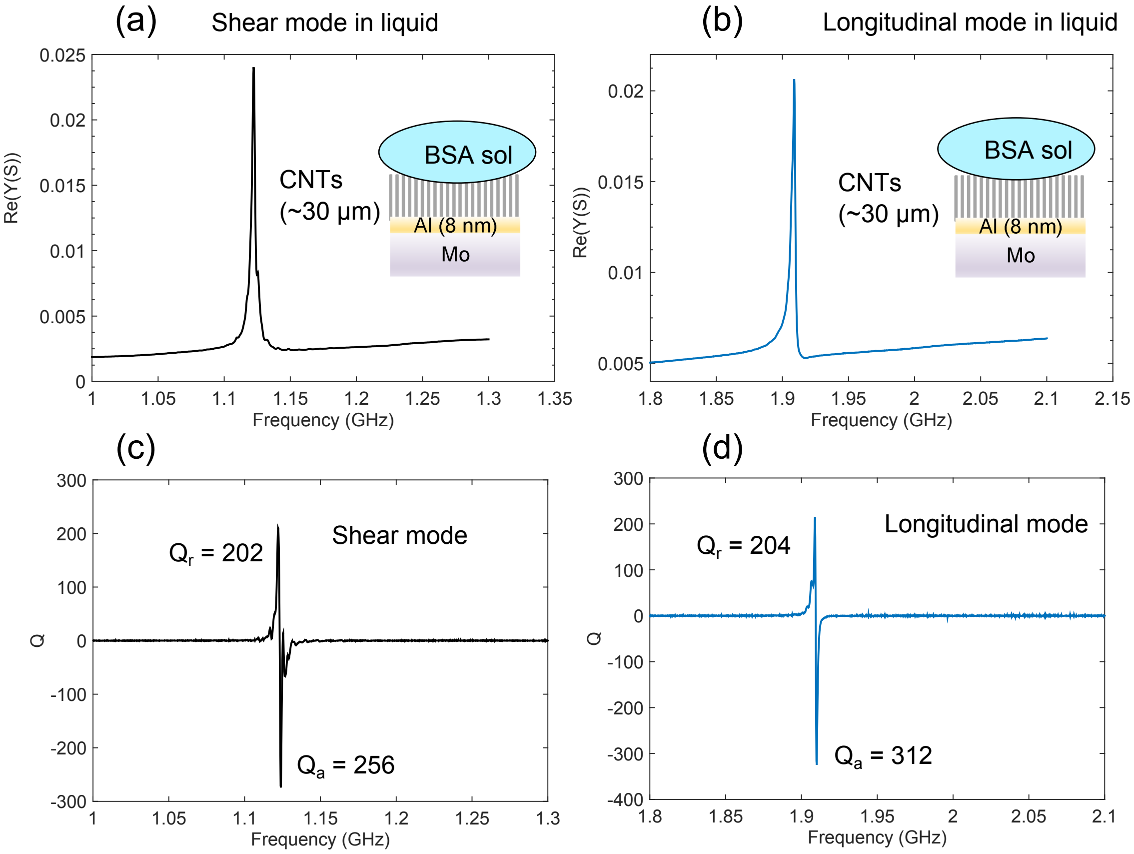

Figure 5.12: Plots showing the performance of tall (∼30 µm) VACNTs in a solution of 2.5 mg/mL of BSA solution on $Y(S)$ of the shear mode ($f_S = 1.12$ GHz) in (a), the longitudinal mode ($f_L = 1.9$ GHz) in (b) and the Q at resonance (202) and anti-resonance (256)) in (c) for the shear mode and the longitudinal mode ($Q_r = 204$ and $Q_a = 312$) in (d).

Inspite of the improved Q_r of the resonant modes in the BSA solution, significant f_r shifts due to mass attachment are not observed, as shown in Figure 5.13. Although a trend is evident as time progresses after dropping the 2.5 mg/mL BSA solution, the Δf_r are almost two orders (10^{-6} for taller CNTs compared to 10^{-4} for 15 µm heights) of magnitude lower than in the case for a lower Q_r (∼95 with ∼15 µm

CNTs) resonator in liquid. The positive Δf_r in the case of the longitudinal mode can be caused by temperature drift due to evaporation of the BSA solution from the surface of the resonator, leading to surface cooling of the resonator. Nonetheless both the TSM and TLM shift by only a few kHz, which is just above the noise floor for frequency regimes higher than 1 GHz. In addition the concentration of the BSA solution is high enough to saturate the CNT forest of ~15 µm as demonstrated earlier in this section.

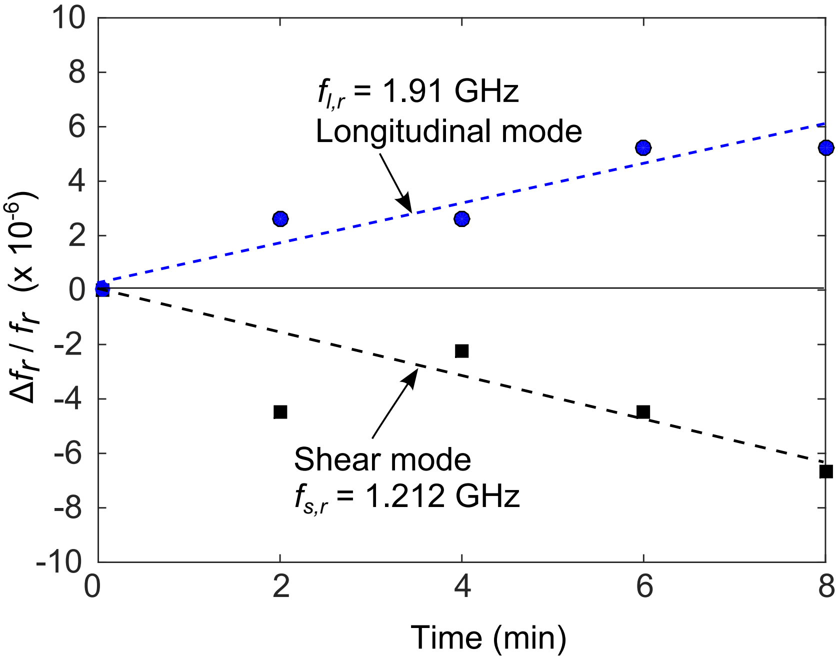

Figure 5.13: The relative frequency shifts for the shear and longitudinal modes with time for a resonator with highest longitudinal mode Q_r (~200) achieved in liquid using VACNTs of ~30 µm in height. Dashed lines are guides for the eye. The longitudinal mode (blue line) has a positive shift compared to the shear mode (dark line) and the $\Delta f_r/f_r$ are smaller (100 times less) than with a resonator with lower Q_r (~95) in liquid.

5.8 Prostrate specific antigen (PSA) detection in air with longitudinal mode SMR

In this section the initial results using a longitudinal mode in air to detect PSA biomarker for early prostrate cancer diagnosis are discussed. The functionalisation of the surface and biomarker attachment are carried out by Dr. Ewelina Wajs using the protocol described in [198]. SMRs with a ZnO layer having a thickness longitudinal mode at 2.5 GHz are fabricated for the biosensing experiment in this section. After deposition of the top Mo electrode layer, a thin Au/Cr (20 nm/4 nm) layer is evaporated thermally, as Au surfaces are easier to functionalise. The Au surface is first cleaned in O_2 plasma by RIE for 1 min with a forward power of 50 W, 40 sccm O_2 gas flow and 25 Pa process pressure. The functionalisation protocol is schematically shown in Figure 5.14.

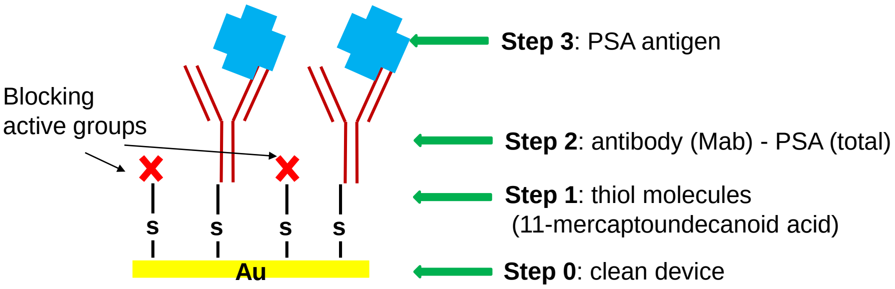

Figure 5.14: Schematic illustrating the surface functionalisation steps in the PSA detection on an Au coated SMR resonator.

Ethanolic solution of 11-mercaptoundecanoid acid is prepared to have a 5mM total thiol concentration. Approximately 20 µL aliquot of this solution is spotted on a clean device, then left incubating for 3 hours at 4 °C and washed with ethanol. PSA (total) monoclonal antibody (Mab) is then immobilised on these self-assembled monolayers (SAMs) via a peptide bond. To immobilise the capture antibodies (Ab), the carboxyl groups of the SAM are sequentially modified with an aqueous mixture of 1-Ethyl-3-(3-dimethylaminopropyl)carbodiimide (EDC) (0.2 M) and N-Hydroxysuccinimide (NHS) (50 mM) for 30 min followed by rinsing with EtOH. Capture antibodies (total PSA) are covalently immobilised on the NHS-activated

SAM by spotting with 5 µL of a 0.5 mg/mL solution in 10 mM acetate buffer pH 5.0 for 1 hour at RT. The remaining NHS-active ester sites are blocked with 1.0 M ethanolamine pH 8.5 for 30 min at RT. The devices are then exposed to a solution of the PSA antigen, diluted in phosphate buffer pH 7.2 to the desired concentration for 15 min, followed by washing with phosphate buffer pH 7.2 to remove non-specifically bounded antigen. The devices are finally dried with N_2. At each monolayer immobilisation step on the surface, the SMR electro-acoustic performance is recorded by measuring Y, around the resonance region as shown in Figure 5.15 for the highest PSA antigen concentration of 20 ng/mL that is used in this work.

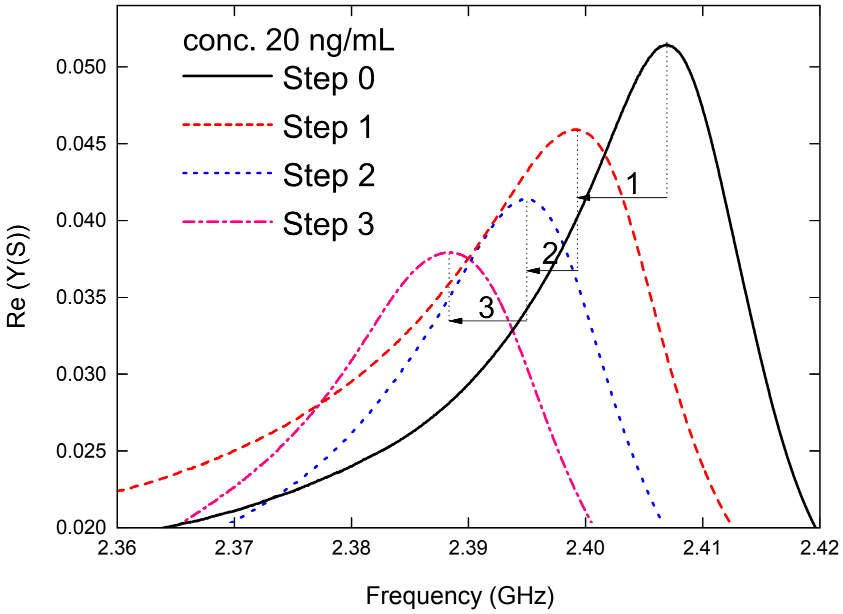

Figure 5.15: Frequency shifts at each stage for of the functionalisation process demonstrating reduction in f_r at each step indicating mass attachment. The concentration is for 20 ng/mL of PSA antigen, with step 1 being the thiol molecule formation, step 2 binding of antibody, and step 3 for the detection of PSA antigen.

The Δf_r (average of best 3 results) of the longitudinal mode devices at each concentration of PSA is plotted in Figure 5.16 and from this graph the sensitivity to PSA antigen concentration of the functionalised SMRs is calculated to be $-(0.33 \pm 0.02)$ MHz/(ng/mL). In the detection of prostrate cancer, the minimum

PSA antigen concentration is 4 ng/mL [199], which in the functionalised ZnO SMRs will lead to a Δf_r of 1.44 MHz that is well above the noise floor ($\sim$ 3 kHz) of the device operating at 2.5 GHz in the TLM.[200]

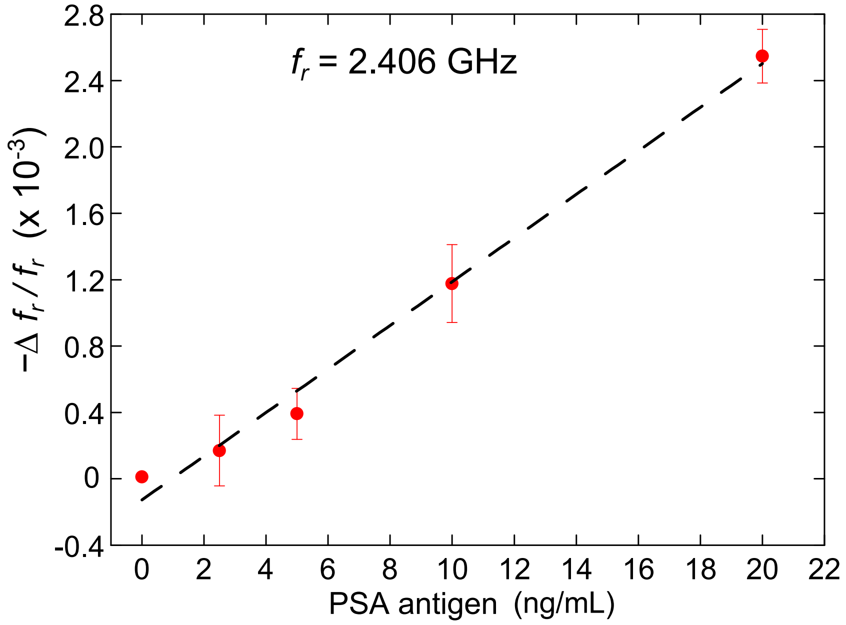

Figure 5.16: Frequency shifts of the longitudinal mode SMR with the binding of the different concentrations of PSA on the functionalised Au surface with SMR resonating at 2.41 GHz.

5.9 Chapter conclusion

In summary SMRs with TSM achieved with inclined c-axis piezoelectric layers are utilised to sense mass attachment, temperature variations, viscosity and finally to detect antibodies as a proof of concept. Methods to analyse the experimental data and to perform real time frequency tracking are described. Initial experiments with the AlN resonators with VACNTs grown on the active area from Chapter 4 are performed with BSA in water solutions. It is demonstrated that the longitudinal mode can be used for mass sensing and eventually biosensing, with the presence of the CNTs as an isolation layer to mitigate damping in DI water. The impact of this layer has substantial prospect for the large scale deployment of FBARs and SMRs operating in the longitudinal mode for real-time biosensing applications, thereby overcoming the fabrication limitations for TSM SMRs. Finally a typical cancer biomarker (PSA) for prostrate cancer is sensed using the TLM of a functionalised SMR operating air as a first experiment for future reference to compare functionalised CNTs coated SMRs, for in-liquid TLM biosensors.

Chapter 6

Conclusion

The main challenges in fabricating and using high frequency BAW resonators for gravimetric sensors in liquid have been addressed in this work. Generally to minimise the liquid damping, FBARs and SMRs are operated in the thickness shear mode that has a short decay length in liquids. TSM resonances are most efficiently achieved by an inclined *c*-axis (∼30°) piezoelectric layer, which leads to a quasi-shear mode and a quasi-longitudinal mode. Nonetheless the shortcomings of manufacturing inclined *c*-axis piezoelectric layers on a large scale due to the inhomogeneity of the inclinations and the costly modifications to the deposition systems have restricted their use in biosensing only to research level.

6.1 Shear mode resonators

In Chapter 3 the possibility of reducing significant changes to the deposition chamber is achieved by using textured surfaces and an off-axis deposition of the piezoelectric layer. The random roughness inherited from the deposition of an acoustic reflector stack and a polycrystalline AlN seed layer with uniform (103) orientations are compared. Inclined *c*-axis ZnO films are grown on each surface and SMRs are fabricated, leading to high inclination angles of up to 45° and narrower *c*-axis distributions, hence increased homogeneity, in the case of AlN seed layers. Both Q_r and k^2_{eff} are higher in the case of devices with the controlled surface texture of AlN compared to the random roughness of the reflector surface. However the AlN seed layer is piezoelectrically inactive as it is deposited with high pressure, low power and without substrate heating —conditions that promote polycrystalline and non-piezoelectric layers. The presence of the AlN between the active inclined *c*-axis ZnO and the bottom Mo electrode causes parasitic coupling losses thereby reducing both the achievable Q_r and k^2_{eff}.

To detect lower quantities of analytes, a higher Q_r is necessary. Therefore an electrically conductive textured surface such as Al deposited at higher T_S is considered. Based on the adatom mobility and energy, the morphology of the sputtered Al changes with T_S. At $T_\mathrm{S} = 100$ °C, the optimum roughness of 9.2 nm is achieved on ∼180 nm thick Al layers for the bottom electrode. The Al electrode deposited at this T_S has lower stress and uniform grain structure promoting a homogeneous *c*-axis inclination in the piezoelectric film. In this case the ZnO layers had ∼25° *c*-axis inclinations leading to k^2_{eff} higher than 2.5% and Q_r larger than 150. In addition the Al and ZnO could be deposited in the same chamber, thus facilitating the fabrication. In Chapter 5, S_m of 4.95 kHz·cm^2/ng is experimentally demonstrated with the TSM resonance by evaporating thin Al films on the active area of the resonator. TCF values of −66 ppm/K are extracted with the devices and their application as a viscosity sensor with different EtOH-water compositions is also evaluated. A functionalised SMR device is then used in liquid to detect Rabbit IgG antibody to illustrate the potential of the SMR as a biosensor. Despite the improved homogeneity and reduced deposition modifications from this work, fabrication of inclined *c*-axis piezoelectric films on larger substrates is still not viable. This is due to the exponential thickness variation and hence wide distribution of inclinations across large substrates in off-axis deposition. In contrast oriented *c*-axis piezoelectric films to excite the TLM, can be deposited homogeneously on large substrates.

6.2 Carbon nanotubes as isolation layer

The potential of partially isolating the longitudinal mode in SMRs to mitigate its propagation in liquid, while maintaining a sensitivity to mass attachment is investigated in Chapter 4. CNTs are considered as the liquid isolation layer as they have low mass density and provide an acoustic mismatch between the resonator and the liquid; they are grown only on the active area to function as a sensing layer with high surface area to volume ratio simultaneously. After initial experiments with the low temperature (450 °C) growth of high mass density and short CNTs using Co/Mo/Ti on ZnO SMRs, it became evident that ZnO films are chemically unstable in NH_3 gas during the annealing step. Consequently the devices did not show any response. A passivation layer such as Si_3N_4 or SiO_2 is therefore necessary. The growth of this type of CNTs is not reproducible on the top electrodes such as Au or Mo, which are used in this work.

Instead with Fe/Al layers, more reproducible and high forest density CNT layers are achieved on these electrodes. The growth conditions and SMR device structure are modified to withstand the higher temperature growth (600 °C). AlN is chosen as the piezoelectric film and the performance of both the shear and the longitudinal modes are assessed. Different CNT forest density and height are obtained by varying the Fe layer thickness from 0.5 to 4.5 nm, with the 0.5 nm Fe providing the tallest (several µm) and densest MWCNT forest. With thicker Fe layers, "spaghetti"-like and shorter CNT layers are obtained. Nevertheless all three CNT morphologies considered reduce the damping of the TLM in DI water. Longitudinal mode Q_r around 100 are measured with high density and tall forests (∼15 µm) compared with Q_r of only 5 without the CNTs. In Chapter 5 the mass sensitivity of the tall and highest density CNT forest is tested by dropping BSA solutions of different concentrations (0.05-2.5 mg/mL). With CNT forests of ∼15 µm height, both TSM and TLM are responsive to mass binding as the DI water can still penetrate to a certain depth in the forest; the TLM exhibits larger Δf_r (∼7 times higher) for the same concentration probably because the compressive vibration of CNT forest is stronger than the transverse wave. In contrast CNT forests of ∼30 µm height demonstrate Q_r of over 200 in BSA solutions but no significant Δf_r, as the mass attachment is further from the decay length of the resonances. A compromise between Q_r in liquid and S_m has to be considered in designing the CNT forest height. This work highlights the possibility for the first time of using the TLM in liquid for mass sensing with Q_r comparable to the shear mode, and hence the large scale fabrication of BAW resonators for real-time biosensors.

6.3 Future works

In this research, improvements in the homogeneity and inexpensive deposition techniques of inclined *c*-axis piezoelectric films for shear mode SMRs have been demonstrated. In addition possibilities to utilise the longitudinal mode for in-liquid sensing have been shown, with performance similar to —if not better than —those of conventional shear mode resonators. However in both themes further works are possible and are suggested in the following paragraphs for using BAW resonators as low-cost and real-time biosensors on a larger scale.

6.3.1 Implementation on FBARs

Inclined *c*-axis piezoelectric films on FBARs form part of an area that requires further work. Although SMRs are structurally robust, FBARs offer the possibility of flowing liquid at the back thereby isolating the contacts from the liquids. In addition, the membranes can be connected to a microfluidic channel to perform real-time sensing using the shear mode resonance. Nonetheless a major issue with the deposition of several materials such as the Al at higher T_S and the inclined *c*-axis ZnO is the residual compressive stress, which causes the films to crack during the back trench etching. Thermal annealing of the films could help relax the stress and increase the yield of FBARs, which can then be compared to shear mode SMRs.

6.3.2 Other materials

In the work on the shear modes, only ZnO was considered for the textured Al electrodes. Additional experiments are still necessary on AlN to determine the optimum surface promoting inclined *c*-axis AlN with uniform inclination angles. Electrodes such as W and methods to texture them are also under consideration owing to their higher acoustic impedance, which improve acoustic confinement of the wave and consequently higher Q_r can be obtained. AlN has superior chemical stability compared to ZnO, the latter requires a passivation layer with either a nitride or an oxide. This also needs to be investigated to confirm that ZnO is protected by the presence of such layers and can function longer in BAW biosensors. The merits of ZnO are its ease of deposition and higher piezoelectricity compared to AlN, therefore a comparison with AlN on biosensing applications is also essential.

6.3.3 CNT isolation layer

To assess the effects of the CNTs on both the shear and the longitudinal modes, the SMRs in this work are fabricated with inclined *c*-axis AlN. Yet such films resonate with neither the "pure" longitudinal nor the "pure" shear modes. Additional experiments are accordingly required to evaluate the isolation effect of CNTs on the *c*-axis oriented AlN films resonating in the longitudinal mode. The CNTs grown in this work were multi-walled and thus the possibility exists in comparing the quality of isolation and mass sensitivities achieved with SWCNTs forests. Although the SMRs with CNTs have been demonstrated to be sensitive to mass binding, a proof of a functionalised CNT layer capable of binding to specific biomolecules is envisaged to confirm the concept. This work is under consideration, which will consist of functionalising the CNTs to detect PSA in real-time using the longitudinal mode. Moreover alternative isolation layers such as parylene should be explored as isolation layer because of their easier deposition.

6.3.4 Modelling

A shortcoming of this work has been the limited modelling both by analytical and finite element analysis. This is due to time constraint and the complexity of modelling CNT arrays, which are inherently different from bulk materials. In this work, emphasis is on the experimental fabrication, which will then be extended to models to explain the results achieved. Therefore simulations in COMSOL Multiphysics® and analytical models to optimise the CNT densities and heights are avenues to explore in order to design forest morphologies to improve longitudinal mode operation in detecting biochemicals in liquid. In addition such modelling can be used in conjunction with the inclined *c*-axis growth of piezoelectric films to determine the ideal roughness and structures necessary to efficiently excite the shear mode.

Bibliography

[1] IARC, *GLOBOCAN 2012: Estimated Cancer Incidence, Mortality and Prevalence Worldwide in 2012*, http://globocan.iarc.fr/Pages/fact_sheets_cancer.aspx, Online, Jan. 2013.

[2] World Health Organisation, *10 facts about cancer*, http://www.who.int/features/factfiles/cancer/en/, Online, Jan. 2013.

[3] D. R. Thévenot, K. Toth, R. A. Durst, and G. S. Wilson, "Electrochemical biosensors: Recommended definitions and classification," *Biosensors and Bioelectronics*, vol. 16, no. 1–2, pp. 121–131, 2001.

[4] C. I. L. Justino, T. A. Rocha-Santos, and A. C. Duarte, "Review of analytical figures of merit of sensors and biosensors in clinical applications," *Trends in Analytical Chemistry*, vol. 29, no. 10, pp. 1172–1183, 2010.

[5] G. G. Guilbault, "Biosensors," *Current Opinion in Biotechnology*, vol. 2, no. 1, pp. 3–8, 1991.

[6] G. Wingqvist, "AlN-based sputter-deposited shear mode thin film bulk acoustic resonator (FBAR) for biosensor applications — A review," *Surface and Coatings Technology*, vol. 205, no. 5, p. 1279, 2010.

[7] J. I. Reyes De Corcuera and R. P. Cavalieri, "Biosensors," in, M. D. Inc, Ed. New York: Encyclopedia of Agricultural, Food and Biological Engineering, 2003, ch. 42, pp. 173–177.

[8] S. Badilescu and M. Packirisamy, *BioMEMS: Science and Engineering Perspectives.* CRC Press, 2011.

[9] D. Grieshaber, R. MacKenzie, J. Vörös, and E. Reimhult, “Electrochemical Biosensors - Sensor Principles and Architectures,” *Sensors*, vol. 8, no. 3, pp. 1400–1458, 2008.

[10] W. Tan, L. Sabet, Y. Li, T. Yu, P. R. Klokkevold, D. T. Wong, and C.-M. Ho, “Optical protein sensor for detecting cancer markers in saliva,” *Biosensors and Bioelectronics*, vol. 24, no. 2, pp. 266–271, Oct. 2008.

[11] G. S. Wilson and R. Gifford, “Biosensors for real-time in vivo measurements,” *Biosensors and Bioelectronics*, vol. 20, no. 12, pp. 2388–2403, Jun. 2005.

[12] V. Scognamiglio, “Nanotechnology in glucose monitoring: Advances and challenges in the last 10 years,” *Biosensors and Bioelectronics*, vol. 47, pp. 12–25, Sep. 2013.

[13] W. Pang, H. Zhao, E. S. Kim, H. Zhang, H. Yu, and X. Hu, “Piezoelectric microelectromechanical resonant sensors for chemical and biological detection.,” *Lab Chip*, vol. 12, no. 1, pp. 29–44, 2012.

[14] R. Pilolli, L. Monaci, and A. Visconti, “Advances in biosensor development based on integrating nanotechnology and applied to food-allergen management,” *Trends in Analytical Chemistry*, vol. 47, pp. 12–26, Jun. 2013.

[15] N. R. Stradiotto, H. Yamanaka, and M. V. B. Zanoni, “Electrochemical sensors: a powerful tool in analytical chemistry,” en, *Journal of the Brazilian Chemical Society*, vol. 14, pp. 159–173, Apr. 2003.

[16] J. M. Gamba, “The role of transport phenomena in whispering gallery mode optical biosensor performance,” PhD thesis, California Institute of Technology, 2012.

[17] M. N. Velasco-Garcia, "Optical biosensors for probing at the cellular level: A review of recent progress and future prospects," *Seminars in Cell & Developmental Biology*, vol. 20, no. 1, pp. 27–33, Feb. 2009.

[18] T. D. Martins, A. C. C. Ribeiro, H. S. de Camargo, P. A. da Costa Filho, H. P. M. Cavalcante, and D. L. Dias, "New Insights on Optical Biosensors: Techniques, Construction and Application," in *State of the Art in Biosensors - General Aspects*, T. Rinken, Ed., InTech, Mar. 2013, pp. 111–140.

[19] J. A. Lane, R. K. Mehra, S. D. Carrington, and R. M. Hickey, "Development of biosensor-based assays to identify anti-infective oligosaccharides," *Analytical Biochemistry*, vol. 410, no. 2, pp. 200–205, Mar. 2011.

[20] X. Yang, J. Kirsch, and A. Simonian, "Campylobacter spp. detection in the 21st century: A review of the recent achievements in biosensor development," *Journal of Microbiological Methods*, vol. 95, no. 1, pp. 48–56, Oct. 2013.

[21] O. Tigli and S. U. Senveli, "Biosensors in the small scale: Methods and technology trends," *IET Nanobiotechnology*, vol. 7, no. 1, pp. 7–21, Mar. 2013.

[22] M. Nirschl, F. Reuter, and J. Vörös, "Review of Transducer Principles for Label-Free Biomolecular Interaction Analysis," *Biosensors*, vol. 1, no. 4, pp. 70–92, Dec. 2011.

[23] M. Nirschl, "Thin-film Bulk Acoustic Resonators for Biomolecular Interaction Analysis," PhD thesis, ETH Zürich, May 2011.

[24] J. Tamayo, P. M. Kosaka, J. J. Ruz, Á. San Paulo, and M. Calleja, "Biosensors based on nanomechanical systems," *Chemical Society Reviews*, vol. 42, no. 3, p. 1287, 2013.

[25] J. L. Arlett, E. B. Myers, and M. L. Roukes, "Comparative advantages of mechanical biosensors," *Nature Nanotechnology*, vol. 6, no. 4, pp. 203–215, Mar. 2011.

[26] J. Lee, W. Shen, K. Payer, T. P. Burg, and S. R. Manalis, "Toward Attogram Mass Measurements in Solution with Suspended Nanochannel Resonators," *Nano Letters*, vol. 10, no. 7, pp. 2537–2542, Jul. 2010.

[27] A. Boisen, S. Dohn, S. S. Keller, S. Schmid, and M. Tenje, "Cantilever-like micromechanical sensors," *Reports on Progress in Physics*, vol. 74, no. 3, p. 036 101, Feb. 2011.

[28] S. Fanget, S. Hentz, P. Puget, J. Arcamone, M. Matheron, E. Colinet, P. Andreucci, L. Duraffourg, E. Myers, and M. L. Roukes, "Gas sensors based on gravimetric detection–A review," *Sensors and Actuators B: Chemical*, vol. 160, no. 1, pp. 804–821, Dec. 2011.

[29] F. Z. Bi and B. P. Barber, "Bulk acoustic wave RF technology," *Microwave Magazine, IEEE*, vol. 9, no. 5, pp. 65–80, 2008.

[30] G. V. Tsarenkov, "10+ GHz piezoelectric BAW resonators based on semiconductor multilayer heterostructures," in *1999 IEEE Ultrasonics Symposium. Proceedings. International Symposium (Cat. No.99CH37027)*, Institute of Electrical and Electronics Engineers, 1999, pp. 939–942.

[31] I. Voiculescu and A. N. Nordin, "Acoustic wave based MEMS devices for biosensing applications," *Biosensors and Bioelectronics*, vol. 33, no. 1, pp. 1–9, Mar. 2012.

[32] S. Rey-Mermet, R. Lanz, and P. Muralt, "Bulk acoustic wave resonator operating at 8 GHz for gravimetric sensing of organic films," *Sensors and Actuators B: Chemical*, vol. 114, no. 2, p. 681, 2006.

[33] I. Katardjiev and V. Yantchev, "Recent developments in thin film electroacoustic technology for biosensor applications," *Vacuum*, vol. 86, no. 5, pp. 520–531, Jan. 2012.

[34] R. Aigner, “SAW and BAW technologies for RF filter applications: A review of the relative strengths and weaknesses,” in *Ultrasonics Symposium, 2008. IUS 2008. IEEE*, 2008, pp. 582–589.

[35] H. Nakahata, A. Hachigo, K. Itakura, and S. Shikata, “Fabrication of high frequency SAW filters from 5 to 10 GHz using SiO_2/ZnO/diamond structure,” in *Ultrasonics Symposium, 2000 IEEE*, vol. 1, IEEE, 2000, pp. 349–352.

[36] S. W. Wenzel and R. M. White, “Analytic comparison of the sensitivities of bulk-wave, surface-wave, and flexural plate-wave ultrasonic gravimetric sensors,” *Applied Physics Letters*, vol. 54, no. 20, p. 1976, 1989.

[37] K. A. Marx, “Quartz Crystal Microbalance: A Useful Tool for Studying Thin Polymer Films and Complex Biomolecular Systems at the Solution-Surface Interface.,” *Biomacromolecules*, vol. 4, no. 5, pp. 1099–1120, 2003.

[38] G. Sauerbrey, “Verwendung von Schwingquarzen zur Wägung dünner Schichten und zur Mikrowägung,” *Zeitschrift für Physik*, vol. 155, no. 2, p. 206, 1959.

[39] Y. Q. Fu, J. K. Luo, X. Y. Du, A. J. Flewitt, Y. Li, G. H. Markx, A. J. Walton, and W. I. Milne, “Recent developments on ZnO films for acoustic wave based bio-sensing and microfluidic applications: a review,” *Sensors and Actuators B: Chemical*, vol. 143, no. 2, p. 606, 2010.

[40] C. D. Corso, A. Dickherber, and W. D. Hunt, “Lateral field excitation of thickness shear mode waves in a thin film ZnO solidly mounted resonator,” *Journal of Applied Physics*, vol. 101, no. 5, p. 054 514, 2007.

[41] Y. Montagut, J. V. García, Y. Jiménez, C. March, Á. Montoya, and A. Arnau, “Validation of a Phase-Mass Characterization Concept and Interface for Acoustic Biosensors,” *Sensors*, vol. 11, no. 12, pp. 4702–4720, Apr. 2011.

[42] S Tadigadapa and K Mateti, “Piezoelectric MEMS sensors: State-of-the-art and perspectives,” *Measurement Science and Technology*, vol. 20, no. 9, p. 092 001, Sep. 2009.

[43] M. Nirschl, A. Rantala, K. Tukkiniemi, S. Auer, A.-C. Hellgren, D. Pitzer, M. Schreiter, and I. Vikholm-Lundin, “CMOS-Integrated Film Bulk Acoustic Resonators for Label-Free Biosensing,” *Sensors*, vol. 10, no. 5, pp. 4180–4193, May 2010.

[44] Z. Yan, X. Y. Zhou, G. K. H. Pang, T. Zhang, W. L. Liu, J. G. Cheng, Z. T. Song, S. L. Feng, L. H. Lai, J. Z. Chen, and Y. Wang, “ZnO-based film bulk acoustic resonator for high sensitivity biosensor applications,” *Applied Physics Letters*, vol. 90, no. 14, p. 143 503, 2007.

[45] J. K. Luo, Y. Q. Fu, and W. I. Milne, “Acoustic Wave Based Microfluidics and Lab-on-a-Chip,” in *Modeling and Measurement Methods for Acoustic Waves and for Acoustic Microdevices*, M. G. Beghi, Ed., InTech, Aug. 2013, ch. 21.

[46] K. Tukkiniemi, A. Rantala, M. Nirschl, D. Pitzer, T. Huber, and M. Schreiter, “Fully integrated FBAR sensor matrix for mass detection,” *Procedia Chemistry*, vol. 1, no. 1, pp. 1051–1054, Sep. 2009.

[47] H. Zhang, M. S. Marma, E. S. Kim, C. E. McKenna, and M. E. Thompson, “A film bulk acoustic resonator in liquid environments,” *Journal of Micromechanics and Microengineering*, vol. 15, no. 10, p. 1911, 2005.

[48] G. Wingqvist, J. Bjurström, A. Hellgren, and I. Katardjiev, “Immunosensor utilizing a shear mode thin film bulk acoustic sensor,” *Sensors and Actuators B: Chemical*, vol. 127, no. 1, p. 248, 2007.

[49] G. Wingqvist, V. Yantchev, and I. Katardjiev, “Mass sensitivity of multilayer thin film resonant BAW sensors,” *Sensors and Actuators A: Physical*, vol. 148, no. 1, pp. 88–95, Nov. 2008.

[50] M. DeMiguel-Ramos, T. Mirea, M. Clement, J. Olivares, J. Sangrador, and E. Iborra, "Optimized tilted c-axis AlN films for improved operation of shear mode resonators," *Thin Solid Films*, pp. 219–223, Aug. 2015.

[51] M. Clement, E. Iborra, J. Olivares, M. DeMiguel-Ramos, T. Mirea, and J. Sangrador, "On the effectiveness of lateral excitation of shear modes in AlN layered resonators," *Ultrasonics*, vol. 54, no. 6, pp. 1504–1508, Aug. 2014.

[52] G. Wingqvist, J. Bjurström, L. Liljeholm, V. Yantchev, and I. Katardjiev, "Shear mode AlN thin film electro-acoustic resonant sensor operation in viscous media," *Sensors and Actuators B: Chemical*, vol. 123, no. 1, pp. 466–473, Apr. 2007.

[53] T. Yanagitani, M. Kiuchi, M. Matsukawa, and Y. Watanabe, "Characteristics of Pure-shear Mode BAW Resonators Consisting of $(11\bar{2}0)$ Textured ZnO Films," *Ultrasonics, Ferroelectrics, and Frequency Control, IEEE Transactions on*, vol. 54, no. 8, pp. 1680–1686, Aug. 2007.

[54] A. Dickherber, C. D. Corso, and W. Hunt, "Lateral Field Excitation (LFE) of Thickness Shear Mode (TSM) Acoustic Waves in Thin Film Bulk Acoustic Resonators (FBAR) as a Potential Biosensor," in *Engineering in Medicine and Biology Society, 2006. EMBS '06. 28th Annual International Conference of the IEEE*, 2006, pp. 4590–4593.

[55] K. M. Lakin, K. T. McCarron, J. Belsick, and J. F. McDonald, "Thin film bulk acoustic wave resonator and filter technology," in *Radio and Wireless Conference, 2001. RAWCON 2001. IEEE*, 2001, pp. 89–92.

[56] R. Thalhammer, J. Kaitila, S. Zieglmeier, and L. Elbrecht, "4E-3 Spurious Mode Suppression in BAW Resonators," in *2006 IEEE Ultrasonics Symposium*, Oct. 2006, pp. 456–459.

[57] R. Ruby, "Review and Comparison of Bulk Acoustic Wave FBAR, SMR Technology," in *Ultrasonics Symposium, 2007. IEEE*, 2007, pp. 1029–1040.

[58] Research and Markets, *Avago FBAR Filter All-Silicon MEMS Duplexer Reverse Costing Analysis*, http://www.researchandmarkets.com/reports/2411910/avago_fbar_filter_allsilicon_mems_duplexer, Feb. 2013.

[59] W. Lin, R. Zhang, K.-S. Moon, and C. P. Wong, "Synthesis of High-Quality Vertically Aligned Carbon Nanotubes on Bulk Copper Substrate for Thermal Management," *IEEE Transactions on Advanced Packaging*, vol. 33, no. 2, pp. 370–376, May 2010.

[60] K. A. Shah and B. A. Tali, "Synthesis of carbon nanotubes by catalytic chemical vapour deposition: A review on carbon sources, catalysts and substrates," *Materials Science in Semiconductor Processing*, vol. 41, pp. 67–82, Jan. 2016.

[61] T. Mirea, J. Olivares, M. Clement, M. DeMiguel-Ramos, J. de Frutos, J. Sangrador, and E. Iborra, "Carbon nanotube growth on piezoelectric AlN films: Influence of catalyst underlayers," *RSC Adv.*, vol. 5, no. 98, pp. 80 682–80 687, 2015.

[62] J. F. Rosenbaum, *Bulk Acoustic Wave Theory and Devices.* New York: Artech House, 1945.

[63] J. Weber, M. Link, R. Primig, D. Pitzer, and M. Schreiter, "High Frequency Viscosity Sensing with FBARs," in *International Frequency Control Symposium and Exposition, 2006 IEEE*, Jun. 2006, pp. 117–122.

[64] K.-Y. Hashimoto, *RF Bulk Acoustic Wave Filters for Communications*, ser. Artech House Microwave Library. Boston: Artech House, 2009.

[65] L. García-Gancedo, J. Pedrós, E. Iborra, M. Clement, X. B. Zhao, J. Olivares, J. Capilla, J. K. Luo, J. R. Lu, W. I. Milne, and A. J. Flewitt, "Direct comparison of the gravimetric responsivities of ZnO-based FBARs and SMRs," *Sensors and Actuators B: Chemical*, vol. 183, pp. 136–143, 2013.

[66] L. García-Gancedo, Z. Zhu, E. Iborra, M. Clement, J. Olivares, A. J. Flewitt, W. I. Milne, G. M. Ashley, J. K. Luo, X. B. Zhao, and J. R. Lu, "AlN-based BAW resonators with CNT electrodes for gravimetric biosensing," *Sensors and Actuators B: Chemical*, vol. 160, no. 1, pp. 1386–1393, 2011.

[67] M. L. Johnston, I. Kymissis, and K. L. Shepard, "FBAR-CMOS Oscillator Array for Mass-Sensing Applications," *Sensors Journal, IEEE*, vol. 10, no. 6, pp. 1042–1047, 2010.

[68] K. J. Coakley, J. D. Splett, M. D. Janezic, and R. F. Kaiser, "Estimation of Q-factors and resonant frequencies," *Microwave Theory and Techniques, IEEE Transactions on*, vol. 51, no. 3, pp. 862–868, 2003.

[69] Y. Zhang and D. Chen, *Multilayer Integrated Film Bulk Acoustic Resonators.* Springer Berlin Heidelberg, 2013.

[70] S. Chang, N. Rogacheva, and C. Chou, "Analysis of methods for determining electromechanical coupling coefficients of piezoelectric elements," *IEEE Transactions on Ultrasonics, Ferroelectrics and Frequency Control*, vol. 42, no. 4, pp. 630–640, Jul. 1995.

[71] H. Campanella, *Acoustic Wave and Electromechanical Resonators: Concept to Key Applications (Integrated Microsystems).* Artech House, 2010.

[72] K. M. Lakin, "Thin film resonators and filters," in *Ultrasonics Symposium, 1999. Proceedings. 1999 IEEE*, vol. 2, 1999, pp. 895–906.

[73] S. Razafimandimby, C. Tilhac, A. Cathelin, A. Kaiser, and D. Belot, "A novel architecture of a tunable bandpass BAW-filter for a WCDMA transceiver," *Analog Integrated Circuits and Signal Processing*, vol. 49, no. 3, p. 237, 2006.

[74] D. S. Ballantine Jr., R. M. White, S. J. Martin, A. J. Ricco, E. T. Zellers, G. C. Frye, and H. Wohltjen, *Acoustic Wave Sensors: Theory, Design, & Physico-Chemical Applications (Applications of Modern Acoustics).* Academic Press, 1996.

[75] W. E. Newell, “Face-mounted piezoelectric resonators,” *Proceedings of the IEEE*, vol. 53, no. 6, pp. 575–581, 1965.

[76] R. Weigel, D. P. Morgan, J. M. Owens, A. Ballato, K. M. Lakin, K.-Y. Hashimoto, and C. C. W. Ruppel, “Microwave acoustic materials, devices, and applications,” *Microwave Theory and Techniques, IEEE Transactions on*, vol. 50, no. 3, pp. 738–749, 2002.

[77] W. Xu, X. Zhang, H. Yu, A. Abbaspour-Tamijani, and J. Chae, “In-Liquid Quality Factor Improvement for Film Bulk Acoustic Resonators by Integration of Microfluidic Channels,” *Electron Device Letters, IEEE*, vol. 30, no. 6, pp. 647–649, 2009.

[78] H. Zhang and E. S. Kim, “Micromachined Acoustic Resonant Mass Sensor,” *Microelectromechanical Systems, Journal of*, vol. 14, no. 4, pp. 699–706, 2005.

[79] G. G. Fattinger, “BAW resonator design considerations - An overview,” in *2008 IEEE International Frequency Control Symposium*, Institute of Electrical and Electronics Engineers (IEEE), May 2008.

[80] J. Kaitila, “Review of Wave Propagation in BAW Thin Film Devices - Progress and Prospects,” in *2007 IEEE Ultrasonics Symposium Proceedings*, Institute of Electrical and Electronics Engineers (IEEE), Oct. 2007.

[81] J. Enlund, D. Martin, V. Yantchev, and I. Katardjiev, “Solidly mounted thin film electro-acoustic resonator utilizing a conductive Bragg reflector,” *Sensors and Actuators A: Physical*, vol. 141, no. 2, p. 598, 2008.

[82] R. Aigner, “MEMS in RF Filter Applications: Thin-film Bulk Acoustic Wave Technology,” *Sensors Update*, vol. 12, no. 1, pp. 175–210, Feb. 2003.

[83] J.-W. Lobeek, R. Strijbos, A. Jansman, N. X. Li, A. B. Smolders, and N. Pulsford, “High-Q BAW Resonator on Pt/Ta2O5/SiO2-based Reflector Stack,” in *Institute of Electrical and Electronics Engineers (IEEE)*, Institute of Electrical and Electronics Engineers (IEEE), Jun. 2007.

[84] R. Strijbos, A. Jansman, J.-W. Lobeek, N. X. Li, and N. Pulsford, "Design and Characterisation of High-Q Solidly-Mounted Bulk Acoustic Wave Filters," in *Institute of Electrical and Electronics Engineers (IEEE)*, Institute of Electrical and Electronics Engineers (IEEE), 2007.

[85] B. A. Auld, *Acoustic Fields and Waves in Solids, Vol. 2.* Krieger Pub Co, 1990.

[86] O. Wolfbeis, *Piezoelectric Sensors*, A. Janshoff and C. Steinem, Eds. Springer Berlin Heidelberg, 2007.

[87] J. Enlund, D. M. Martin, V. Yantchev, and I. Katardjiev, "FBAR Sensor Array for in Liquid Operation," *Sensors Journal, IEEE*, vol. 10, no. 12, pp. 1903–1904, 2010.

[88] J. Bjurström, G. Wingqvist, and I. Katardjiev, "Synthesis of textured thin piezoelectric AlN films with a nonzero c-axis mean tilt for the fabrication of shear mode resonators," *Ultrasonics, Ferroelectrics and Frequency Control, IEEE Transactions on*, vol. 53, no. 11, pp. 2095–2100, 2006.

[89] M. Clement, E. Iborra, J. Olivares, M. de Miguel-Ramos, J. Capilla, and J. Sangrador, "On the lateral excitation of shear modes in AlN layered resonators," in *2012 IEEE International Ultrasonics Symposium*, Institute of Electrical and Electronics Engineers, Oct. 2012, pp. 1–4.

[90] M. Gorisse, A. Reinhardt, C. Billard, M. Borel, E. Defay, T. Bertaud, T. Lacrevaz, and C. Bermond, "Lateral Field Excitation of membrane-based Aluminum Nitride resonators," in *2011 Joint Conference of the IEEE International Frequency Control and the European Frequency and Time Forum (FCS) Proceedings*, Institute of Electrical and Electronics Engineers, May 2011, pp. 1–5.

[91] R. Gabl, H. D. Feucht, H. Zeininger, G. Eckstein, M. Schreiter, R. Primig, D. Pitzer, and W. Wersing, "First results on label-free detection of DNA and protein molecules using a novel integrated sensor technology based on gravi-

metric detection principles," *Biosensors and Bioelectronics*, vol. 19, no. 6, p. 615, 2004.

[92] R. Gabl, E. Green, M. Schreiter, H. D. Feucht, H. Zeininger, R. Primig, D. Pitzer, G. Eckstein, and W. Wersing, "Novel integrated FBAR sensors: a universal technology platform for bio- and gas-detection," in *Sensors, 2003. Proceedings of IEEE*, vol. 2, 2003, pp. 1184–1188.

[93] T. Nishihara, T. Yokoyama, T. Miyashita, and Y. Satoh, "High performance and miniature thin film bulk acoustic wave filters for 5 GHz," in *Ultrasonics Symposium, 2002. Proceedings. 2002 IEEE*, vol. 1, 2002, pp. 969–972.

[94] W. Xu, X. Zhang, S. Choi, and J. Chae, "A High-Quality-Factor Film Bulk Acoustic Resonator in Liquid for Biosensing Applications," *Microelectromechanical Systems, Journal of*, vol. 20, no. 1, pp. 213–220, 2011.

[95] N. F. Foster, G. A. Coquin, G. A. Rozgonyi, and F. A. Vannatta, "Cadmium Sulphide and Zinc Oxide Thin-Film Transducers," *IEEE Transactions on Sonics and Ultrasonics*, vol. 15, no. 1, pp. 28–40, Jan. 1968.

[96] M. Link, "Study and realization of shear wave mode solidly mounted film bulk acoustic resonators (FBAR) made of c-axis inclined zinc oxide (ZnO) thin films: Application as gravimetric sensors in liquid environments.," PhD thesis, Ecole Polytechnique Fédérale de Lausanne, 2006.

[97] J. V. Tirado, "Bulk acoustic wave resonators and their application to microwave devices," PhD thesis, Universitat Autonoma de Barcelona, 2010.

[98] D. M. Pozar, *Microwave Engineering, 4th Edition*. Wiley, 2011.

[99] Q. Chen, "Fabrication and characterization of AlN film bulk acoustic wave resonator," PhD thesis, University of Pittsburg, Jul. 2006.

[100] G. F. Perez-Sanchez and A. Morales-Acevedo, "Design of bulk acoustic wave resonators based on ZnO for filter applications," in *Electrical Engineering,*

Computing Science and Automatic Control,CCE,2009 6th International Conference on, 2009, pp. 1–6.

[101] W. P. Mason, “Effect of Impurities and Phonon Processes on the Ultrasonic Attenuation of Germanium, Crystal Quartz, and Silicon,” *Physical Acoustics*, pp. 235–286, 1965.

[102] J. D. Larson, S. R. Gilbert, and B. Xu, “PZT material properties at UHF and microwave frequencies derived from FBAR measurements,” in *Ultrasonics Symposium, 2004 IEEE*, vol. 1, Aug. 2004, pp. 173–177.

[103] E. Benes, “Improved quartz crystal microbalance technique,” *Journal of Applied Physics*, vol. 56, no. 3, pp. 608–626, Aug. 1984.

[104] M. Benetti, D. Cannatà, F. Di Pietrantonio, V. Foglietti, and E. Verona, “Microbalance chemical sensor based on thin-film bulk acoustic wave resonators,” *Applied Physics Letters*, vol. 87, no. 17, p. 173 504, 2005.

[105] M. Link, J. Weber, M. Schreiter, W. Wersing, O. Elmazria, and P. Alnot, “Sensing characteristics of high-frequency shear mode resonators in glycerol solutions,” *Sensors and Actuators B: Chemical*, vol. 121, no. 2, p. 372, 2007.

[106] S. Meyburg, G. Wrobel, R. Stockmann, J. Moers, S. Ingebrandt, and A. Offenhäusser, “Single cell recordings with pairs of complementary transistors,” *Applied Physics Letters*, vol. 89, no. 1, p. 013 901, 2006.

[107] M. DeMiguel-Ramos, G. Rughoobur, A. Flewitt, T. Mirea, B. Diaz-Duran, J. Olivares, M. Clement, and E. Iborra, “Transparent thin film bulk acoustic wave resonators,” in *2016 European Frequency and Time Forum (EFTF)*, Institute of Electrical and Electronics Engineers (IEEE), Apr. 2016.

[108] G. Chen, X. Zhao, X. Wang, H. Jin, S. Li, S. Dong, A. J. Flewitt, W. I. Milne, and J. K. Luo, “Film bulk acoustic resonators integrated on arbitrary substrates using a polymer support layer,” *Scientific Reports*, vol. 5, p. 9510, Mar. 2015.

[109] L. Arapan, "Thin Film Plate Acoustic Resonators for Frequency Control and Sensing Applications," PhD thesis, Uppsala University, Sweden, 2012.

[110] S. V. Krishnaswamy, J. Rosenbaum, S. Horwitz, C. Vale, and R. A. Moore, "Film bulk acoustic wave resonator technology," in *Ultrasonics Symposium, 1990. Proceedings., IEEE 1990*, 1990, pp. 529–536.

[111] H.-Y. Kim, K.-B. Kim, S. H. Cho, and Y.-I. Kim, "Analysis of resonance characteristics of Bragg reflector type film bulk acoustic resonator," *Surface and Coatings Technology*, vol. 211, pp. 143–147, Oct. 2012.

[112] T. S. Low and W. Guo, "Modeling of a three-layer piezoelectric bimorph beam with hysteresis," *Journal of Microelectromechanical Systems*, vol. 4, no. 4, pp. 230–237, 1995.

[113] K. M. Lakin, "Acoustic bulk wave composite resonators," *Applied Physics Letters*, vol. 38, no. 3, pp. 125–127, 1981.

[114] C. K. Lee, S. Cochran, A. Abrar, K. J. Kirk, and F. Placido, "Thick aluminium nitride films deposited by room-temperature sputtering for ultrasonic applications," *Ultrasonics*, vol. 42, no. 1-9, pp. 485–490, Apr. 2004.

[115] L. García-Gancedo, J. Pedrós, Z. Zhu, A. J. Flewitt, W. I. Milne, J. K. Luo, and C. J. B. Ford, "Room-temperature remote-plasma sputtering of c-axis oriented zinc oxide thin films," *Journal of Applied Physics*, vol. 112, no. 1, p. 014 907, 2012.

[116] T. Yokoyama, T. Nishihara, S. Taniguchi, M. Iwaki, Y. Satoh, M. Ueda, and T. Miyashita, "New electrode material for low-loss and high-Q FBAR filters," in *Ultrasonics Symposium, 2004 IEEE*, vol. 1, 2004, pp. 429–432.

[117] X. L. He, L. García-Gancedo, P. C. Jin, J. Zhou, W. B. Wang, S. R. Dong, J. K. Luo, A. J. Flewitt, and W. I. Milne, "Film bulk acoustic resonator pressure sensor with self temperature reference," *Journal of Micromechanics and Microengineering*, vol. 22, no. 12, p. 125 005, 2012.

[118] L. García-Gancedo, J. Pedrós, X. B. Zhao, G. M. Ashley, A. J. Flewitt, W. I. Milne, C. J. B. Ford, J. R. Lu, and J. K. Luo, "Dual-mode thin film bulk acoustic wave resonators for parallel sensing of temperature and mass loading," *Biosensors and Bioelectronics*, vol. 38, no. 1, pp. 369–374, Oct. 2012.

[119] D. Cannatà, M. Benetti, F. Di Pietrantonio, E. Verona, A. Palla-Papavlu, V. Dinca, M. Dinescu, and T. Lippert, "Nerve agent simulant detection by solidly mounted resonators (SMRs) polymer coated using laser induced forward transfer (LIFT) technique," *Sensors and Actuators B: Chemical*, vol. 173, pp. 32–39, Oct. 2012.

[120] P. Kumar and C. C. Tripathi, "Design of a New Step-like Frame FBAR for Suppression of Spurious Resonances," English, *Radioengineering*, vol. 22, no. 3, pp. 687–693, Sep. 2013.

[121] L. García-Gancedo, F. Al-Naimi, A. J. Flewitt, W. I. Milne, G. M. Ashley, J. K. Luo, X. Zhao, and J. R. Lu, "ZnO-Based FBAR resonators with carbon nanotube electrodes," *IEEE Transactions on Ultrasonics, Ferroelectrics and Frequency Control*, vol. 58, no. 11, pp. 2438–2445, Nov. 2011.

[122] M. Clement, J. Olivares, E. Iborra, S. González-Castilla, N. Rimmer, and A. Rastogi, "AlN films sputtered on iridium electrodes for bulk acoustic wave resonators," *Thin Solid Films*, vol. 517, no. 16, pp. 4673–4678, Jun. 2009.

[123] L. García-Gancedo, F. Al-Naimi, A. J. Flewitt, W. I. Milne, G. M. Ashley, J. K. Luo, X. B. Zhao, and J. R. Lu, "Fabrication of high-Q film bulk acoustic resonator (FBAR) filters with carbon nanotube (CNT) electrodes," in *2010 IEEE International Ultrasonics Symposium*, 2010, p. 301.

[124] L. García-Gancedo, E. Iborra, M. Clement, J. Olivares, Z. Zhu, A. J. Flewitt, W. I. Milne, G. M. Ashley, J. K. Luo, X. B. Zhao, and J. R. Lu, "Solidly mounted resonators with carbon nanotube electrodes for biosensing applications," in *Frequency Control and the European Frequency and Time Forum (FCS), 2011 Joint Conference of the IEEE International*, 2011, pp. 1–5.

[125] S. Liu, Q. Shen, Y. Cao, L. Gan, Z. Wang, M. L. Steigerwald, and X. Guo, “Chemical functionalization of single-walled carbon nanotube field-effect transistors as switches and sensors,” *Coordination Chemistry Reviews*, vol. 254, no. 9-10, p. 1101, 2010.

[126] F. Lu, L. Gu, M. J. Meziani, X. Wang, P. G. Luo, L. M. Veca, L. Cao, and Y. P. Sun, “Advances in Bioapplications of Carbon Nanotubes,” *Advanced Materials*, vol. 21, no. 2, p. 139, 2009.

[127] M. Mann, Y. Zhang, K. B. K. Teo, T. Wells, M. M. El Gomati, and W. I. Milne, “Controlling the growth of carbon nanotubes for electronic devices,” *Microelectronic Engineering*, vol. 87, no. 5-8, pp. 1491–1493, 2010.

[128] H. C. Pineda, “Thin–film bulk acoustic wave resonators - FBAR: Fabrication, heterogeneous integration with CMOS technologies and sensor applications.,” PhD thesis, Université de Montpellier II and Universitat Autònoma de Barcelona, Dec. 2007.

[129] S. Marksteiner, J. Kaitila, G. G. Fattinger, and R. Aigner, “Optimization of acoustic mirrors for solidly mounted BAW resonators,” in *Ultrasonics Symposium, 2005 IEEE*, vol. 1, Sep. 2005, pp. 329–332.

[130] A Reinhard, N. Buffet, and A Shirakawa, “Simulation of BAW Resonators Frequency Adjustment,” in *Ultrasonics Symposium, 2007. IEEE*, Oct. 2007, pp. 1444–1447.

[131] J. Capilla, J. Olivares, M. Clement, J. Sangrador, E. Iborra, V. Felmetsger, and A Devos, “Ta_2O_5/SiO_2 insulating acoustic mirrors for AlN-based X-band BAW resonators,” in *Ultrasonics Symposium (IUS), 2011 IEEE International*, Oct. 2011, pp. 1704–1707.

[132] M. Benetti, D. Cannata, A. D’Amico, F. Di Pietrantonio, V. Foglietti, and E. Verona, “Thin film bulk acoustic wave resonator (TFBAR) gas sensor,” in *IEEE Ultrasonics Symposium, 2004*, Institute of Electrical and Electronics Engineers, 2004, pp. 1581–1584.

[133] M. DeMiguel-Ramos, B. Diaz-Duran, J. Munir, M. Clement, T. Mirea, J. Olivares, and E. Iborra, “Tungsten Oxide Layers of High Acoustic Impedance for Fully Insulating Acoustic Reflectors,” in *IEEE Transactions on Ultrasonics, Ferroelectrics, and Frequency Control*, vol. 63, Institute of Electrical and Electronics Engineers (IEEE), Jul. 2016, pp. 938–944.

[134] S. Rai, Y. Su, W. Pang, R. Ruby, and B. Otis, “A digitally compensated 1.5 GHz CMOS/FBAR frequency reference,” *Ultrasonics, Ferroelectrics and Frequency Control, IEEE Transactions on*, vol. 57, no. 3, pp. 552–561, 2010.

[135] S. Ohta, K. Nakamura, A. Doi, and Y. Ishida, “Temperature characteristics of solidly mounted piezoelectric thin film resonators,” *IEEE Symposium on Ultrasonics, 2003*, 2003.

[136] J. Munir, T. Mirea, M. DeMiguel-Ramos, M. Saeed, A. Bin Shaari, and E. Iborra, “Effects of compensating the temperature coefficient of frequency with the acoustic reflector layers on the overall performance of solidly mounted resonators,” *Ultrasonics*, vol. 74, pp. 153–160, Oct. 2016.

[137] M. DeMiguel-Ramos, J. Olivares, T. Mirea, M. Clement, E. Iborra, G. Rughoobur, L. Garcia-Gancedo, A. J. Flewitt, and W. I. Milne, “The influence of acoustic reflectors on the temperature coefficient of frequency of solidly mounted resonators,” in *2014 IEEE International Ultrasonics Symposium*, Sep. 2014, pp. 1472–1475.

[138] K. K. Kanazawa and J. G. Gordon, “Frequency of a quartz microbalance in contact with liquid,” *Analytical Chemistry*, vol. 57, no. 8, pp. 1770–1771, Jul. 1985.

[139] L. Qin, Q. Chen, H. Cheng, Q. Chen, J.-F. Li, and Q.-M. Wang, “Viscosity sensor using ZnO and AlN thin film bulk acoustic resonators with tilted polar c-axis orientations,” *Journal of Applied Physics*, vol. 110, no. 9, p. 094 511, 2011.

[140] G. Wingqvist, J. Bjurström, L. Liljeholm, I. Katardjiev, and A. L. Spetz, "Shear Mode AlN Thin Film Electroacoustic Resonator for Biosensor Applications," in *IEEE Sensors, 2005.*, Institute of Electrical and Electronics Engineers, 2005, pp. 492–495.

[141] J. Weber, W. M. Albers, J. Tuppurainen, M. Link, R. Gabl, W. Wersing, and M. Schreiter, "Shear mode FBARs as highly sensitive liquid biosensors," *Sensors and Actuators A: Physical*, vol. 128, no. 1, pp. 84–88, Mar. 2006.

[142] J. Bjurström, D. Rosen, I. Katardjiev, V. Yanchev, and I. Petrov, "Dependence of the electromechanical coupling on the degree of orientation of c-textured thin AlN films," *IEEE Trans. Ultrason., Ferroelect., Freq. Contr.*, vol. 51, no. 10, pp. 1347–1353, Oct. 2004.

[143] M. Moreria, J. Bjurstrom, T. Kubart, B. Kuzavas, and I. Katardjiev, "Synthesis of c-tilted AlN films with a good tilt and thickness uniformity," in *Ultrasonics Symposium (IUS), 2011 IEEE International*, IEEE, Oct. 2011.

[144] S. S. Pottigari and J. W. Kwon, "Vacuum-gapped film bulk acoustic resonator for low-loss mass sensing in liquid," in *TRANSDUCERS 2009 - 2009 International Solid-State Sensors, Actuators and Microsystems Conference*, Institute of Electrical and Electronics Engineers, Jun. 2009, pp. 156–159.

[145] C. P. Tan and H. G. Craighead, "Surface Engineering and Patterning Using Parylene for Biological Applications," *Materials*, vol. 3, no. 3, pp. 1803–1832, Mar. 2010.

[146] B. Joddar, E. Garcia, A. Casas, and C. M. Stewart, "Development of functionalized multi-walled carbon-nanotube-based alginate hydrogels for enabling biomimetic technologies," *Scientific Reports*, vol. 6, p. 32 456, 2016.

[147] M. Dragoman, A. Muller, D. Neculoiu, D. Vasilache, G. Konstantinidis, K. Grenier, D. Dubuc, L. Bary, R. Plana, and E. Flahaut, "High performance thin film bulk acoustic resonator covered with carbon nanotubes," *Applied Physics Letters*, vol. 89, no. 14, p. 143 122, 2006.

[148] M. Penza, P. Aversa, G. Cassano, D. Suriano, W. Wlodarski, M. Benetti, D. Cannata, F. Di Pietrantonio, and E. Verona, “Thin-Film Bulk-Acoustic-Resonator Gas Sensor Functionalized With a Nanocomposite Langmuir-Blodgett Layer of Carbon Nanotubes,” *IEEE Transactions on Electron Devices*, vol. 55, no. 5, pp. 1237–1243, May 2008.

[149] S. Esconjauregui, T. Makaryan, T. Mirea, M. DeMiguel-Ramos, J. Olivares, Y. Guo, H. Sugime, L. D’Arsié, J. Yang, S. Bhardwaj, C. Cepek, J. Robertson, and E. Iborra, “Carbon nanotube forests as top electrode in electroacoustic resonators,” *Applied Physics Letters*, vol. 107, no. 13, p. 133 106, Sep. 2015.

[150] E. Iborra, J. Sangrador, M. Clement, T. Mirea, M. DeMiguel-Ramos, J. Olivares, J. Capilla, L. García-Gancedo, S. Esconjauregui, A. J. Flewitt, and W. I. Milne, “Acoustic properties of carbon nanotube electrodes in BAW resonators,” in *European Frequency and Time Forum International Frequency Control Symposium (EFTF/IFC), 2013 Joint*, Jul. 2013, pp. 984–987.

[151] J. Ruffner, P. Clem, B. Tuttle, D Dimos, and D. Gonzales, “Effect of substrate composition on the piezoelectric response of reactively sputtered AlN thin films,” *Thin Solid Films*, vol. 354, no. 1-2, pp. 256–261, Oct. 1999.

[152] C.-H. Chao, P.-W. Chi, and D.-H. Wei, “Investigations on the Crystallographic Orientation Induced Surface Morphology Evolution of ZnO Thin Films and Their Wettability and Conductivity,” *The Journal of Physical Chemistry C*, vol. 120, no. 15, pp. 8210–8219, Apr. 2016.

[153] J. H. Lin and Y. H. Kao, “Wireless temperature sensing using a passive RFID tag with film bulk acoustic resonator,” in *Ultrasonics Symposium, 2008. IUS 2008. IEEE*, 2008, pp. 2209–2212.

[154] J. Olivares, E. Wegmann, J. Capilla, E. Iborra, M. Clement, L. Vergara, and R. Aigner, “Sputtered SiO_2 as low acoustic impedance material for Bragg mirror fabrication in BAW resonators,” *IEEE Transactions on Ultrasonics, Ferroelectrics and Frequency Control*, vol. 57, no. 1, pp. 23–29, Jan. 2010.

[155] M. Clement, E. Iborra, J. Sangrador, A. Sanz-Hervaís, L. Vergara, and M. Aguilar, “Influence of sputtering mechanisms on the preferred orientation of aluminum nitride thin films,” *Journal of Applied Physics*, vol. 94, no. 3, p. 1495, 2003.

[156] M. DeMiguel-Ramos, M. Clement, J. Olivares, J. Capilla, J. Sangrador, and E. Iborra, “Induced surface roughness to promote the growth of tilted-AlN films for shear mode resonators,” in *European Frequency and Time Forum International Frequency Control Symposium (EFTF/IFC), 2013 Joint*, IEEE, Jul. 2013.

[157] A. J. Flewitt, J. D. Dutson, P Beecher, D Paul, S. J. Wakeham, M. E. Vickers, C Ducati, S. P. Speakman, W. I. Milne, and M. J. Thwaites, “Stability of thin film transistors incorporating a zinc oxide or indium zinc oxide channel deposited by a high rate sputtering process,” *Semicond. Sci. Technol.*, vol. 24, no. 8, p. 085 002, Jun. 2009.

[158] Microchemicals, *Technical data sheet*, http://www.microchemicals.com/micro/az_5214e.pdf, Online, Nov. 2016.

[159] Viscopedia, *Whole Blood*, http://www.viscopedia.com/viscosity-tables/substances/whole-blood/#c1740, Online, Jan. 2017.

[160] H. Hinghofer-Szalkay and J. E. Greenleaf, “Continuous monitoring of blood volume changes in humans,” *Journal of Applied Physiology*, vol. 63, no. 3, pp. 1003–1007, Sep. 1987.

[161] M. Inoue, “The properties of aluminum thin films sputter deposited at elevated temperatures,” *J. Vac. Sci. Technol. A*, vol. 6, no. 3, p. 1636, May 1988.

[162] S. C. Her and Y. H. Wang, “Temperature Effect on Mechanical Properties of Aluminum Film,” *Applied Mechanics and Materials*, vol. 479-480, pp. 96–99, Dec. 2013.

[163] J. A. Thornton, “The microstructure of sputter-deposited coatings,” *Journal of Vacuum Science & Technology A: Vacuum, Surfaces, and Films*, vol. 4, no. 6, p. 3059, Nov. 1986.

[164] A. Anders, “A structure zone diagram including plasma-based deposition and ion etching,” *Thin Solid Films*, vol. 518, no. 15, pp. 4087–4090, May 2010.

[165] A. James and M. Lord, *Chemical and Physical Data Handbook*, 97th ed. Nature Publishing Group, 1992.

[166] S. Iijima, “Helical microtubules of graphitic carbon,” *Nature*, vol. 354, no. 6348, pp. 56–58, Nov. 1991.

[167] A. Thess, R. Lee, P. Nikolaev, H. Dai, P. Petit, J. Robert, C. Xu, Y. H. Lee, S. G. Kim, A. G. Rinzler, and et al., “Crystalline Ropes of Metallic Carbon Nanotubes,” *Science*, vol. 273, no. 5274, pp. 483–487, Jul. 1996.

[168] J. Robertson, S. Hofmann, M. Cantoro, A. Parvez, C. Ducati, G. Zhong, R. Sharma, and C. Mattevi, “Controlling the Catalyst During Carbon Nanotube Growth,” *Journal of Nanoscience and Nanotechnology*, vol. 8, no. 11, pp. 6105–6111, Nov. 2008.

[169] V. Jourdain and C. Bichara, “Current understanding of the growth of carbon nanotubes in catalytic chemical vapour deposition,” *Carbon*, vol. 58, pp. 2–39, Jul. 2013.

[170] J. W. Ding, X. H. Yan, J. X. Cao, D. L. Wang, Y Tang, and Q. B. Yang, “Curvature and strain effects on electronic properties of single-wall carbon nanotubes,” *Journal of Physics: Condensed Matter*, vol. 15, no. 27, pp. L439–L445, Jun. 2003.

[171] G. Zhong, J. H. Warner, M. Fouquet, A. W. Robertson, B. Chen, and J. Robertson, “Growth of Ultrahigh Density Single-Walled Carbon Nanotube

Forests by Improved Catalyst Design," *ACS Nano*, vol. 6, no. 4, pp. 2893–2903, Apr. 2012.

[172] L. M. Hoyos-Palacio, A. G. García, J. F. Pérez-Robles, J González, and H. V. Martínez-Tejada, "Catalytic effect of Fe, Ni, Co and Mo on the CNTs production," *IOP Conference Series: Materials Science and Engineering*, vol. 59, p. 012 005, Jun. 2014.

[173] F. Ding, P. Larsson, J. A. Larsson, R. Ahuja, H. Duan, A. Rosén, and K. Bolton, "The Importance of Strong Carbon-Metal Adhesion for Catalytic Nucleation of Single-Walled Carbon Nanotubes," *Nano Letters*, vol. 8, no. 2, pp. 463–468, Feb. 2008.

[174] H. Sugime, S. Esconjauregui, J. Yang, L. D'Arsié, R. A. Oliver, S. Bhardwaj, C. Cepek, and J. Robertson, "Low temperature growth of ultra-high mass density carbon nanotube forests on conductive supports," *Applied Physics Letters*, vol. 103, no. 7, p. 073 116, 2013.

[175] H. Sugime, S. Esconjauregui, L. D'Arsié, J. Yang, A. W. Robertson, R. A. Oliver, S. Bhardwaj, C. Cepek, and J. Robertson, "Low-Temperature Growth of Carbon Nanotube Forests Consisting of Tubes with Narrow Inner Spacing Using Co/Al/Mo Catalyst on Conductive Supports," *ACS Applied Materials & Interfaces*, vol. 7, no. 30, pp. 16 819–16 827, Aug. 2015.

[176] Y. Murakami, S. Chiashi, Y. Miyauchi, M. Hu, M. Ogura, T. Okubo, and S. Maruyama, "Growth of vertically aligned single-walled carbon nanotube films on quartz substrates and their optical anisotropy," *Chemical Physics Letters*, vol. 385, no. 3-4, pp. 298–303, Feb. 2004.

[177] L. Zhang, Y. Tan, and D. E. Resasco, "Controlling the growth of vertically oriented single-walled carbon nanotubes by varying the density of CoMo catalyst particles," *Chemical Physics Letters*, vol. 422, no. 1-3, pp. 198–203, Apr. 2006.

[178] H. M. Christen, A. A. Puretzky, H. Cui, K. Belay, P. H. Fleming, D. B. Geohegan, and D. H. Lowndes, "Rapid Growth of Long, Vertically Aligned Carbon Nanotubes through Efficient Catalyst Optimization Using Metal Film Gradients," *Nano Letters*, vol. 4, no. 10, pp. 1939–1942, Oct. 2004.

[179] J. E. Herrera, L. Balzano, A. Borgna, W. E. Alvarez, and D. E. Resasco, "Relationship between the Structure/Composition of Co-Mo Catalysts and Their Ability to Produce Single-Walled Carbon Nanotubes by CO Disproportionation," *Journal of Catalysis*, vol. 204, no. 1, pp. 129–145, Nov. 2001.

[180] M. Hu, "Morphology and chemical state of Co-Mo catalysts for growth of single-walled carbon nanotubes vertically aligned on quartz substrates," *Journal of Catalysis*, vol. 225, no. 1, pp. 230–239, Jul. 2004.

[181] H. Sugime, S. Noda, S. Maruyama, and Y. Yamaguchi, "Multiple optimum conditions for Co-Mo catalyzed growth of vertically aligned single-walled carbon nanotube forests," *Carbon*, vol. 47, no. 1, pp. 234–241, Jan. 2009.

[182] J. Olivares, T. Mirea, B. Díaz-Durán, M. Clement, M. DeMiguel-Ramos, J. Sangrador, J. de Frutos, and E. Iborra, "Growth of carbon nanotube forests on metallic thin films," *Carbon*, vol. 90, pp. 9–15, 2015.

[183] P Mitra and A. K. Mukhopadhyay, "ZnO thin film as methane sensor," *Bulletin of the Polish Academy of Sciences-Technical Sciences*, vol. 55, no. 3, pp. 281–285, 2007.

[184] H. Shokry Hassan, A. Kashyout, I. Morsi, A. Nasser, and I. Ali, "Synthesis, characterization and fabrication of gas sensor devices using ZnO and ZnO:In nanomaterials," *Beni-Suef University Journal of Basic and Applied Sciences*, vol. 3, no. 3, pp. 216–221, Sep. 2014.

[185] C. Mateo-Mateo, C. Vázquez-Vázquez, M. Pérez-Lorenzo, V. Salgueiriño, and M. A. Correa-Duarte, "Ostwald Ripening of Platinum Nanoparticles Confined in a Carbon Nanotube/Silica-Templated Cylindrical Space," *Journal of Nanomaterials*, vol. 2012, pp. 1–6, 2012.

[186] S. Manivannan, J. H. Ryu, H. E. Lim, M. Nakamoto, J. Jang, and K. C. Park, “Properties of surface treated transparent conducting single walled carbon nanotube films,” *Journal of Materials Science: Materials in Electronics*, vol. 21, no. 1, pp. 72–77, Mar. 2009.

[187] M. DeMiguel-Ramos, B. Díaz-Durán, J.-M. Escolano, M. Barba, T. Mirea, J. Olivares, M. Clement, and E. Iborra, “Gravimetric biosensor based on a 1.3GHz AlN shear-mode solidly mounted resonator,” *Sensors and Actuators B: Chemical*, vol. 239, no. 2017, pp. 1282–1288, Feb. 2017.

[188] Y. Song and J. Choi, “Carbon nanotube volatile organic liquid sensor,” *Applied Physics Letters*, vol. 95, no. 12, p. 123 122, 2009.

[189] H. Liu, J. Zhai, and L. Jiang, “Wetting and anti-wetting on aligned carbon nanotube films,” *Soft Matter*, vol. 2, no. 10, p. 811, 2006.

[190] J. Evertsson, F. Bertram, F. Zhang, L. Rullik, and et al., “The thickness of native oxides on aluminum alloys and single crystals,” *Applied Surface Science*, vol. 349, pp. 826–832, 2015.

[191] M. DeMiguel-Ramos, M. Clement, J. Goicuria, J. Olivares, T. Mirea, E. Iborra, G. Rughoobur, A. Flewitt, and W. Milne, “ZnO/AlN stacked BAW resonators with double resonance,” in *Ultrasonics Symposium (IUS), 2014 IEEE International*, Sep. 2014, pp. 1484–1487.

[192] I. S. Khattab, F. Bandarkar, M. A. A. Fakhree, and A. Jouyban, “Density, viscosity, and surface tension of water+ethanol mixtures from 293 to 323K,” *Korean Journal of Chemical Engineering*, vol. 29, no. 6, pp. 812–817, Jan. 2012.

[193] N. S. K. Gunda, M. Singh, L. Norman, K. Kaur, and S. K. Mitra, “Optimization and characterization of biomolecule immobilization on silicon substrates using (3-aminopropyl)triethoxysilane (APTES) and glutaraldehyde linker,” *Applied Surface Science*, vol. 305, pp. 522–530, Jun. 2014.

[194] K. Awasthi, D. Singh, S. K. Singh, D. Dash, and O. Srivastava, “Attachment of biomolecules (protein and DNA) to amino-functionalized carbon nanotubes,” *New Carbon Materials*, vol. 24, no. 4, pp. 301–306, Dec. 2009.

[195] S. Vardharajula, P. Tiwari, E. Eroğlu, K. Vig, V. Dennis, Ali, and S. Singh, “Functionalized carbon nanotubes: Biomedical applications,” *International Journal of Nanomedicine*, p. 5361, Oct. 2012.

[196] Y. Gao, T. Kodama, Y. Won, S. Dogbe, L. Pan, and K. E. Goodson, “Impact of nanotube density and alignment on the elastic modulus near the top and base surfaces of aligned multi-walled carbon nanotube films,” *Carbon*, vol. 50, no. 10, pp. 3789–3798, Aug. 2012.

[197] J. Yoon, C. Q. Ru, and A. Mioduchowski, “Noncoaxial resonance of an isolated multiwall carbon nanotube,” *Physical Review B*, vol. 66, no. 23, Dec. 2002.

[198] A. Fragoso and C. O’Sullivan, “Electrochemical Immunosensor for Detection of Proteic Cancer Markers,” *Biosensors and Molecular Technologies for Cancer Diagnostics*, pp. 573–590, May 2012.

[199] M. N. Hochmeister, B. Budowle, O. Rudin, C Gehrig, U. Borer, M Thali, and D. R., “Evaluation of prostate-specific antigen (PSA) membrane test assays for the forensic identification of seminal fluid.,” *Journal of Forensic Science*, vol. 44, no. 5, pp. 1057–1060, 1999.

[200] X. Zhao, F. Pan, G. M. Ashley, L. García-Gancedo, J. Luo, A. J. Flewitt, W. I. Milne, and J. R. Lu, “Label-free detection of human prostate-specific antigen (hPSA) using film bulk acoustic resonators (FBARs),” *Sensors and Actuators B: Chemical*, vol. 190, pp. 946–953, Jan. 2014.